Appendix D

Image Analysis

December 2019

TABLE OF CONTENTS

LIST OF FIGURES

1. INTRODUCTION

This Appendix presents the integrated analysis of the available imaging (interferometric synthetic aperture radar ("InSAR"), radar, and video and drone footage), topographic, survey, and rainfall data of the Vale S.A. ("Vale") Córrego do Feijão Mine Dam I ("Dam I") in Brumadinho, Brazil for the one-year period prior to the failure of Dam I. This analysis includes locating zones of deformation and wet spots (via Sentinel or other appropriate satellite images), as well as evaluating the volume of tailings in the dam. It also provides a breakdown/time-lapse analysis of video footage of Dam I on the failure date, which was used to support the analysis of the failure mechanism. After an initial brief description of the data sources, the Appendix describes the main outcomes of the analyses for the different investigated datasets.

2. DATA SOURCES

The principal datasets analyzed included:

- Topographic data: pre-dam contours of the Dam I area, pre-failure light detection and ranging ("LiDAR") data of Dam I dated September 2018, and post-failure LiDAR data of Dam I dated February 2019.
- Survey data: 14 prisms located on the crest of Dam I, surveyed on a monthly basis by Vale with a total station (i.e., an electronic/optical instrument used for surveying composed by a theodolite integrated with electronic distance measurement ("EDM") to measure both vertical and horizontal angles and the slope distance from the instrument to a particular point), operated manually, covering the period from August 31, 2011, to December 12, 2018.
- Slope stability radar data: ground-based radar data collected by the IBIS-FM system covering the period from March 1, 2018, to January 25, 2019, with 480 images/day, including real-time and "slow movement" processing.
- Satellite InSAR datasets: measurements obtained from the interferometric multi-image processing of satellite synthetic aperture radar ("SAR") images for the following datasets:
    - Sentinel-1 descending orbits: 30 images covering the period from January 3, 2018, to January 22, 2019;
    - TerraSAR-X ascending orbits: 28 images covering the period from February 8, 2018, to January 15, 2019;
    - Sentinel-1 and TerraSAR-X decomposed vertical and east to west ("E-W") components of the deformation vectors covering the period from February 8, 2018, to January 15, 2019;
    - CosmoSkyMed ascending orbits: 24 images covering the period from September 23, 2017, to November 13, 2018;
    - CosmoSkyMed descending orbits: 76 images covering the period from September 7, 2017, to January 24, 2019; and
    - CosmoSkyMed decomposed vertical and E-W components of the deformation vectors covering the period from September 23, 2017, to November 13, 2018.

- Satellite multispectral images at high resolution: 19 multispectral images collected by the Sentinel-2 satellite at high resolution (10 meters (m) to 60 m), covering the period from January 22, 2018, to January 22, 2019, analyzed for the identification of wet spots, the presence of water surfaces, vegetation coverage, and human activity on Dam I and within the tailings.
- Satellite multi-spectral images at very high resolution: eight multispectral images collected by WorldView-3, GeoEye-1, and Pleiades satellites at very high resolution (0.31 m to 30 m), covering the period from June 2, 2018, to January 18, 2019, analyzed for the identification of wet spots, the presence of water surfaces, vegetation coverage, and human activity on Dam I and within the tailings.
- Rainfall data: data collected by the F18 rain gauge located approximately 1.4 kilometers (km) northwest (NW) of Dam I during the period from January 2018 to February 2019, analyzed to identify correlations with satellite InSAR data and the satellite optical image analysis.
- Videos: a frontal video and a video from the back of Dam I capturing the instant of the dam collapse and immediately following failure initiation (video specifications: RGB24, mp4, 24 bits per pixel, frame rate: 30 frames per second ("fps"), height: 1080 pixels, width: 1920 pixels).
- Drone footage: two videos from a drone taken on January 18, 2019—one week prior to the failure—were reviewed to identify any evidence of existing or past deformations.

3. TOPOGRAPHIC DATA ANALYSIS

The scope of the topographic data analysis can be summarized as follows:

- the evaluation of the thickness and volume of the tailings, based on the quantitative comparison between the pre-dam contour lines and the pre-failure LiDAR point cloud;
- the evaluation of the volume lost during the failure of Dam I, comparing the pre-failure (September 2018) and the post-failure (February 2019) LiDAR point clouds; and
- Topographic Wetness Index ("TWI") calculation using the pre-dam topography to identify hydrological flow paths in the pre-dam topography and their location with respect to the pre-failure topography.

The different topographic data have been imported and analyzed in a geographic information system ("GIS") environment to calculate the above listed parameters. Based on contour lines and point clouds, and using kriging algorithms, triangle surfaces were determined and have been transformed into grid files to calculate the difference in elevation on a pixel by pixel basis.

3.1 Volume and Thickness of Tailings

By comparing the pre-dam topography and pre-failure LiDAR point clouds, it was possible to estimate the volume and thickness of the tailings. The estimated volume of tailings stored in the dam at the time of failure is 8,413,000 cubic meters (m^3). This number does not include the embankment or tailings under the embankment. The thickness of the tailings is estimated to have reached a maximum depth of 76 m in the central storage portion of the dam and gradually reduces in thickness moving eastwards up the valley away from the dam crest. The tailings in the NW sector had a greater thickness when compared to the southeast (SE) sector (Figure 1).

The total volume and thickness of the tailings, including the embankment and the tailings under the embankment, is estimated to have been 12,726,000 m^3. The maximum difference in elevation between pre-dam and pre-failure topography is 76 m in relation to the central portion of the dam's crest (Figure 2).

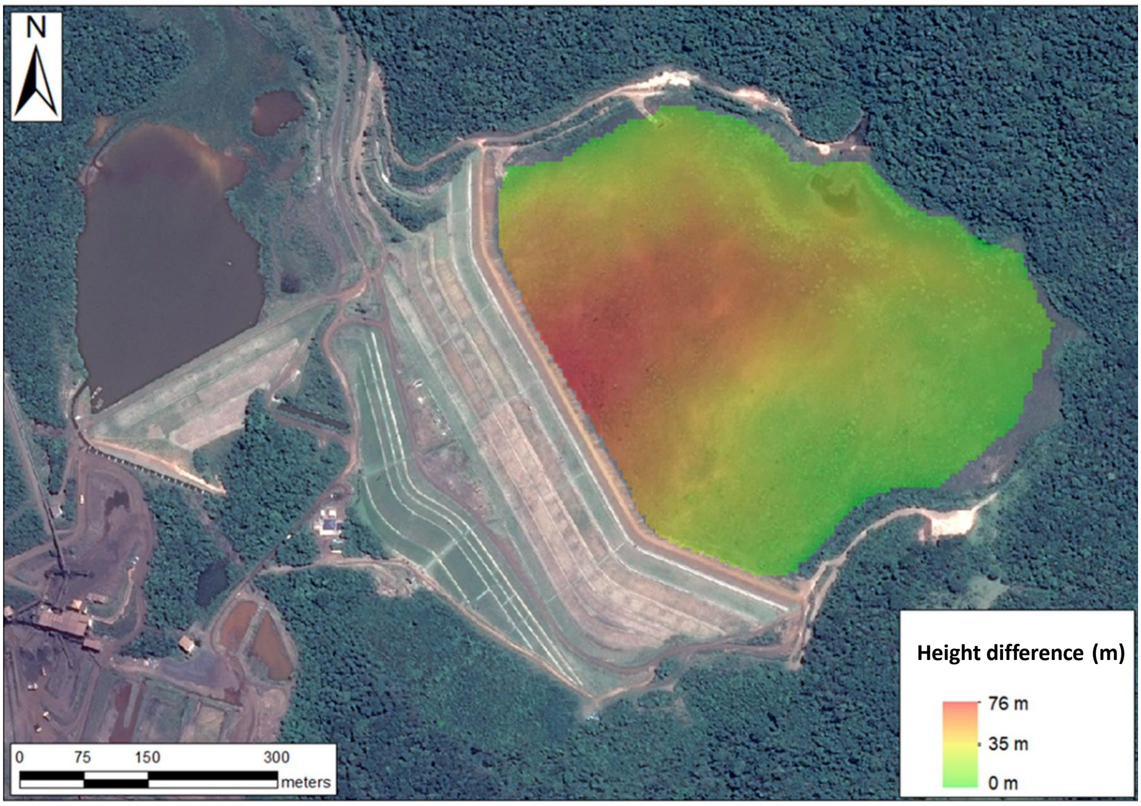

Figure 1: Height Difference Between the Original and Pre-failure Topographies, in Relation to the Tailings, Starting from the Crest of the Dam

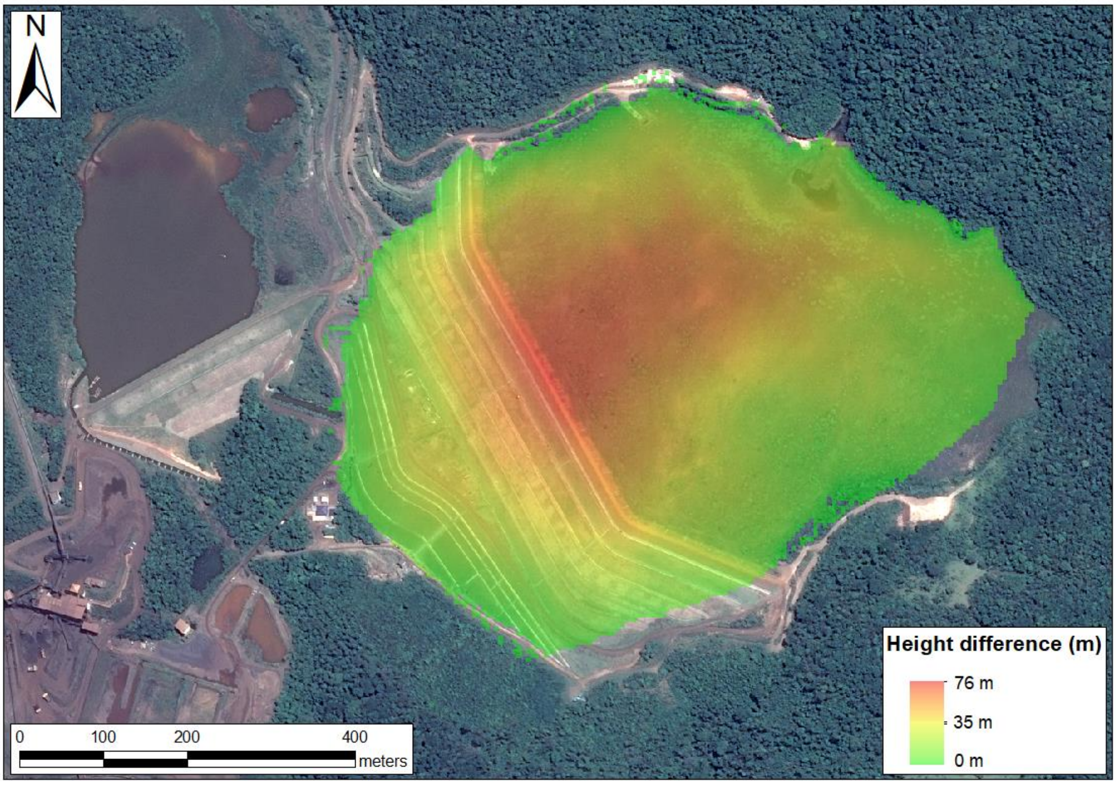

Figure 2: Height Difference Between the Original and Pre-failure Topographies, Including Embankment and Tailings Under Embankment

3.2 Volume of Failed Material

By comparing the pre- and post-failure topographies of Dam I, the volume of the failure is estimated to be 9,651,000 m^3, including the tailings, the dam, and some natural soils. The maximum difference in elevation between the pre- and post-failure surfaces is 79.2 m, located right behind the crest of the dam in the center (Figure 3).

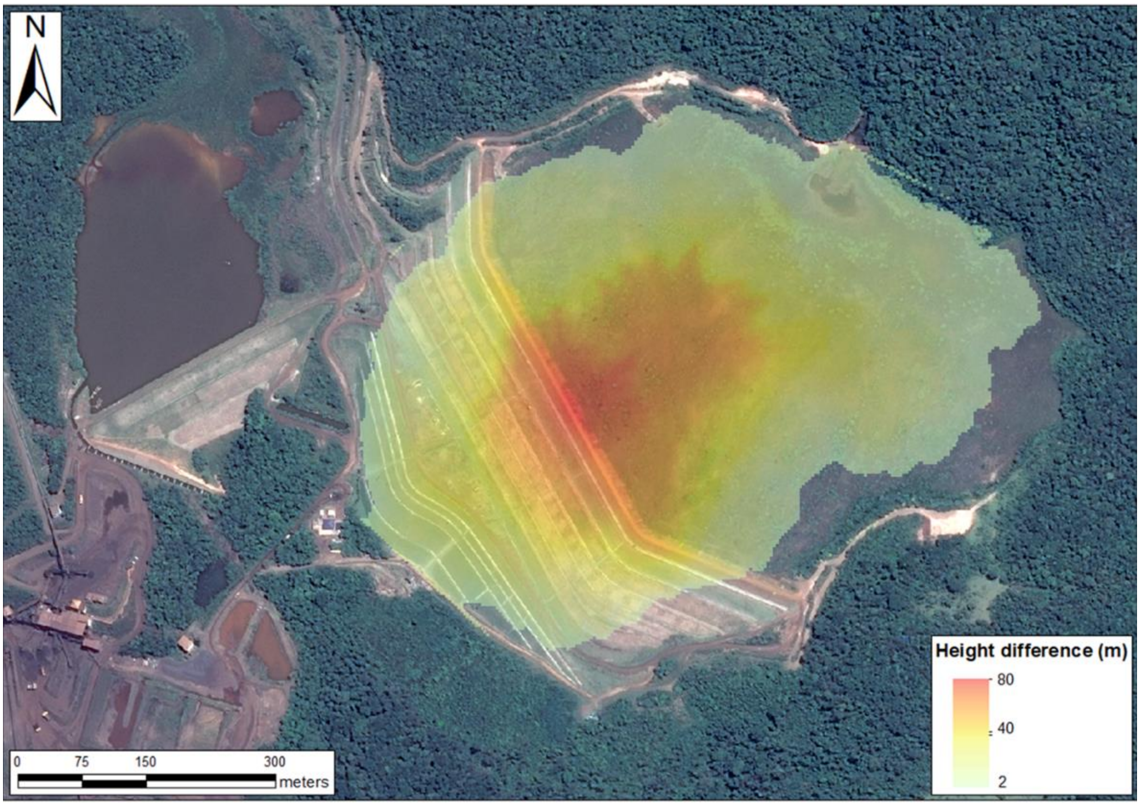

Figure 3: Height Difference Between Pre- and Post-failure Topographies

3.3 Topographic Wetness Index

TWI is commonly used to quantify topographic control on hydrological processes and to identify hydrological flow paths. It is a function of both the slope and the upstream contributing area per unit width orthogonal to the flow direction. It provides an estimate of the water flow before dam construction. High values of TWI indicate that water is accumulating. The spatial distribution of the TWI values in the analyzed area reveals that the flow accumulation obtained by calculating the TWI with the original topography is concentrated at the toe of Dam I, in its southern part, where the dam face is exposed to the southwest (SW) (Figure 4).

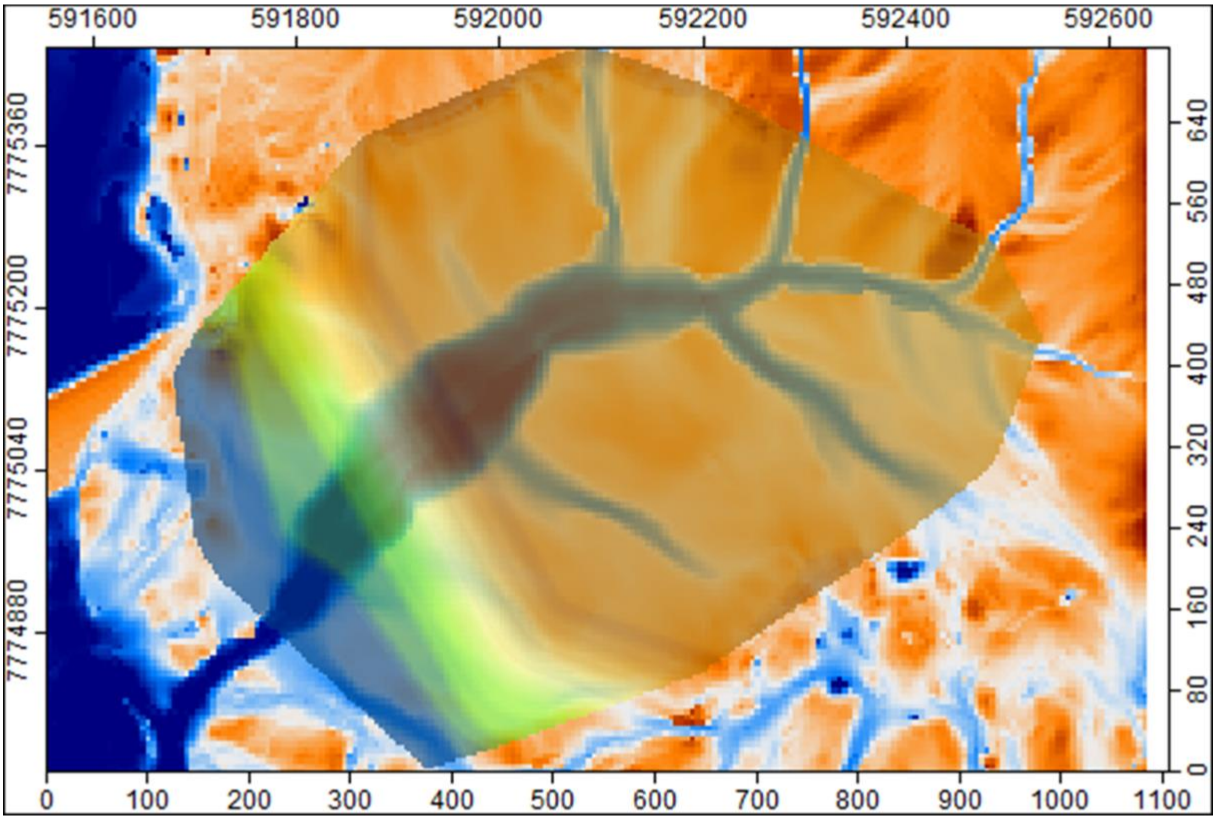

Figure 4: TWI of Dam I Footprint

4. PRISMS ANALYSIS

The main objective of the prisms analysis, which included data from 14 prisms located on the top of Dam I (Figure 5), was to determine whether surface deformations were detected by the prism monitoring and, if so, to analyze their spatial and temporal distributions.

14 prisms were located on the crest of the dam and surveyed manually with a total station. The 14 prisms corresponded to seven positions on the top of Dam I (points named MT-XX-BI are located in the same position of points named CFJB1MXXX, but are covering a different period of time).

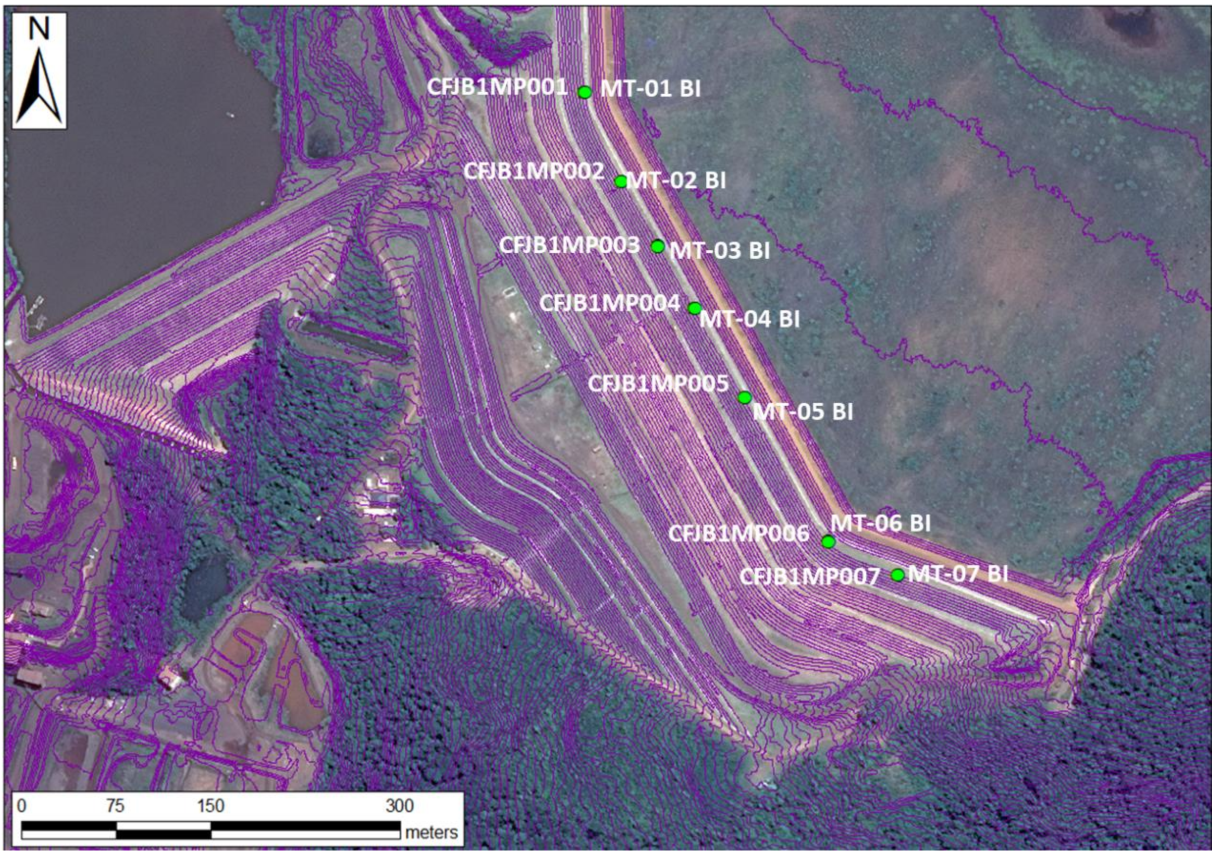

Figure 5: Location of Prism Installed on Dam I

Data acquired from prisms CFJB1MP001, CFJB1MP003, CFJB1MP004, CFJB1MP005, CFJB1MP006, and CFJB1MP007 were available from August 2011 to September 2016, with a monthly acquisition frequency (approximately). Data from prism CFJB1MP002 are available from August 2011 to June 2015. During this time interval, data were not acquired continuously; specifically, the following time intervals were not covered:

- December 2011;
- July, November, and December 2013;
- November 2014;
- January and March 2015; and
- From July 2015 to May 2016.

Data acquired by prisms MT-01 BI, MT-02 BI, MT-03 BI, MT-04 BI, MT-05 BI, MT-06 BI, and MT-07 BI cover a time interval between March 2017 and December 2018; data were collected monthly, except for the following periods:

- June 2018 when data were collected four times; and
- October 2018 when data were collected two times.

The last acquisition of prism data before the failure was December 12, 2018.

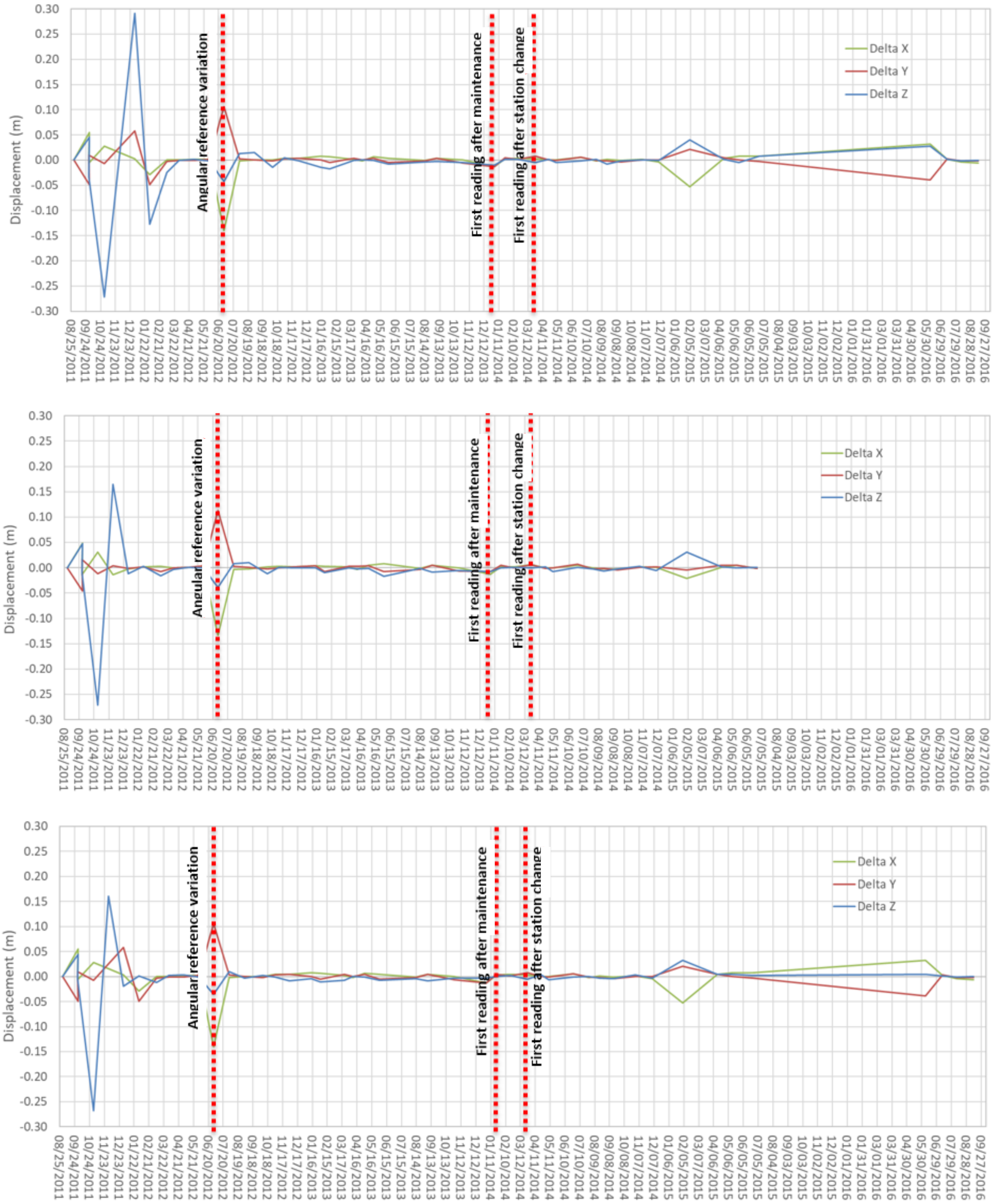

Figure 6: (Top to Bottom) Data (x, y, and z Components) for Prisms CFJB1MP001, CFJB1MP002 and CFJB1MP003

The data in Figures 6 through 9 showed spikes; sometimes these spikes were associated with changes in the total station set up, but in other cases the origin of the spikes is unclear. The noise level (estimated by considering the difference between the minimum and maximum deformation measured, not including the major spikes) is of centimetric order, which is compatible with the manual acquisition and the survey distance. No clear trends were detected above the noise level during the monitoring period, including the last months before the failure (Figure 10 and Figure 11).

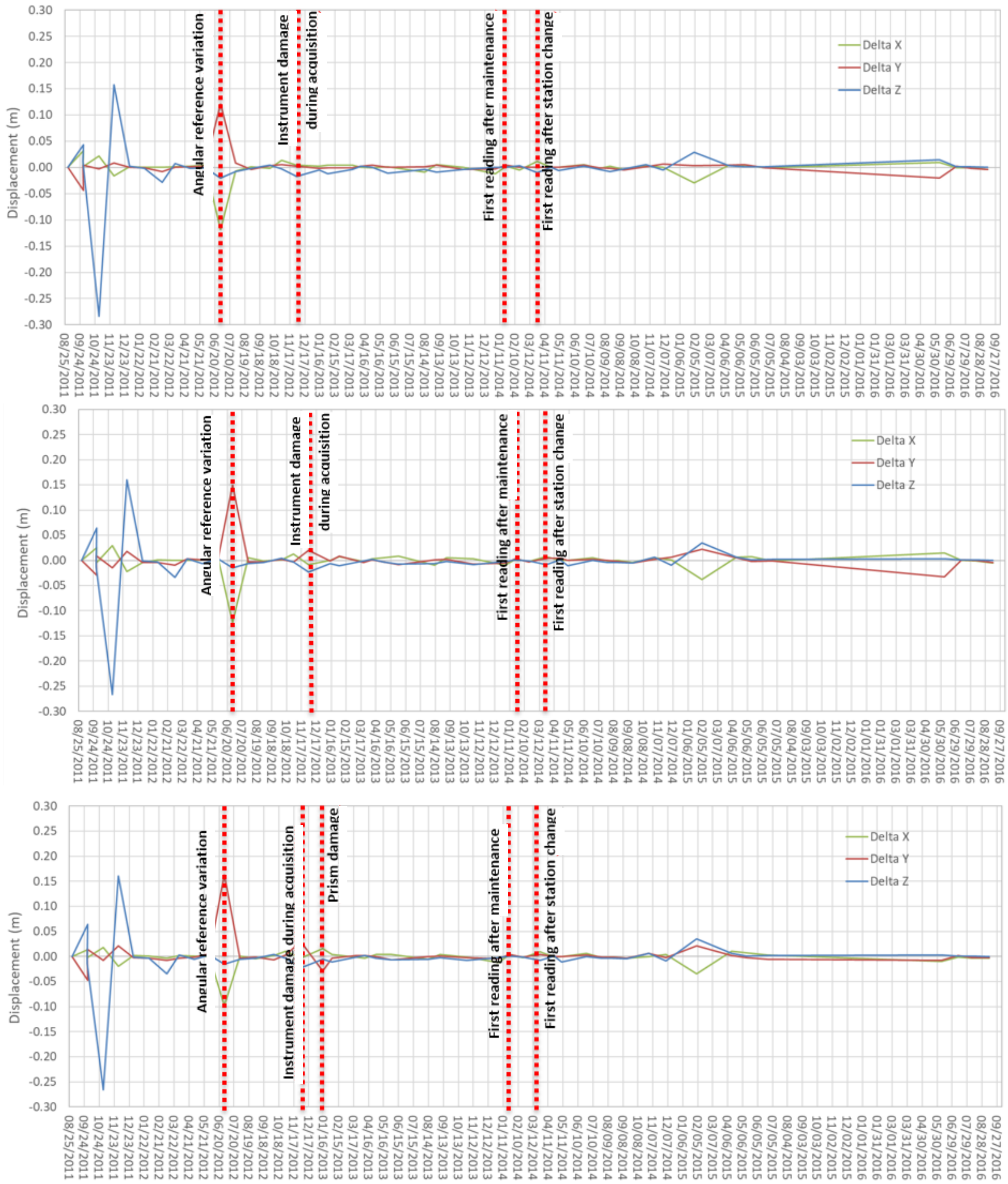
Displacement (m)
Angular reference variation
Instrument damage
during acquisition
First reading after maintenance
First reading after station change
Prism damage
Delta X
Delta Y
Delta Z

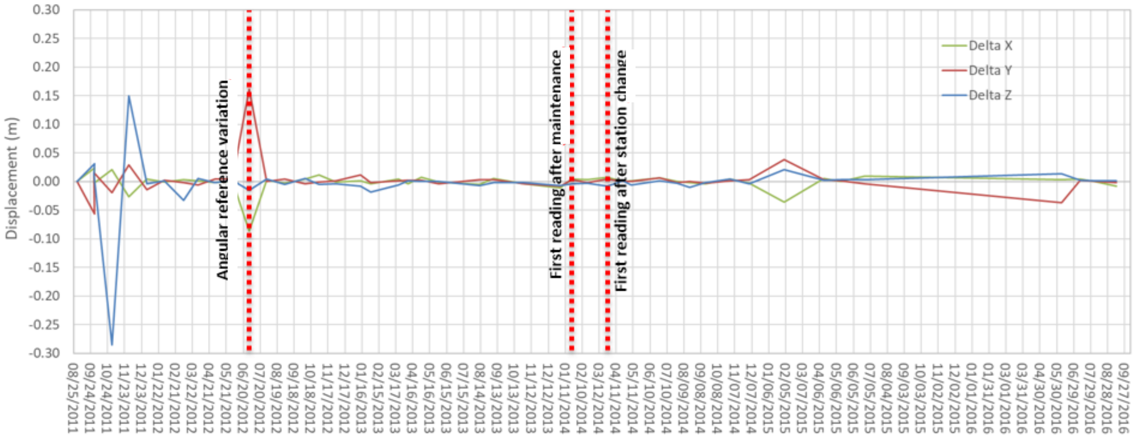

Figure 7: (Top to Bottom) Data for Prisms CFJB1MP004, CFJB1MP005, CFJB1MP006, and CFJB1MP007

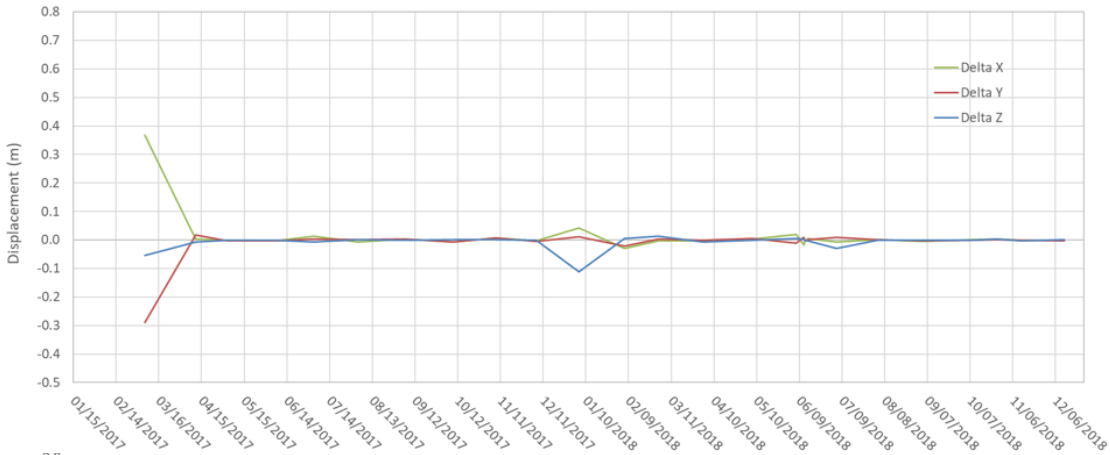

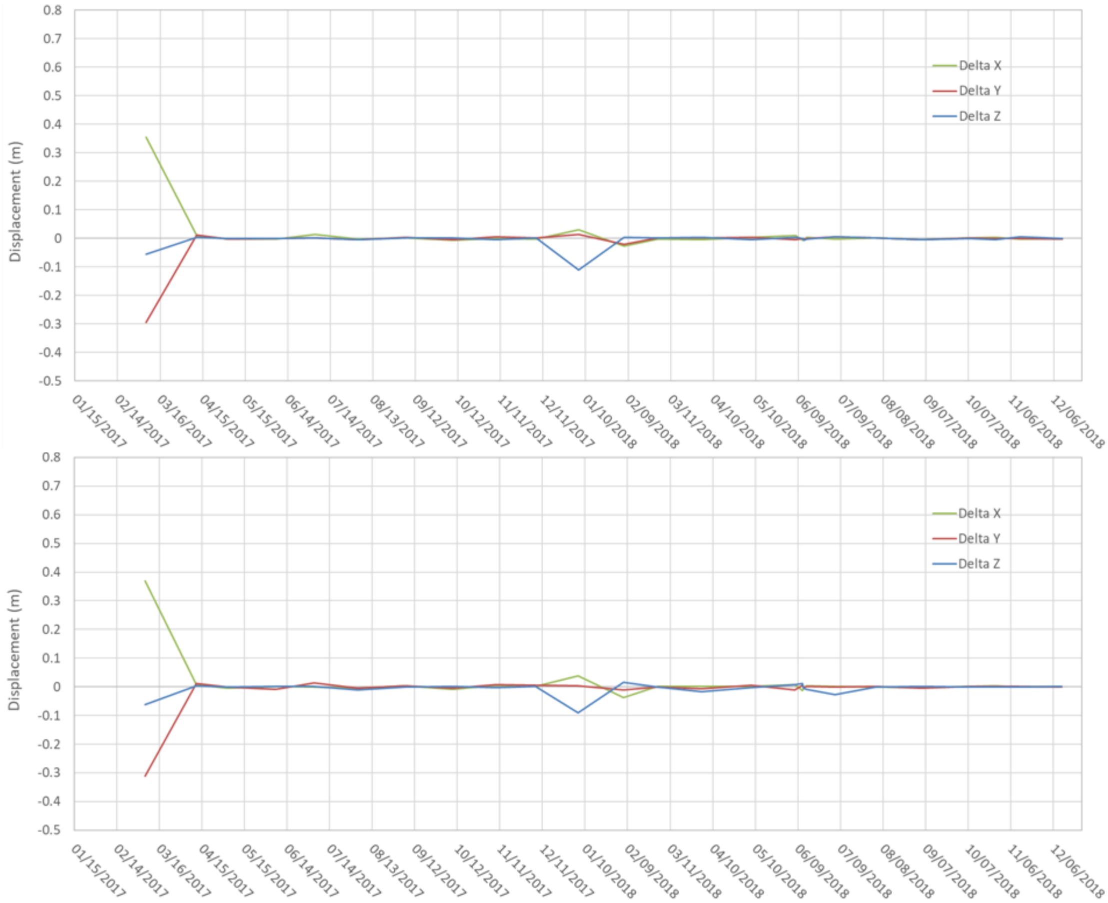

Figure 8: (Top to Bottom) Data for Prisms MT01-BI, MT02-BI, MT03-BI, MT04-BI

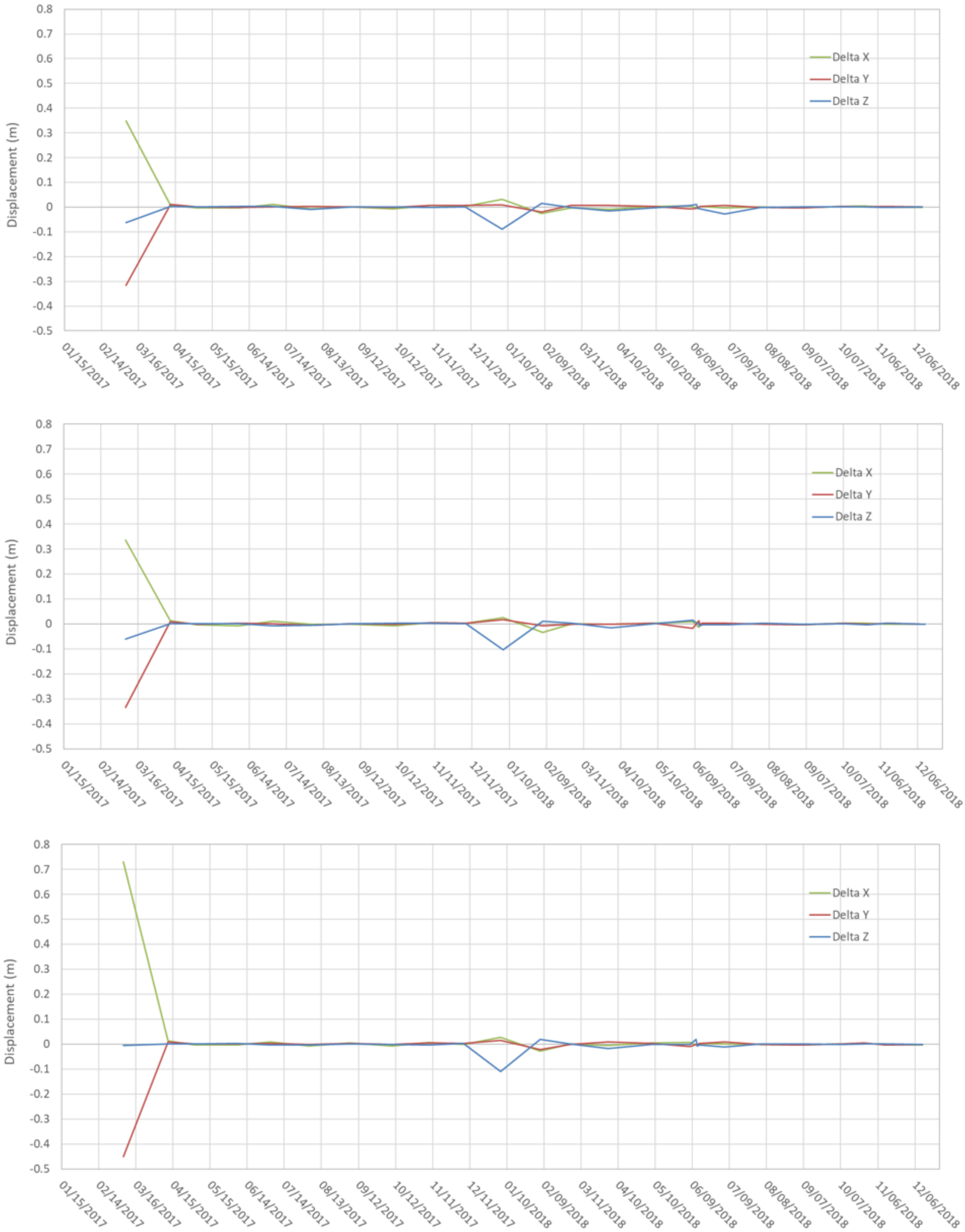

Figure 9: (Top to Bottom) Data for Prisms MT05-BI, MT06-BI and MT07-BI

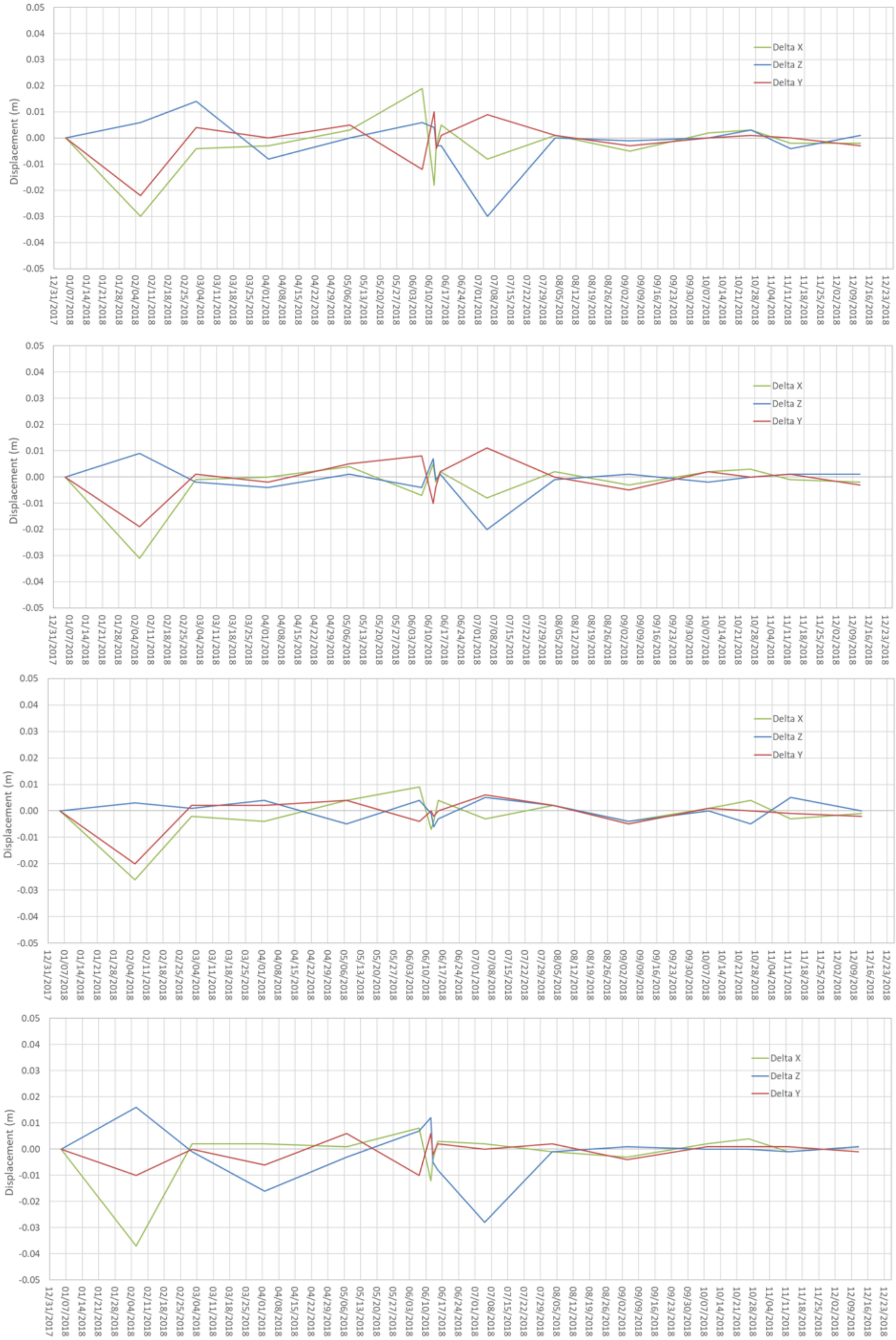

Figure 10: (Top to Bottom) 2018 Data for Prisms MT01-BI, MT02-BI, MT03-BI, MT04-BI

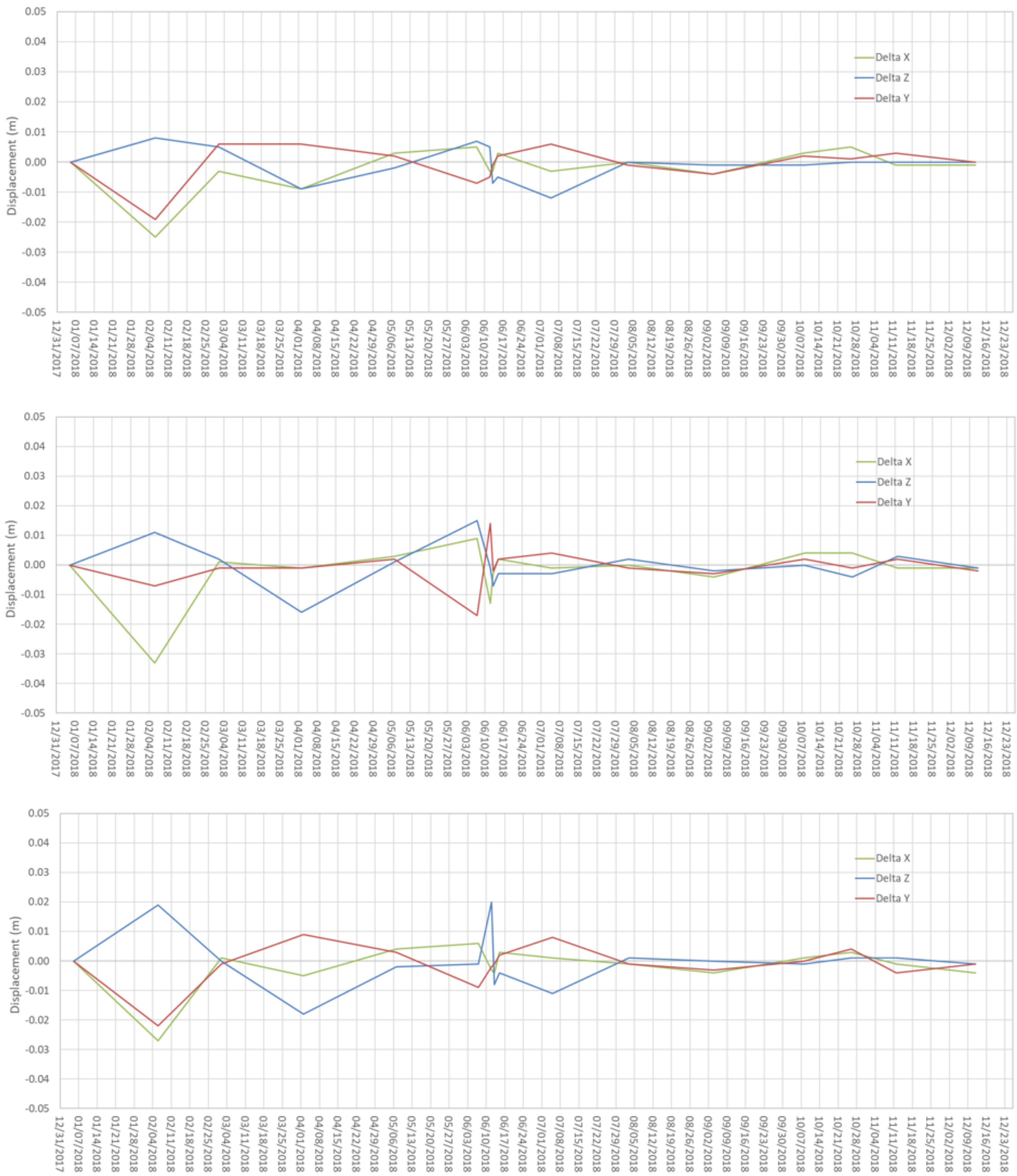

Figure 11: (Top to Bottom) 2018 Data for Prisms MT05-BI, MT06-BI, and MT07-BI

5. GROUND-BASED RADAR ANALYSIS

We reviewed the data acquired during the period from March 2018 to the failure date by the slope stability IBIS-FM radar, manufactured by IDS Georadar and installed at Dam I. The purpose in reviewing these data was to determine (i) whether surface deformations were detected by the ground-based radar; (ii) whether indications produced by the radar regarding those deformations were accurate and reliable; and (iii) the spatial and temporal distributions of any deformations observed.

The radar unit, installed in the stockpile area at a working distance from the dam ranging from 730 m to 1,160 m (i.e., the lower and upper part of the dam, respectively), collected data every 3 minutes ("min") (480 scans/day on average) (Figure 12). Because of the line-of-sight, the radar data have good sensitivity to horizontal deformations (both north (N) and east (E) components) but low sensitivity to vertical deformations, making the radar potentially capable of measuring dam deformations with horizontal components but less capable of measuring vertical deformations.

Figure 12: Position and Areal Coverage of IBIS-FM Radar

5.1 Real-time Data

We reviewed the data processed in real time prior to the failure, through IBIS Guardian software developed by IDS Georadar. Our review focused on the following questions:

- Did the radar detect any deformations in the 48 hours (h) prior to the failure?
- Did the radar data, while processed in real time, detect any deformations during the period from March 2018 to the last radar image prior to failure?
- Are the deformations reported in the monthly deformation maps produced by the radar software reliable, or do they correspond to noise?

The precision of the radar data processed in real time was estimated by IDS Georadar, through analysis of the distribution frequency of the deformation measurements collected over radar pixels characterized by high values of reflectivity prior to the collapse. The deformation measurements provided in that time interval are symmetrically distributed around zero, with a standard deviation of 0.6 millimeters (mm), thus indicating the precision of the measurement. Based on such analysis, according to IDS Georadar, the minimum detectable velocity of the radar in the specific set up of Dam I corresponds to 0.3 millimeters per hour (mm/h) along the radar line-of-sight.

Considering the above described precision, the review of the radar deformation maps for the last 48 h prior to the failure did not detect any deformations above the noise level of the radar (Figure 13). By increasing the temporal window of the cumulative deformation maps to include maps from 2 h, 4 h, 12 h, 24 h, and 48 h prior to failure, it is possible to observe a gradual increase in the deformation values with a scattered spatial distribution without any evident consistent pattern. We interpreted the measured deformation values as the effect of cumulative noise induced by the presence of vegetation on the dam face.

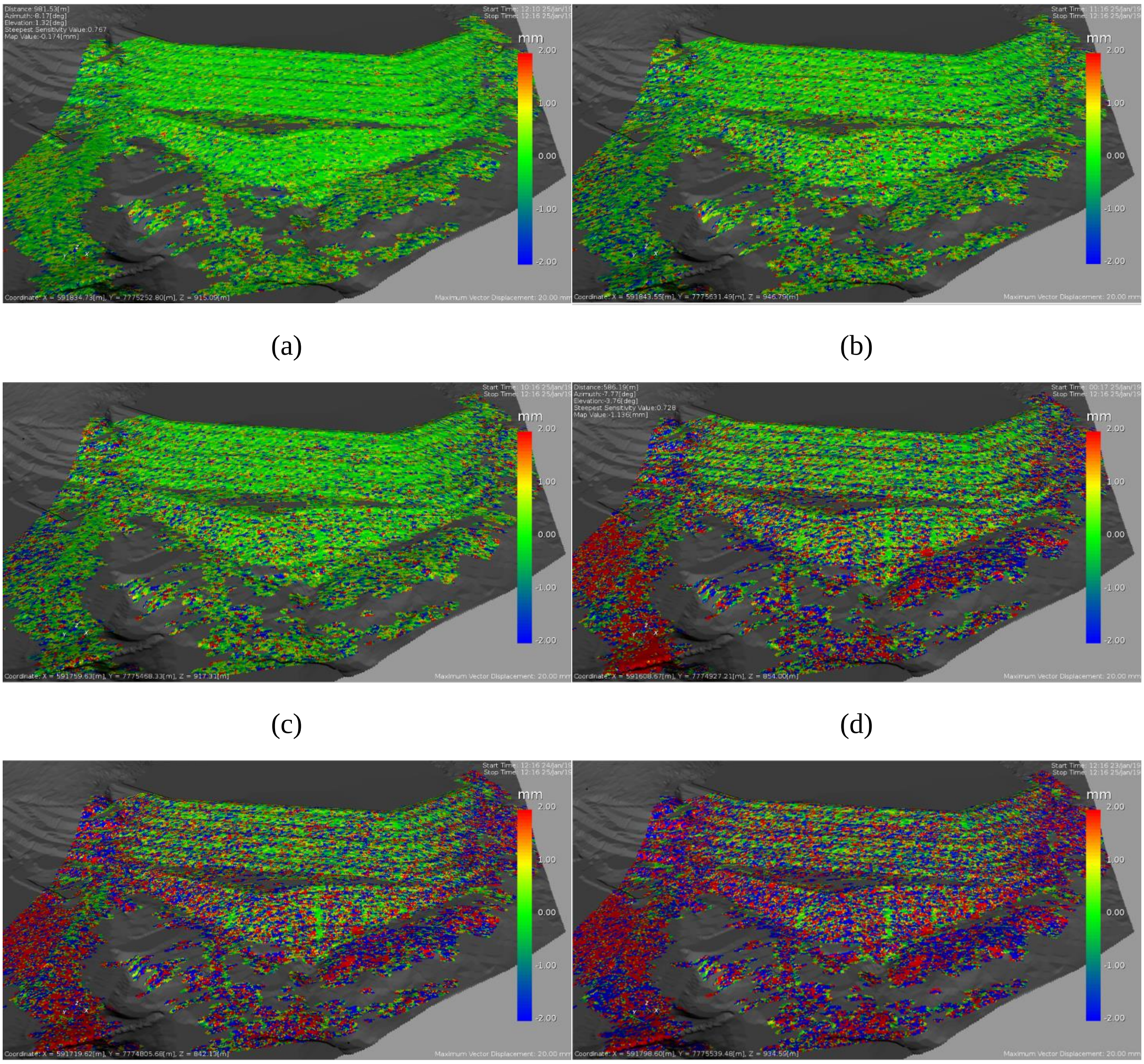

(a) (b)

(c) (d)

(e) (f)

Figure 13: Cumulative Deformation Map from IBIS-FM Radar Covering: (a) time of Failure, (b) 2 h Prior to Failure, (c) 4 h Prior to Failure , (d) 12 h Prior to Failure, (e) 24 h Prior to Failure, and (f) 48 h Prior to Failure

Radar uses microwaves (in this instance, the radar is working in the Ku band, corresponding to a wavelength of 1.8 centimeters), which are affected by the dielectric constant of the reflecting material.

Vegetation has a low reflectivity to the radar signal, and its growth and its movement are likely to be the main causes of the noise identified in the radar data. Such vegetation can induce the following effects in the radar data:

- decorrelation of the radar signal (coherence decrease) especially in the long term;
- false deformations induced by varying moisture content in the vegetation during the day; and
- vegetation on the sides of the dam can introduce noise in the radar data.

The monthly cumulative deformation maps produced by the radar between March 2018 and the date of the failure appear to identify significant surface deformations in different sectors of the dam, especially during March and April 2018. The amount of reported deformation from May to October 2018 is lower than that appearing in the maps for the period November 2018 to January 2019. The highest amount and the largest number of areas of the purported deformations appear in the March to April 2018 maps.

The reported deformations have both negative and positive signs, indicating deformations away from and toward the radar, respectively (Figure 14 and Figure 15). The amount of the purported deformation is significant (ranging from 200 to 700 mm in March 2018 and from 100 to 380 mm in April 2018) and above the noise level established by the radar manufacturer (i.e., 0.3 mm/h).

A re-evaluation of the ground-based radar data reveals that long-term deformations were not occurring as reported. For example, in April 2018, the ground-based radar purported to show large, new, and ongoing surface deformations of hundreds of millimeters in specific areas. However, the radar signal shown in the monthly deformation maps for March and April 2018 is not attributable to actual deformation, but is likely the result of cumulative noise induced by: (i) the presence of vegetation on the face of the dam, (ii) changes in moisture of the vegetation/soil, and (iii) cumulative residual atmospheric artifacts not properly compensated for between each consecutive radar scan (Figure 16 and Figure 17). This was confirmed by photographs taken at the time.

The two largest areas where deformations were reported by the ground-based radar (Areas 3 and 5 of Figure 16) show them directed away from the radar. Such a direction of deformation is not compatible with any reasonable failure mechanism, considering the geometry of the radar line-of-sight and the geometry of the dam (Figure 18).

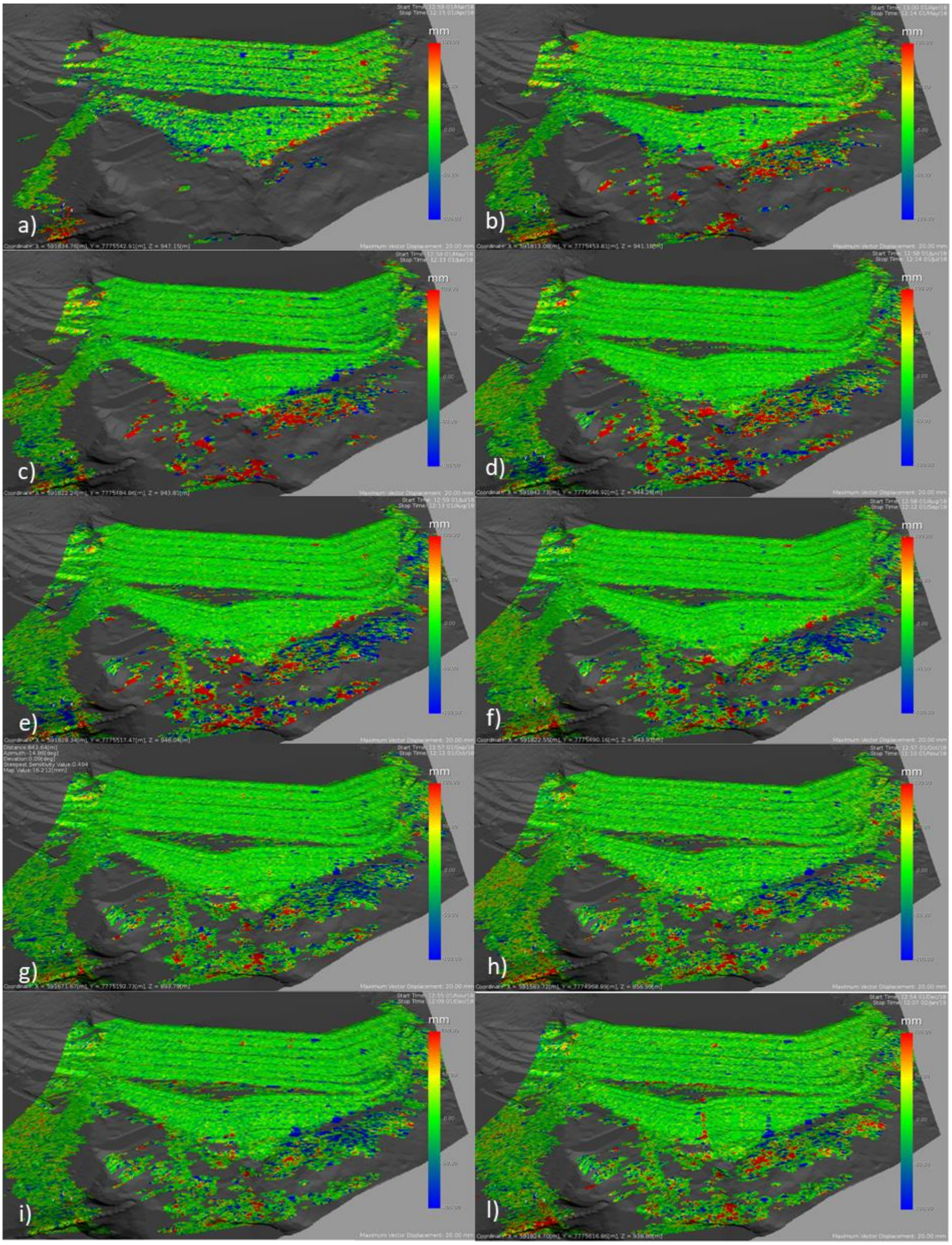

Figure 14: Monthly Cumulative Radar Deformation Maps (Image (a) Corresponds to March 2018 with Subsequent Lettered Images Following Chronologically up to December 2018)

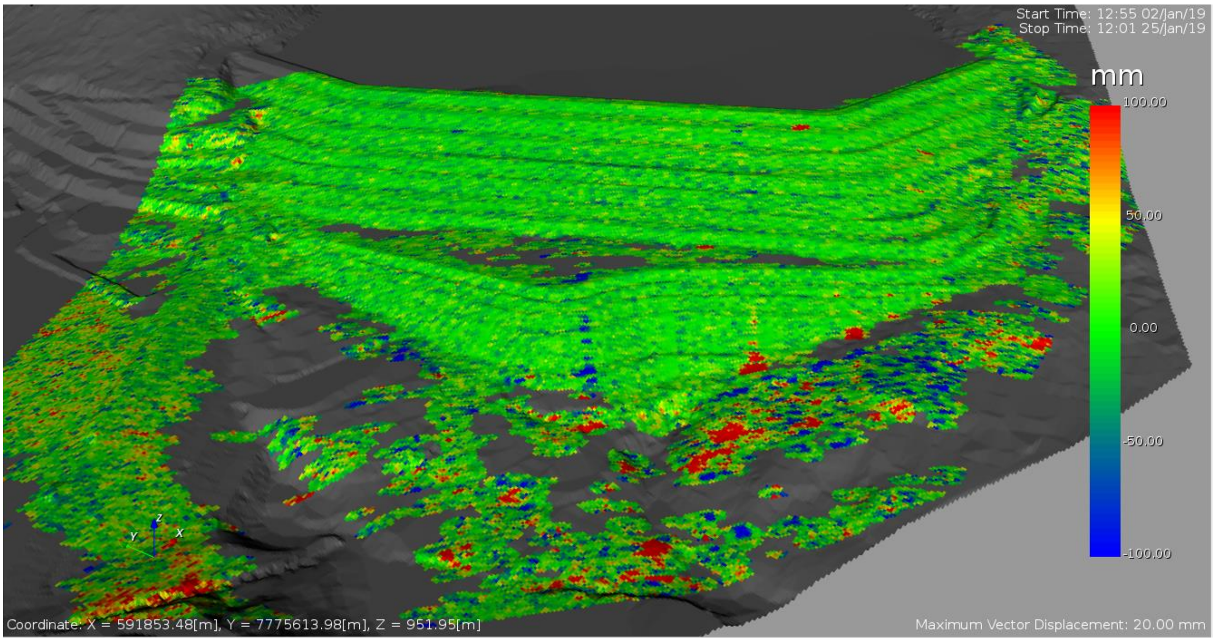

Figure 15: Cumulative Deformation Map From January 2, 2019, to January 25, 2019

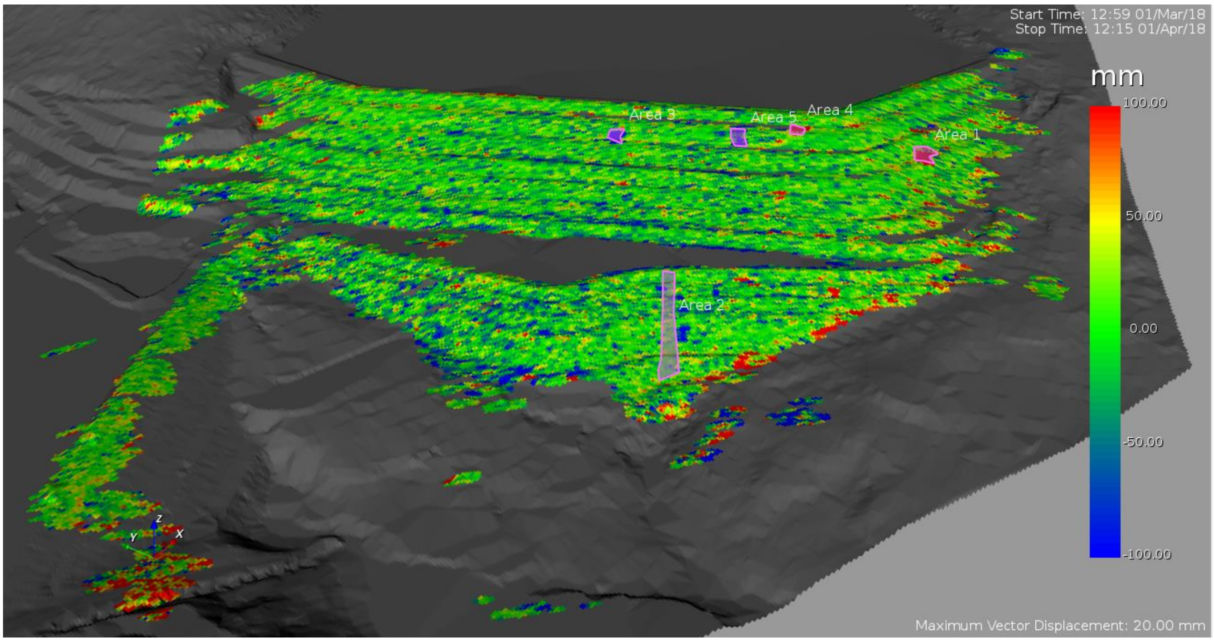

Figure 16: Monthly Cumulative Deformation Map From March 1, 2018, to April 1, 2018

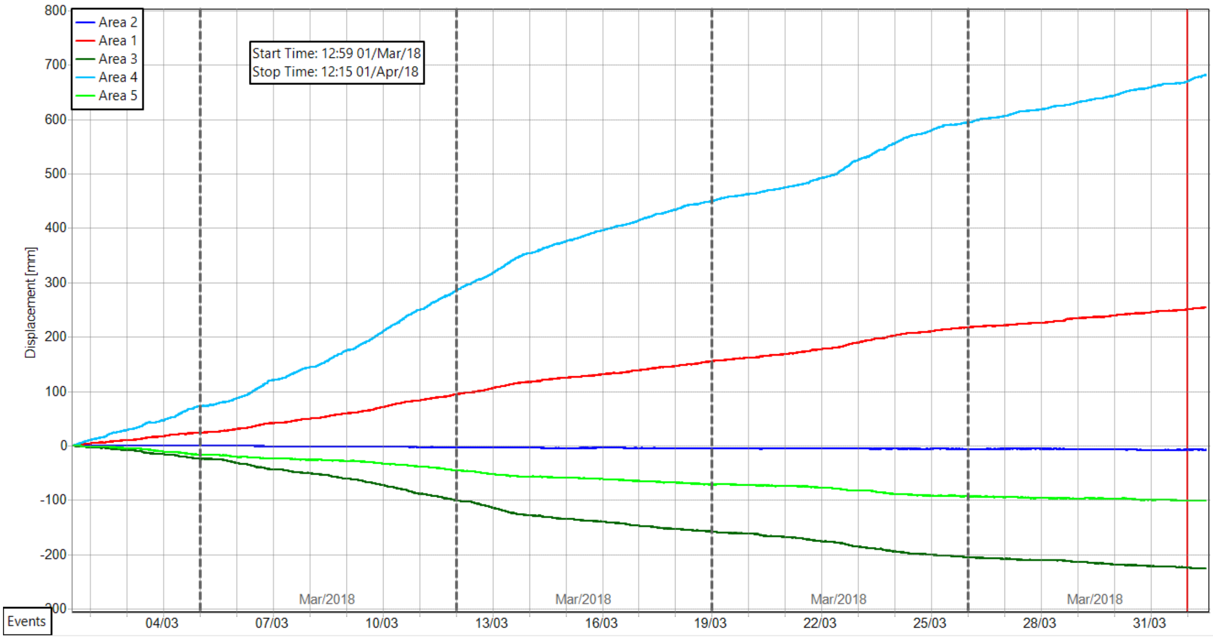

Figure 17: Time Series of Deformation of Selected Areas (As Located on Cumulative Deformation Map in Figure 16)

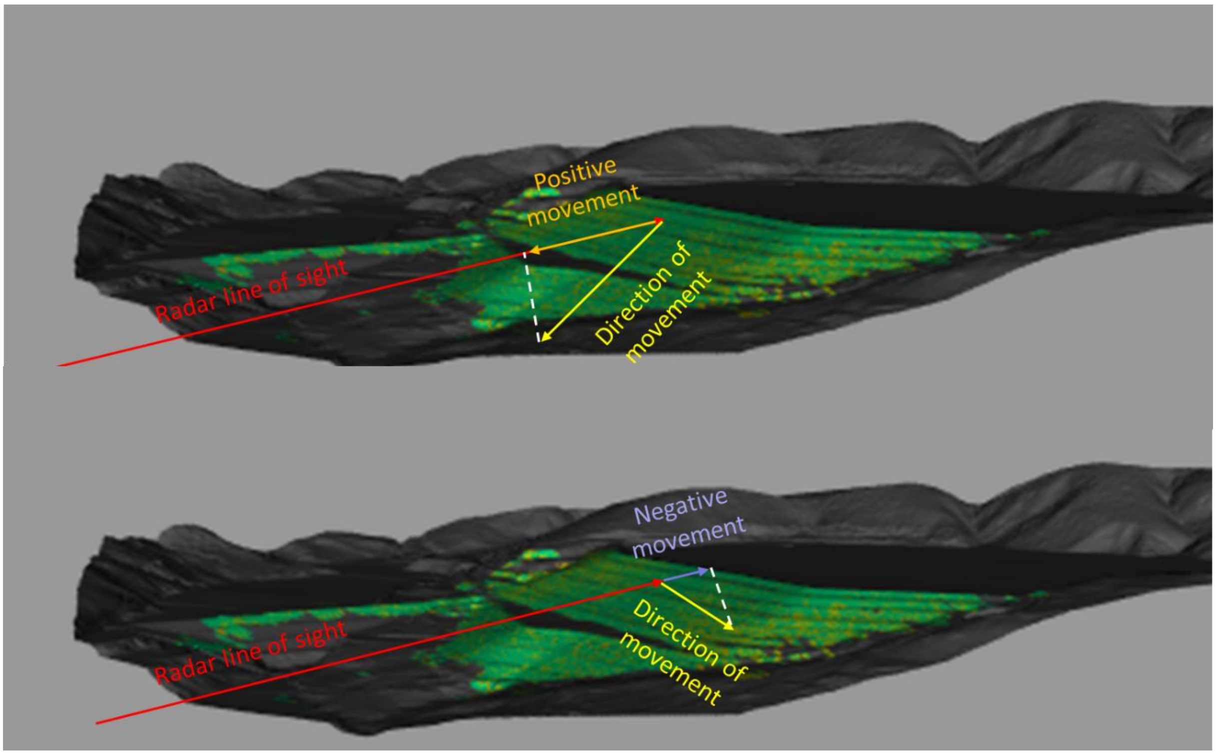

Figure 18: Sketch Showing the Radar Line-of-Sight Geometry and Sign Convention

There also were reports by the ground-based radar of large deformations occurring on the dam during the period from December 2018 up to and including January 18, 2019. The review of the radar data does not identify any deformations above the radar noise level either in the monthly cumulative deformation map from December 19, 2018 to January 19, 2019 (Figure 19), or in the daily cumulative deformation map from January 18 to January 19, 2019 (Figure 20). The radar signal visible in those deformation maps is interpreted as noise induced by vegetation and soil moisture and not actual deformations.

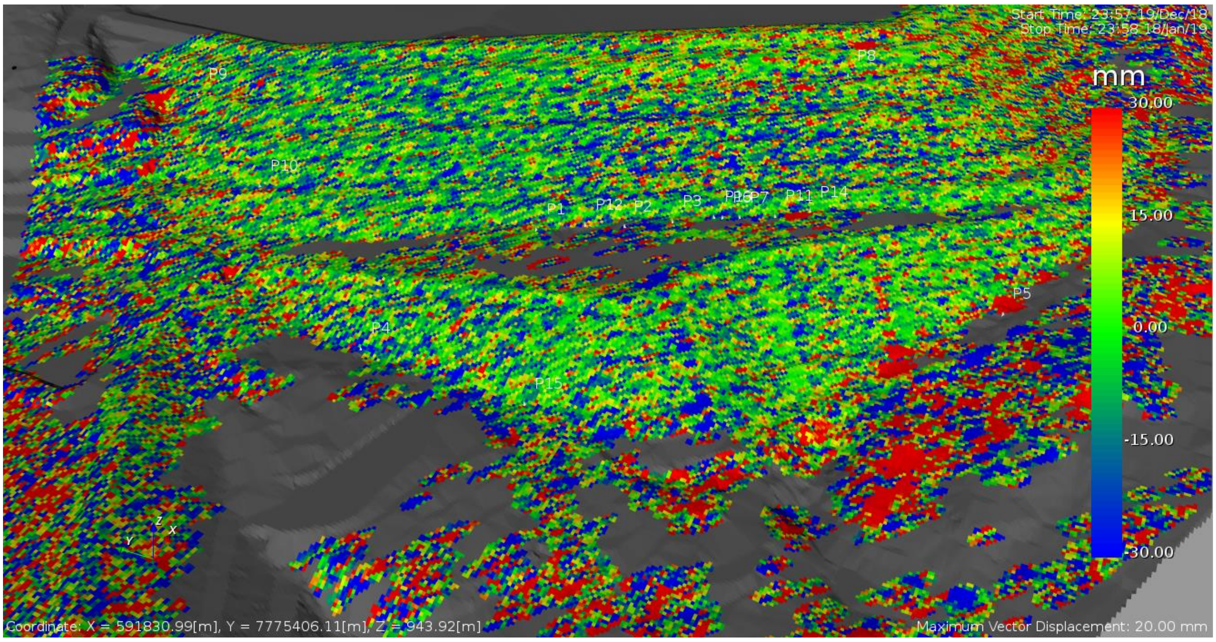

Figure 19: Monthly Cumulative Deformation Map From December 19, 2018 to January 19, 2019

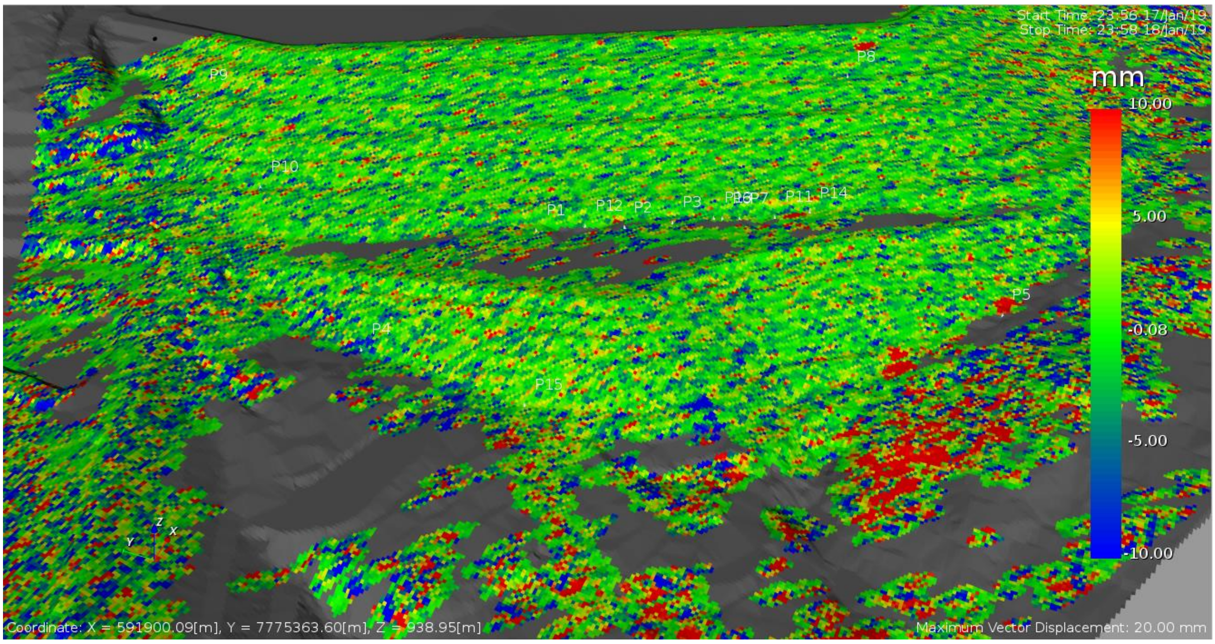

Figure 20: Cumulative Deformation Map From January 18, 2018 to January 19, 2019

As a further proof of the effect attributable to vegetation moisture in reducing the reliability of the radar measurements, the noise level was lowest along the highly reflective concrete surface channels, which indicated no deformation prior to the failure (Figure 21).

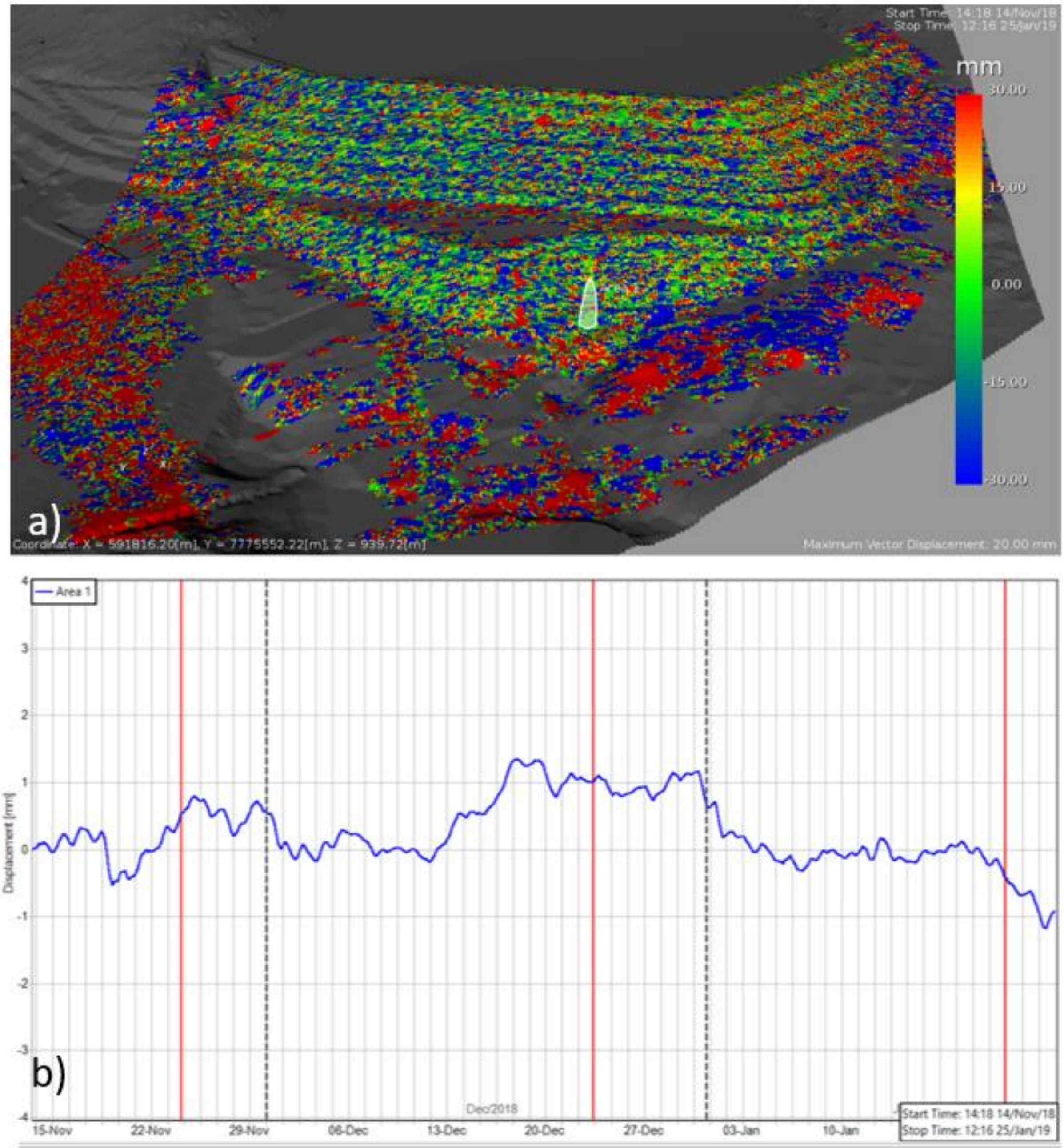

Figure 21: (a) Cumulative Deformation Map for a Concrete Surface Channel From November 14, 2018, to January 25, 2019, and (b) Corresponding Time Series of Deformation

The deformations indicated by the ground-based radar also are not confirmed after a review and analysis of more sensitive satellite data from that same time frame (discussed further below), corroborating this conclusion. Deformations of such intensity as indicated by the monthly deformation maps, if accurate, would have been noted in the InSAR data by a lack of measurement points in correlating areas of the map. However, the InSAR data in those areas reveal good coverage of measurement points (Figure 22 through Figure 25).

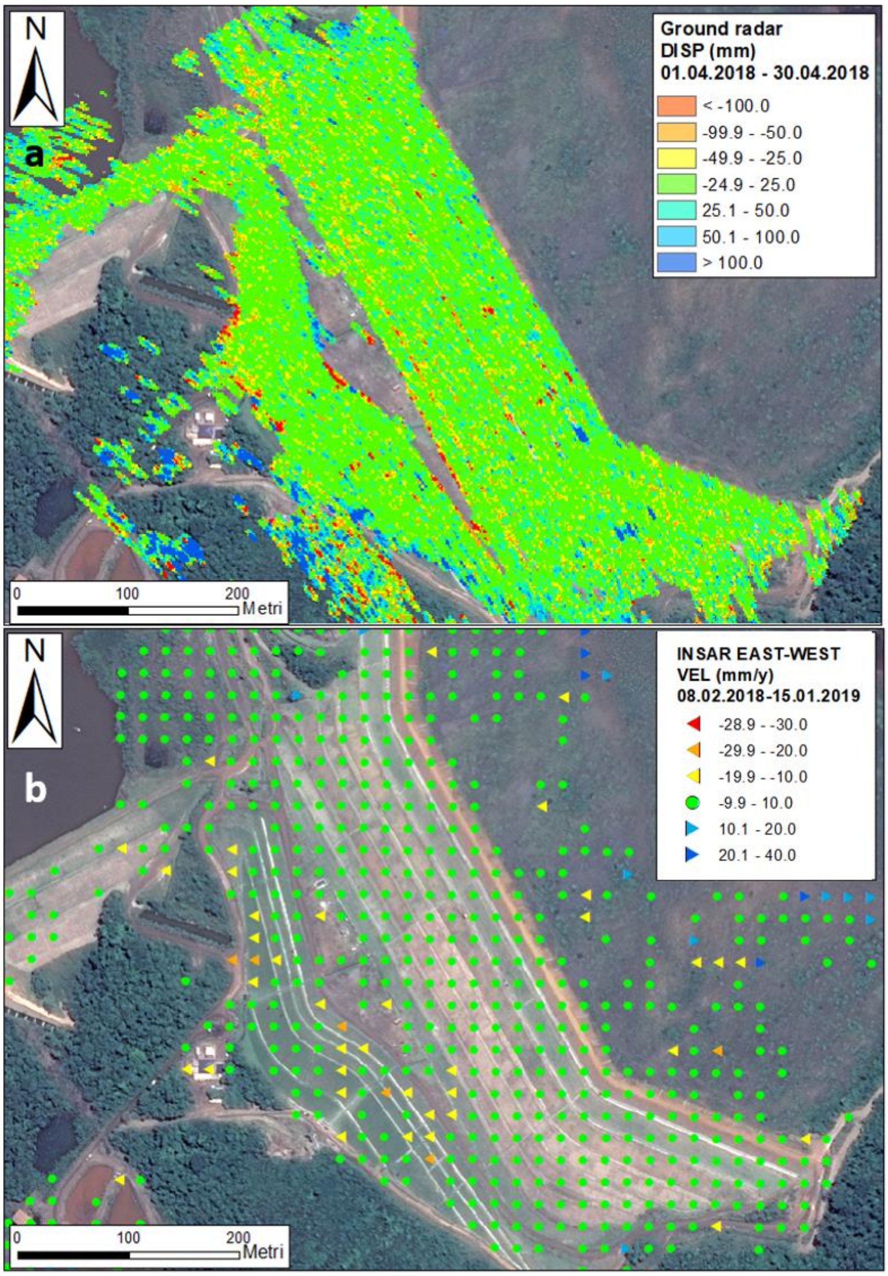

Figure 22: Comparison Between (a) Cumulative Deformation Map From Radar in April 2018 and (b) the E-W Velocity Map Obtained Via InSAR From February 8, 2018, to January 15, 2019

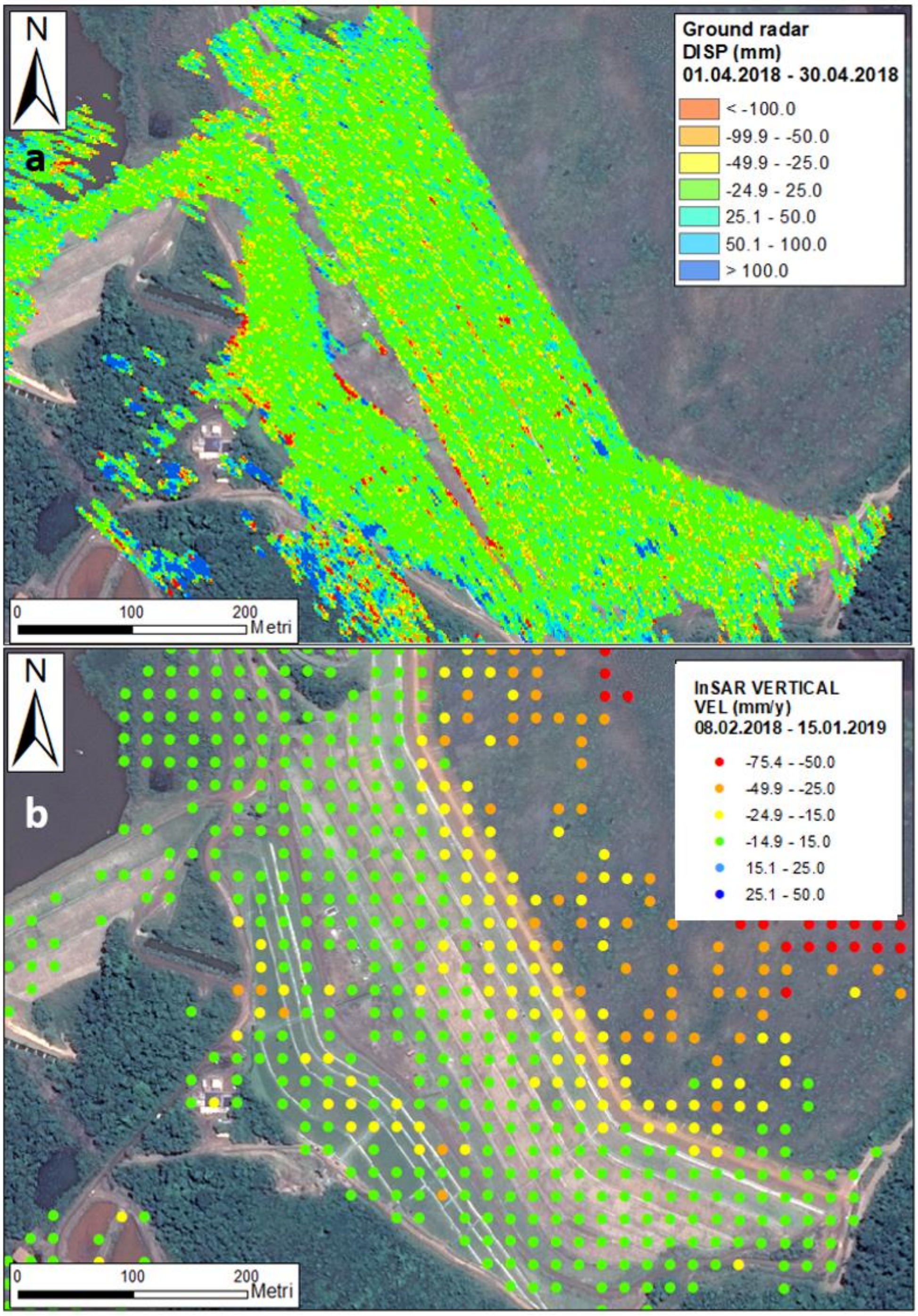

Figure 23: Comparison Between (a) Cumulative Deformation Map From Radar in April 2018 and (b) the Vertical Velocity Map Obtained Via InSAR From February 8, 2018, to January 15, 2019

InSAR data identified deformations on the dam but with a different spatial distribution, having a different geometry (mainly vertical on top of the dam, with a significant horizontal component towards west at the bottom of the dam for InSAR) and with a different range of values (10 millimeters per year (mm/y) to 30 mm/y for InSAR versus 200 mm to 700 mm for the ground-based radar) when compared to those reported by the ground-based radar.

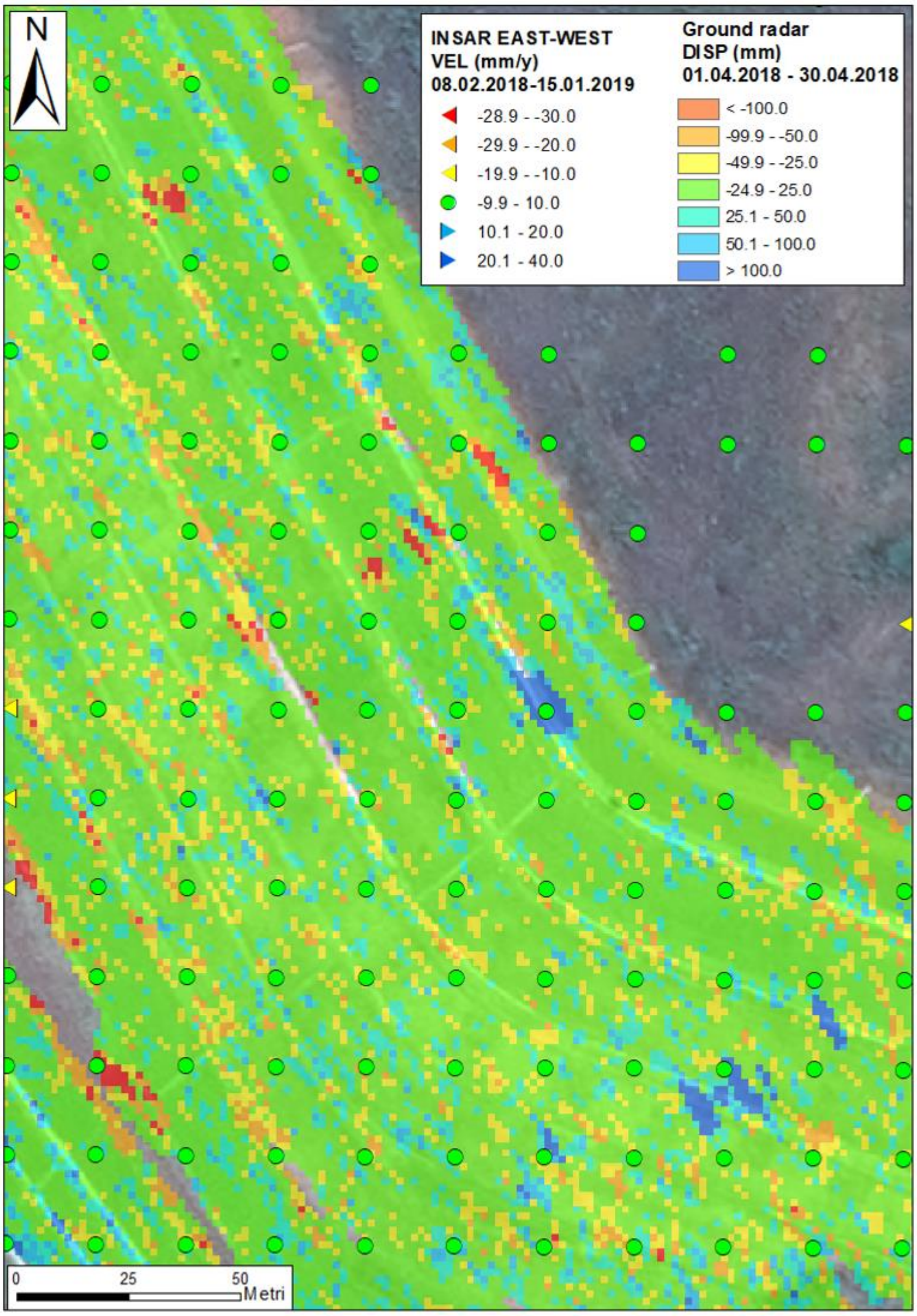

Figure 24: Zoomed-in Image of the Upper Part of the Dam Showing the Cumulative Deformation Map From the Radar in April 2018 and the E-W Velocity Map Obtained Via InSAR From February 8, 2018, to January 15, 2019

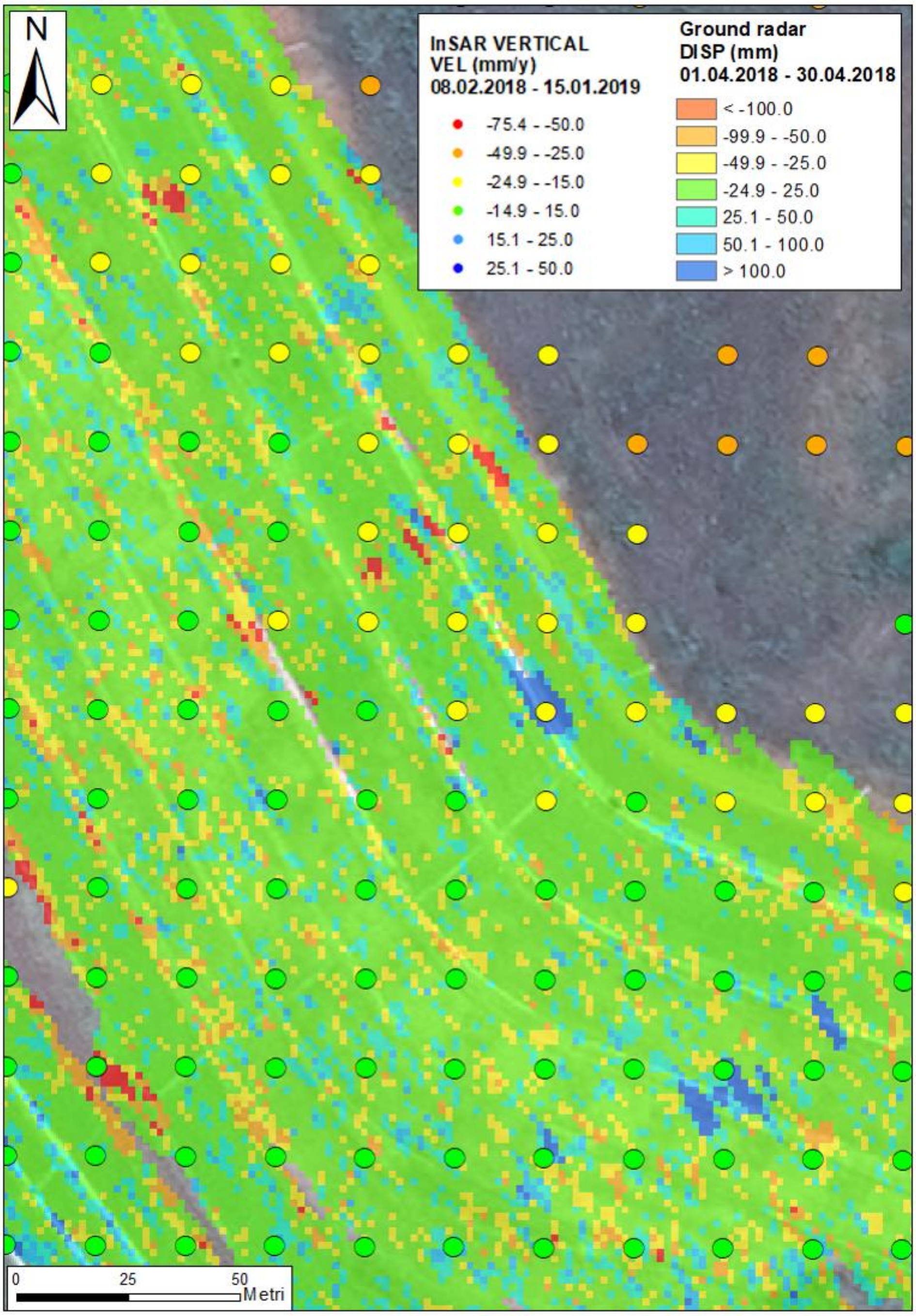

Figure 25: Zoomed-in Image of Upper Part of Dam Showing Cumulative Deformation Map From Radar in April 2018 and Vertical Velocity Map Obtained Via InSAR from February 8, 2018, to January 15, 2019

5.2 DHP 15 Incident

Data collected by the radar on June 11, 2018 were also reviewed in order to verify the occurrence of deformations around the incident encountered in the drilling of deep horizontal drain (DHP) 15 on that day (discussed further in Appendix A).

Small, rapid deformations were recorded by the radar on June 11, 2018 in two areas, Area 1 of around 400 m^2, and Area 2 of around 135 m^2, located in the central part of dam, respectively at a distance around 35 m and 55 m from DHP 15 (Figure 26). In Area 1 positive deformations (towards the radar) started at 1:53 pm, reaching a maximum value in the area of 6.4 mm and an average value of 2.4 mm. From 2:17 pm negative deformations (away from the radar) were measured by the radar until 3:16 pm, with a maximum value of 14.1 mm and an average value in the area of 3.9 mm (Figure 27). Those deformations are compatible with an initial bulging in the area potentially associated with the injection of water and air in the dam during drilling, followed by a contracting process of the dam surface induced by the dissipation of pressure in the ground. In Area 2 the radar recorded only positive deformations (towards the radar) starting at 1:53 pm and ending at 2:46 pm, with a maximum value in the area of 8.3 mm and an average value of 3.6 mm (Figure 27).

All the times are derived from the clock of the PC controlling the radar.

Because these deformations were rapid and occurred in a relatively short period of time, the detected deformations are considered reliable. Notably, the ground based radar did not detect any fast deformations of the type detected in connection with DHP 15 in the months prior to the failure, including during the last radar scan immediately before the visible failure of the dam.

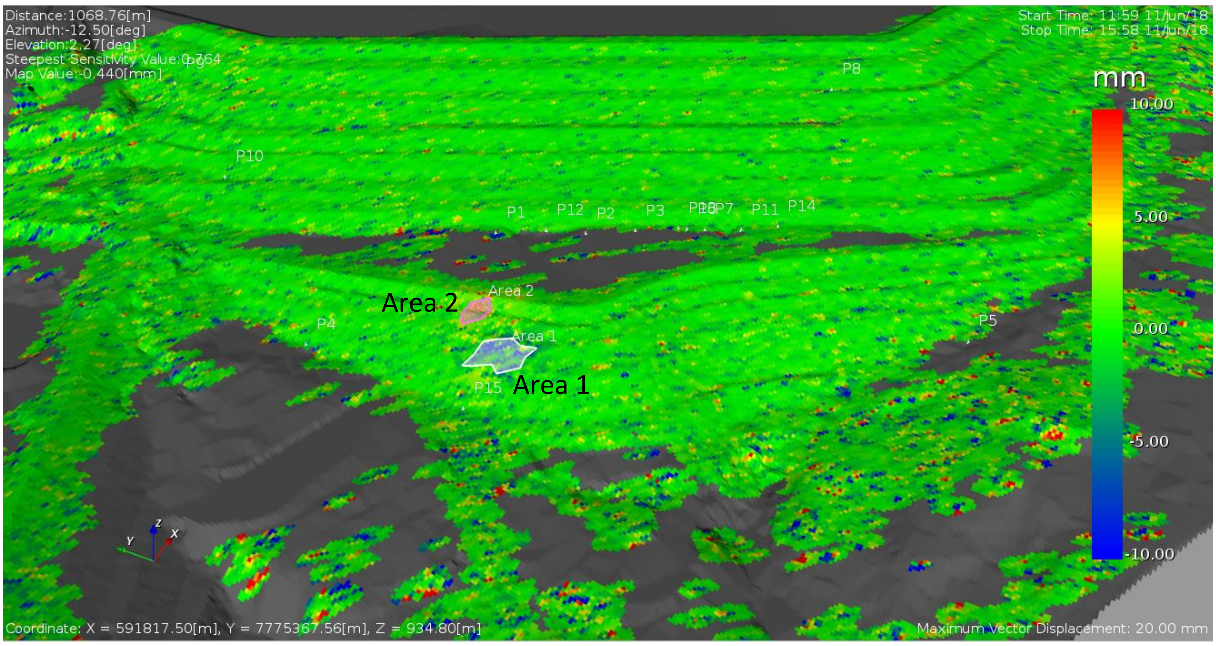

Figure 26: Cumulative Deformation Map from June 11, 2018 11:59 am, to June 11, 2018 3:58 pm

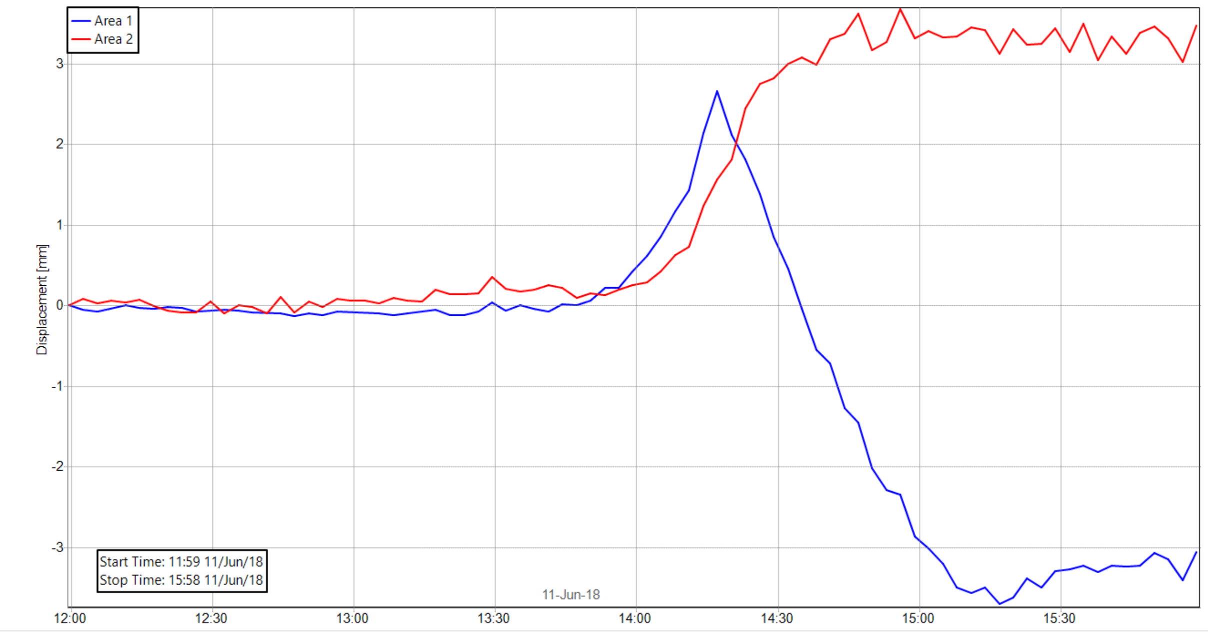

Figure 27: Time Series of Average Deformation of Area 1 and Area 2 from June 11, 2018 11:59 am, to June 11, 2018 3:58 pm

5.3 <u>"Slow Movement" Data</u>

The second review of radar data was performed using a "slow movement" analysis provided by IDS Georadar following the failure. The slow movement processing method uses fewer radar images over the entire period (one image every 24 h), which results in a much lower noise level, potentially providing more reliable deformation data over long time periods.

The "slow movement" analysis did not detect any significant deformation along the radar line of sight above the radar noise or the radar minimum detectable velocity (corresponding to 3 mm/month or 36 mm/day, according to the radar manufacturer IDS Georadar) (Figure 28). In January 2019, a signal slightly above the detectable limit was reported in the lower part of the dam toward the left abutment (Figure 29). However, at 3 mm to 4 mm, this is too close to the minimum detectable velocity to be confirmed as actual deformation. In addition, as noted above, the purported deformations reported by the radar do not correlate with those reported by satellite InSAR.

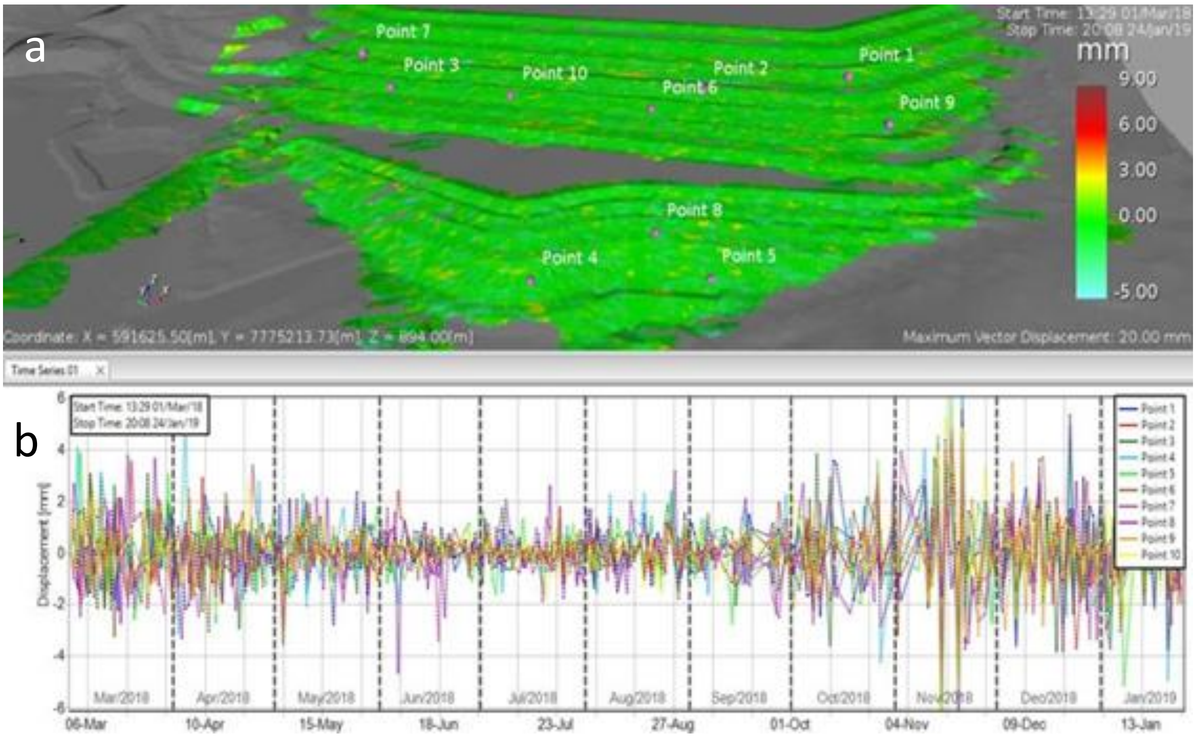

Figure 28: (a) "Slow Movement" Cumulative Deformation Map From March 1, 2018, to January 24, 2019, and (b) Deformation Time Series of Selected Points (as Located on Cumulative Deformation Map)

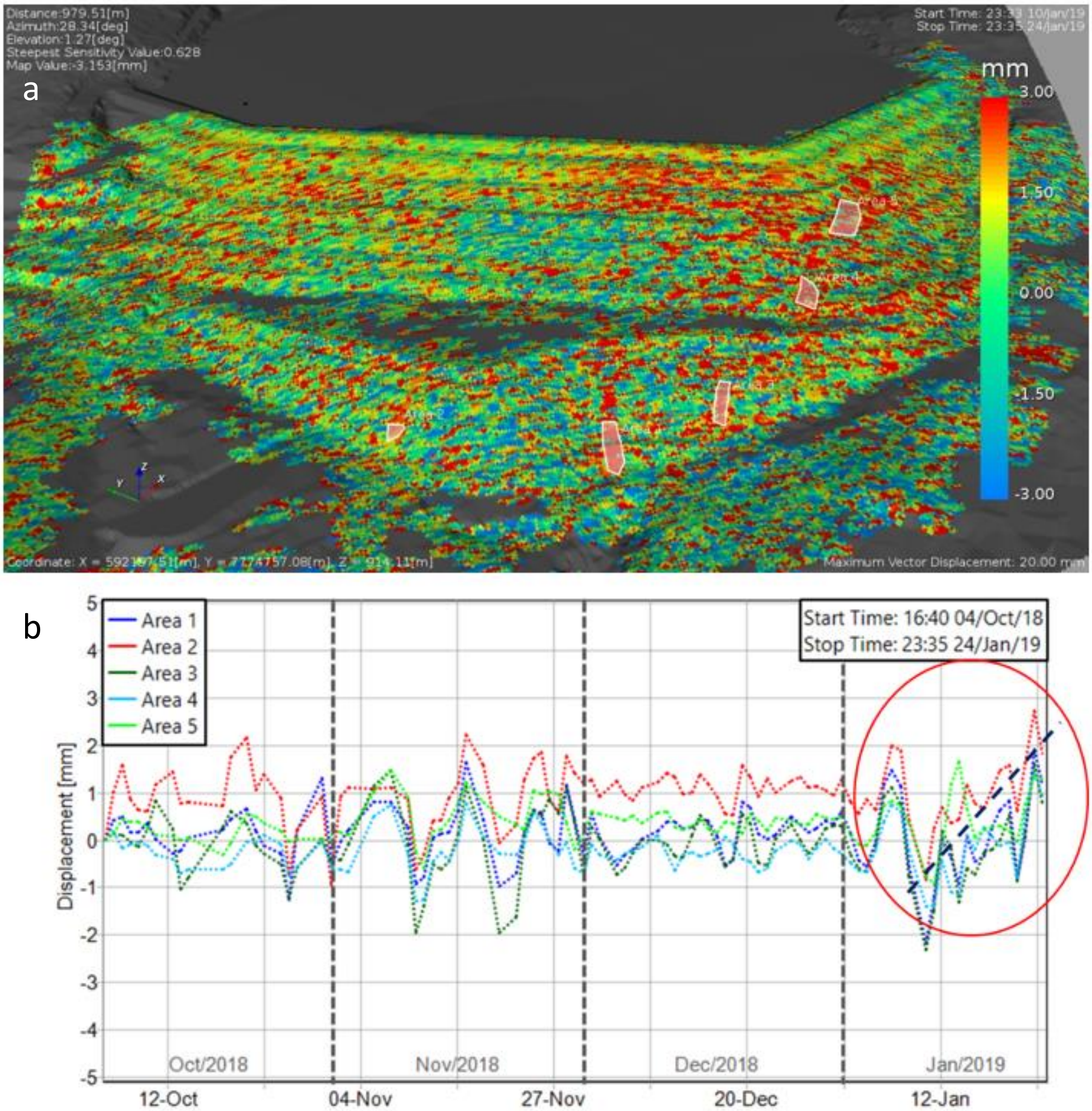

Figure 29: (a) "Slow Movement" Cumulative Deformation Map From October 4, 2018, to January 24, 2019, and (b) Deformation Time Series of Selected Points (as Located on Cumulative Deformation Map)

6. SATELLITE INSAR ANALYSIS

The main objective of this analysis was to review the data provided by satellite InSAR in the year prior to the Dam I failure to understand whether surface deformations were detected and, if so, to analyze their spatial and temporal distributions. InSAR data also were compared to rainfall data to evaluate potential correlations.

The different InSAR datasets analyzed (Sentinel-1 descending (i.e., N to south (S)) orbits, TerraSAR-X ascending (i.e., S to N) orbits, and CosmoSkyMed ascending and descending orbits) are considered to be of good quality, both in terms of point density/area coverage and accuracy of the deformation data. From single satellite geometries (ascending or descending orbits), deformation data along the line-of-sight of the satellites are provided. By combining line-of-sight data provided by ascending orbits with those provided by descending orbits collected in the same period, it was possible to estimate deformation vectors in their vertical and E-W components. InSAR does not measure the N-S component of the deformation vector because ascending and descending line-of-sight are almost perpendicular to the N-S direction, and thus the sensitivity to this direction is very low (~10%).

Sentinel-1 descending data and TerraSAR-X ascending data show good coverage of nearly the entire dam embankment and within the stored tailings. The CosmoSkymed InSAR dataset shows good coverage in the central and upper parts of the dam and within the tailings, but no measurement points are present in the lower part of the dam. Such lack of data could be attributable to the noise in the X-band signal radar data induced by the vegetation coverage on the face of the dam with the longer revisiting time of the satellite (16 days), compared to TerraSAR-X (same frequency band but 11-day revisiting time).

Sentinel-1 is the most informative InSAR dataset because of the almost continuous point coverage over the entire area of interest. Figure 30 shows the average velocity map spanning the entire period covered by the dataset (January 3, 2018, to January 22, 2019) for all the available points in the area (Figure 26a) and only for the moving points (greater than +/- 15 mm/y, Figure 26b).

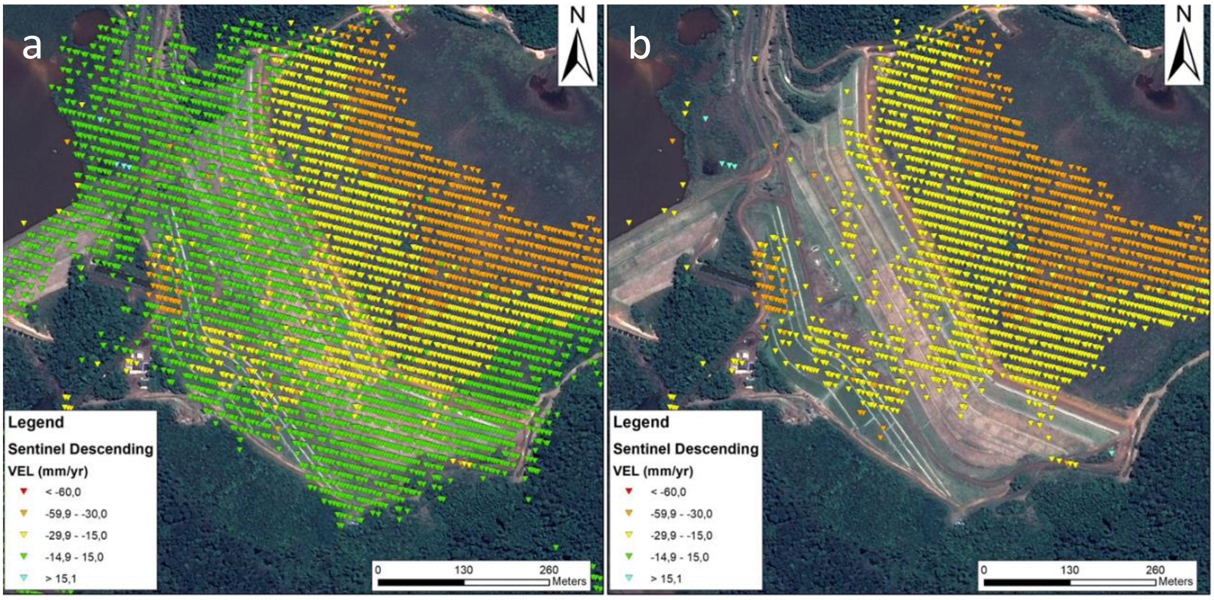

Figure 30: Velocity Map from InSAR Sentinel-1 Dataset From January 3, 2018, to January 22, 2019, Showing (a) All Points and (b) Only Moving Points

6.1 Bottom and Central Part of Dam I

Line-of-sight deformations away from the satellite were detected at the bottom of the dam in three different areas, with vertical and E-W components. The three moving areas at the bottom of the dam show average velocities during the analyzed period ranging between 17 mm/y and 35 mm/y along the descending line-of-sight (Figure 31).

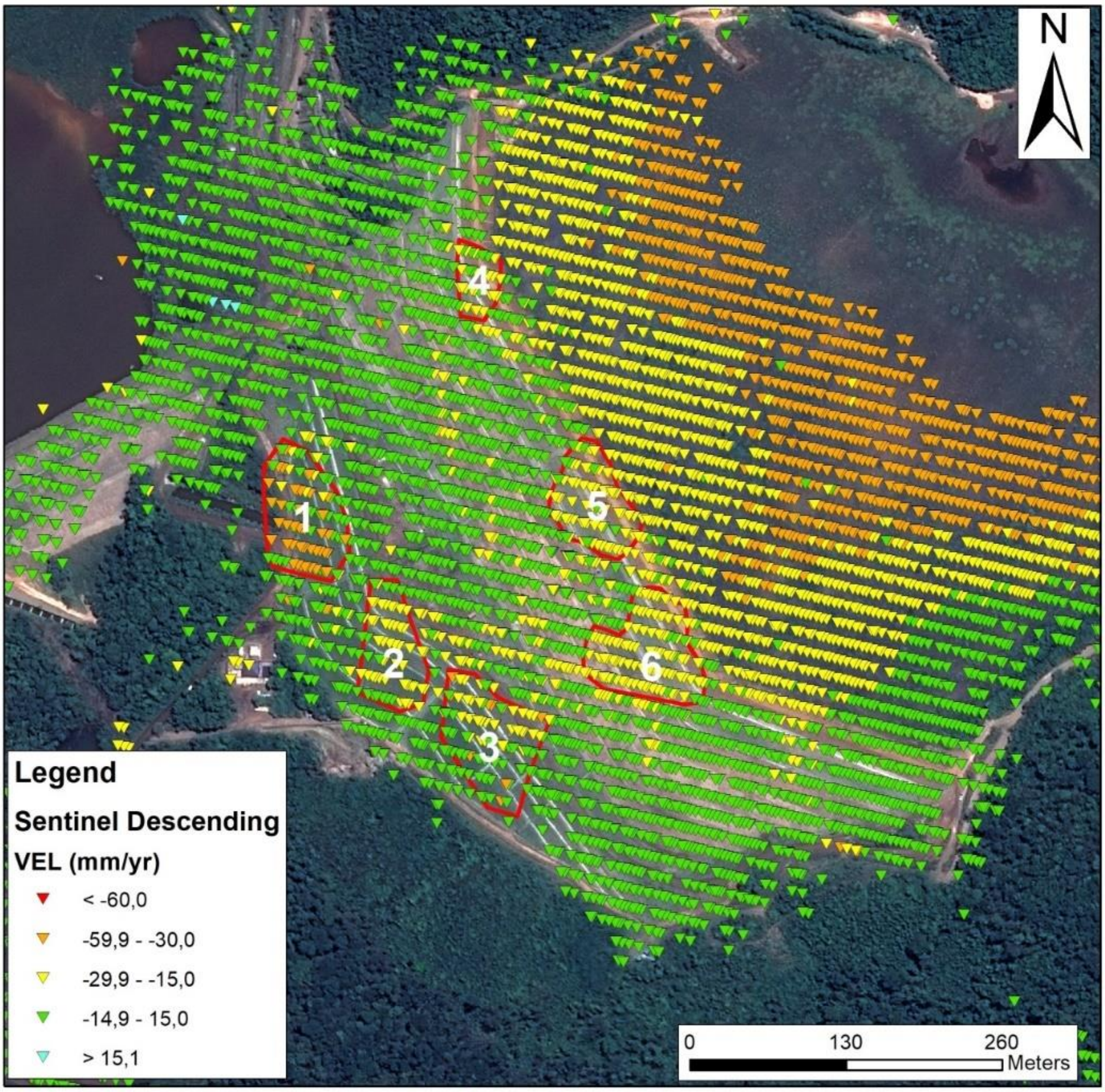

Figure 31: Velocity Map from InSAR Sentinel-1 Dataset From January 3, 2018, to January 22, 2019 (Polygons of Moving Sectors of Dam I are Identified in Red)

The noted deformations are compatible with: (i) vertical settlements, (ii) deformations with horizontal components toward the west (W), or (iii) deformations with both vertical and Westbound components. The InSAR data provided by the TerraSAR-X dataset along ascending geometries confirm the presence of deformations at the bottom of Dam I (Figure 32). When combining their line-of-sight measurements with those of Sentinel-1, as shown in Figure 33, it is possible to confirm the presence of deformations with both a vertical and a westward component at the bottom of Dam I (Figure 34).

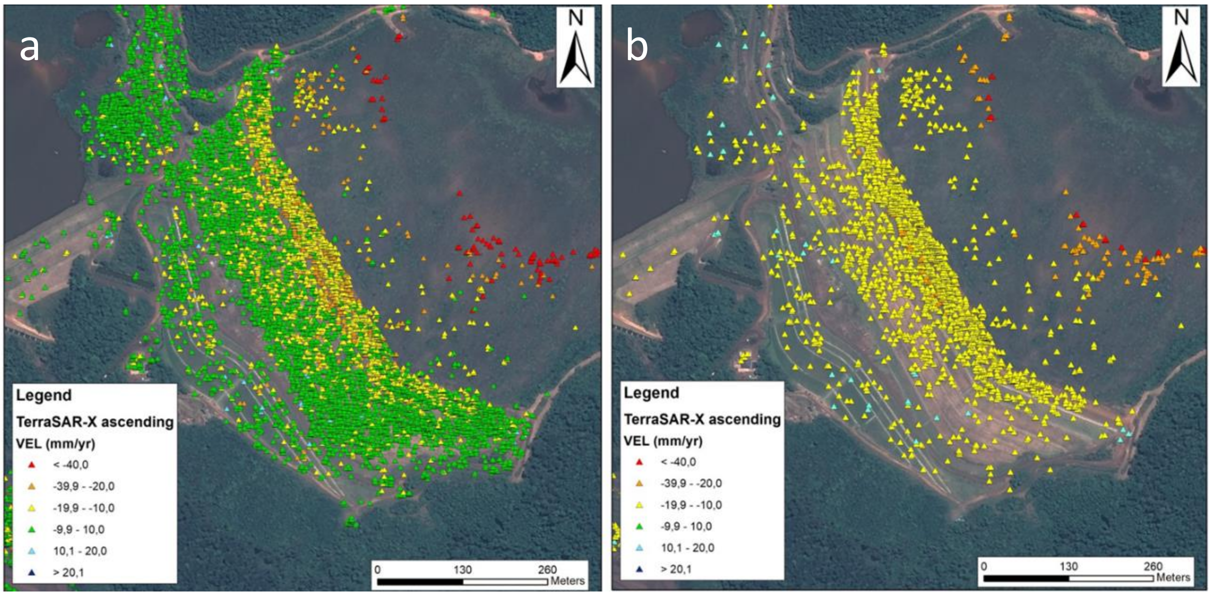

Figure 32: Velocity Map from the InSAR TerraSAR-X Dataset From February 8, 2018, to January 15, 2019, Showing (a) All Points and (b) Only the Moving Points

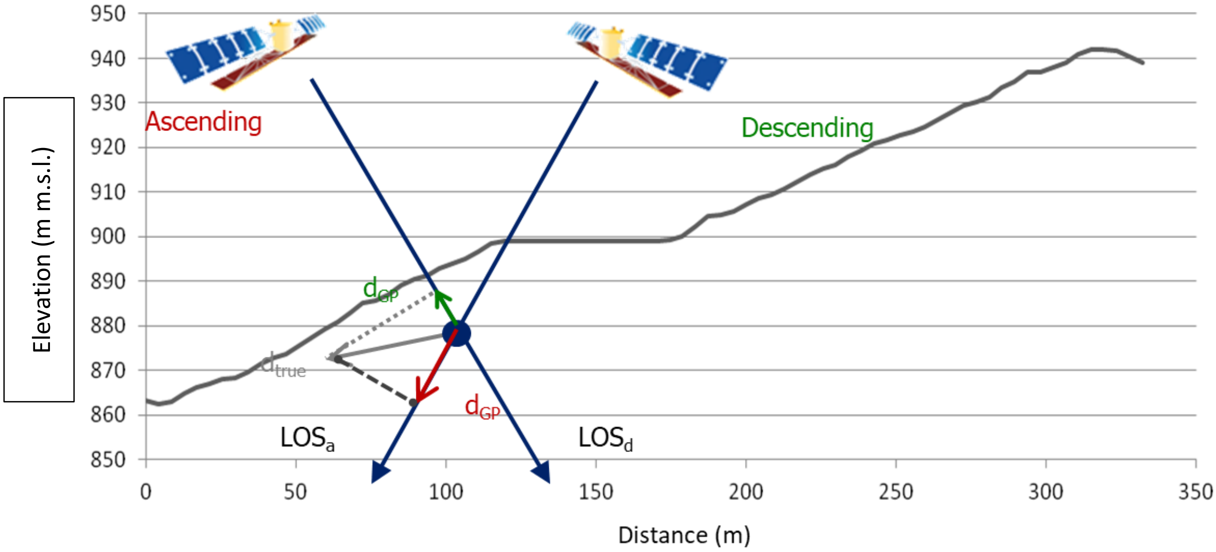

Figure 33: Sketch With a Combination of InSAR Data From Ascending and Descending Orbits Along the Profile of Dam I

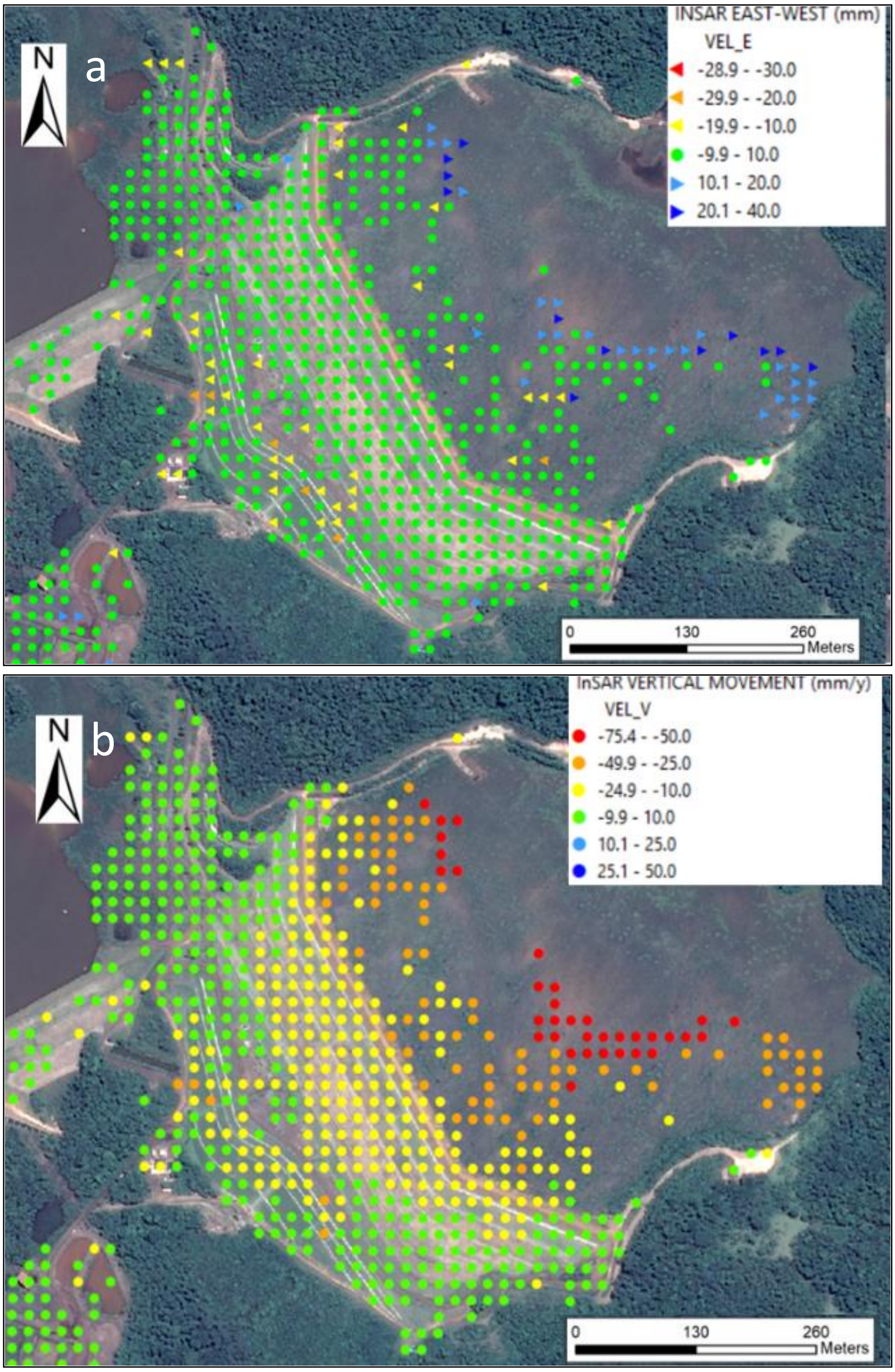

Figure 34: Velocity Map from Decomposed InSAR TerraSAR-X – Sentinel-1 Data: (a) for E-W Components and (b) Vertical Components

In the lower part of the dam the deformations measured by InSAR were mostly less than 10 mm/year, but included areas where the horizontal deformations ranged from 10 to 30 mm/year in the 12 months prior to the failure. It was not possible to confirm the horizontal deformations detected by the Sentinel-TerraSAR-X combined datasets in this sector of Dam I through the ascending and descending CosmoSkyMed datasets because of the lack of measurement points in the lower part of the dam (Figure 35).

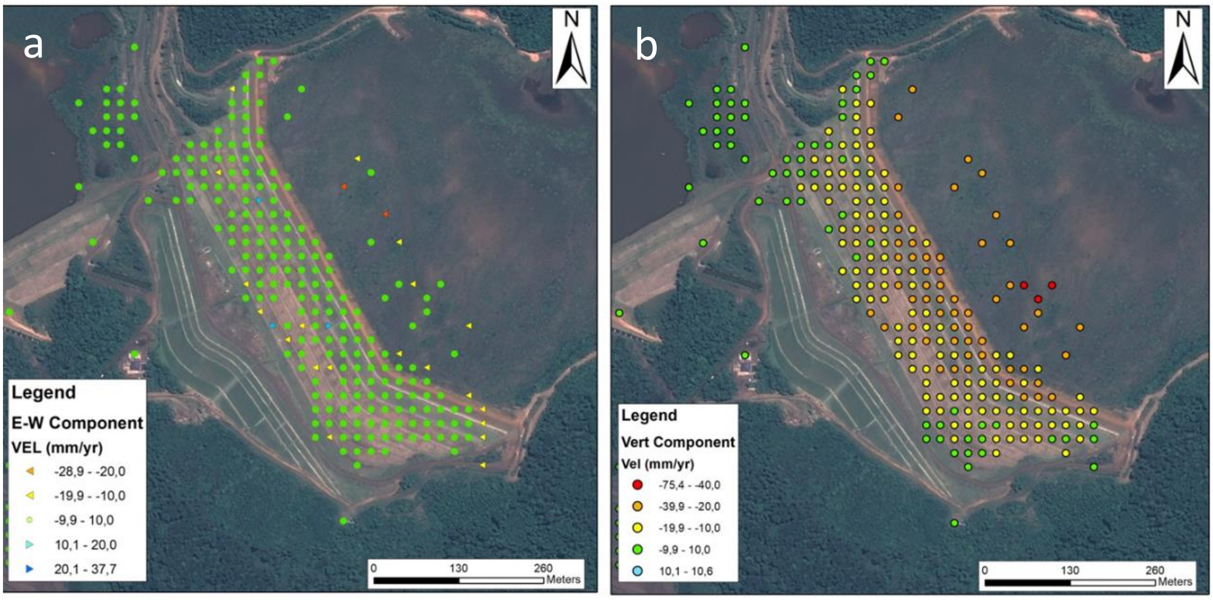

Figure 35: Velocity Map from Decomposed InSAR CosmoSkyMed Datasets for (a) E-W Components and (b) Vertical Components

From Figure 36, it is evident that most of the deformations measured on Dam I occurred in the second part of the analyzed period (i.e., from August 2018 to January 2019).

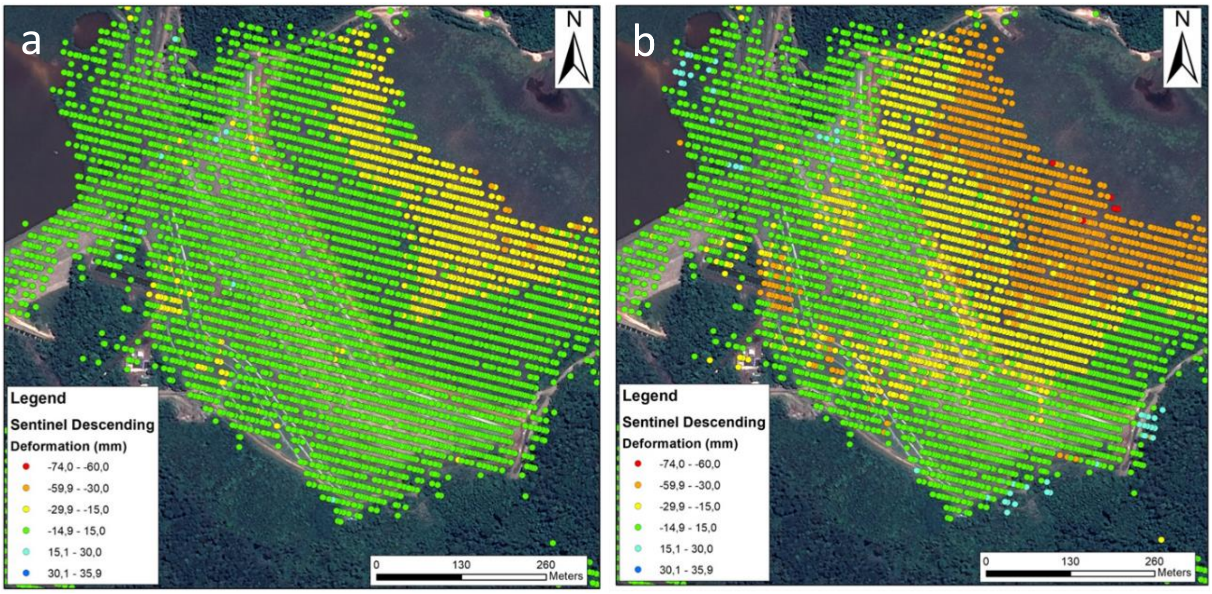

Figure 36: Comparison Between Cumulative Deformations Datasets Measured by Sentinel-1 (a) From January 3, 2018, to August 7, 2018 and (b) From January 3, 2018, to January 22, 2019

By analyzing the temporal series of InSAR measurement points located at the bottom of the dam, deformations are first identified in late March to April 2018, with certain acceleration phases in October and November 2018. A final acceleration occurred from December 2018 to January 2019. These accelerations were observed for most of the InSAR points in this area (Figure 37).

In the central part of Dam I, deformations estimated from all datasets indicate mainly vertical components, showing an increase in velocities starting between September and October 2018 up to the time of the failure.

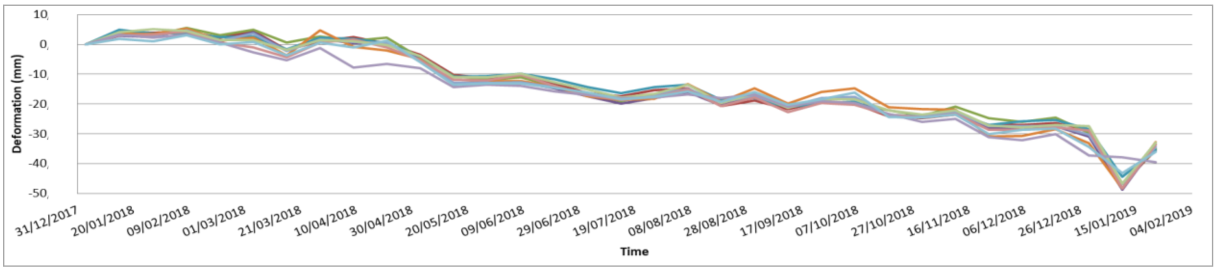

(a)

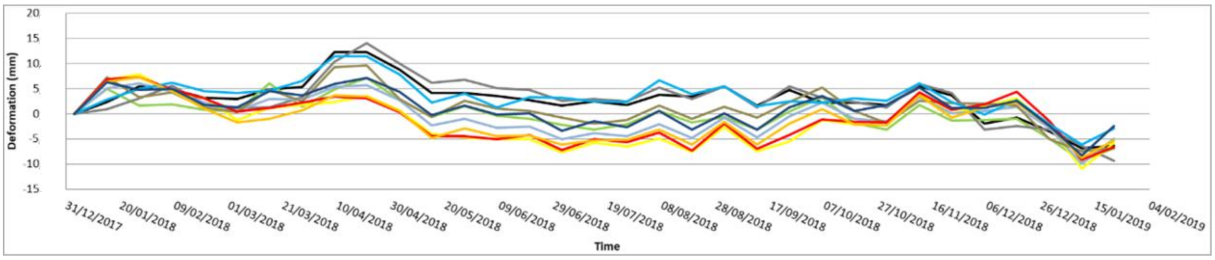

(b)

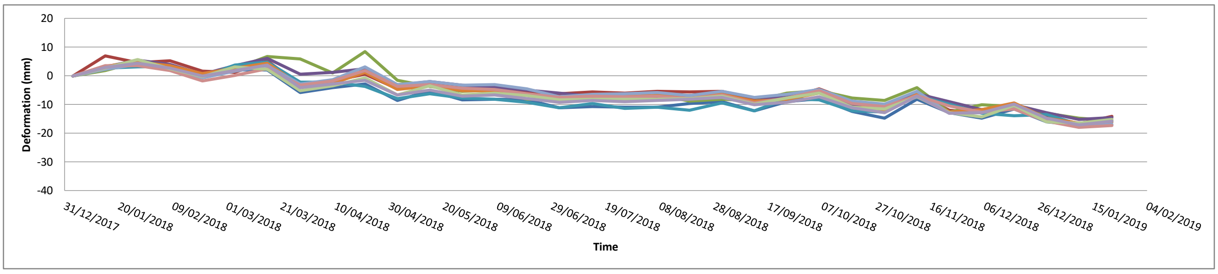

(c)

Figure 37: Deformation Time Series of InSAR Points for Sentinel-1 Data Located at Bottom of Dam I (From Figure 31) for: (a) Area 1, (b) Area 2, and (c) Area 3

Although deformations increased slightly from September to October 2018, none of the points showed a clear progressive acceleration of deformation prior to the failure that would be potentially useful to empirically predict the time of failure (e.g., using the inverse of velocity with time).

6.2 Top of Dam I

On the top of the dam, deformations with mainly vertical components and some minor horizontal components (close to the level of the noise in the data) were detected by all InSAR datasets (Figure 34 and Figure 35), with maximum velocities of 20 mm/y to 22 mm/y.

The measured deformations on the upper part of the dam are linear, with no evident accelerations apart from an increase of velocity from October 2018 and a second velocity increase from the middle of December 2018 until the acquisition of January 10, 2019 of the Sentinel-1 descending dataset (Figure 38). The last two acquisitions of the Sentinel-1 prior to the failure (January 10, 2019 and January 22, 2019) did not indicate any evident acceleration, but confirmed that the deformation reported by the ground based radar on January 18, 2019 (discussed above) was not an actual deformation.

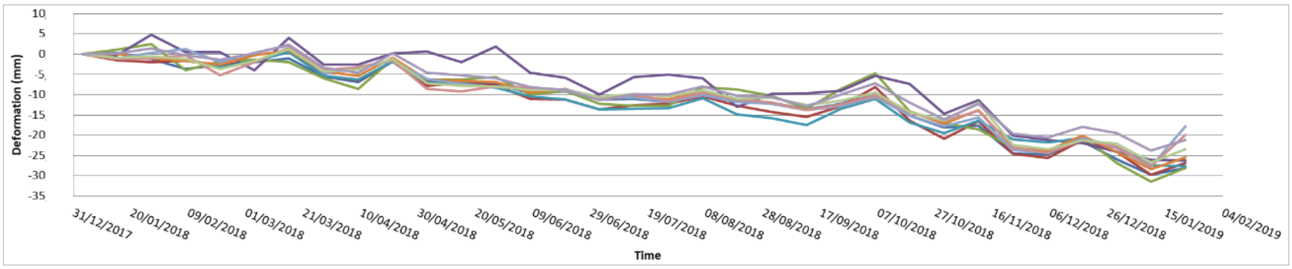

Figure 38: Deformation Time Series of InSAR Points for Sentinel-1 Dataset Located at Top of Dam I Belonging to Area 5 of Figure 31

6.3 <u>Tailings</u>

In the tailings, the maximum deformations measured from the InSAR datasets were up to 140 mm/y along the descending line-of-sight, with mainly vertical components and an almost linearly increasing gradient moving away from the dam crest. Deformations were inclined slightly toward the west close to the dam and toward the east far from the dam.

The deformations measured in all the tailings InSAR datasets align in terms of geometry and magnitude. The dominant deformations in the tailings can be attributed to consolidation, with some accelerations possibly associated with the 2018 wet season.

The maximum deformations measured in the tailings over the last year prior to the failure did not coincide with the maximum depth of tailings, but were located far from the crest of the dam. It is difficult to separate ongoing consolidation of the tailings from deformation of the dam, based on the time period of the InSAR data available. Ongoing consolidation would be expected to decrease with time, while deformation of the dam would be expected to accelerate towards the time of failure. Given that no acceleration is present here, it appears that the detected deformations are associated with the consolidation process.

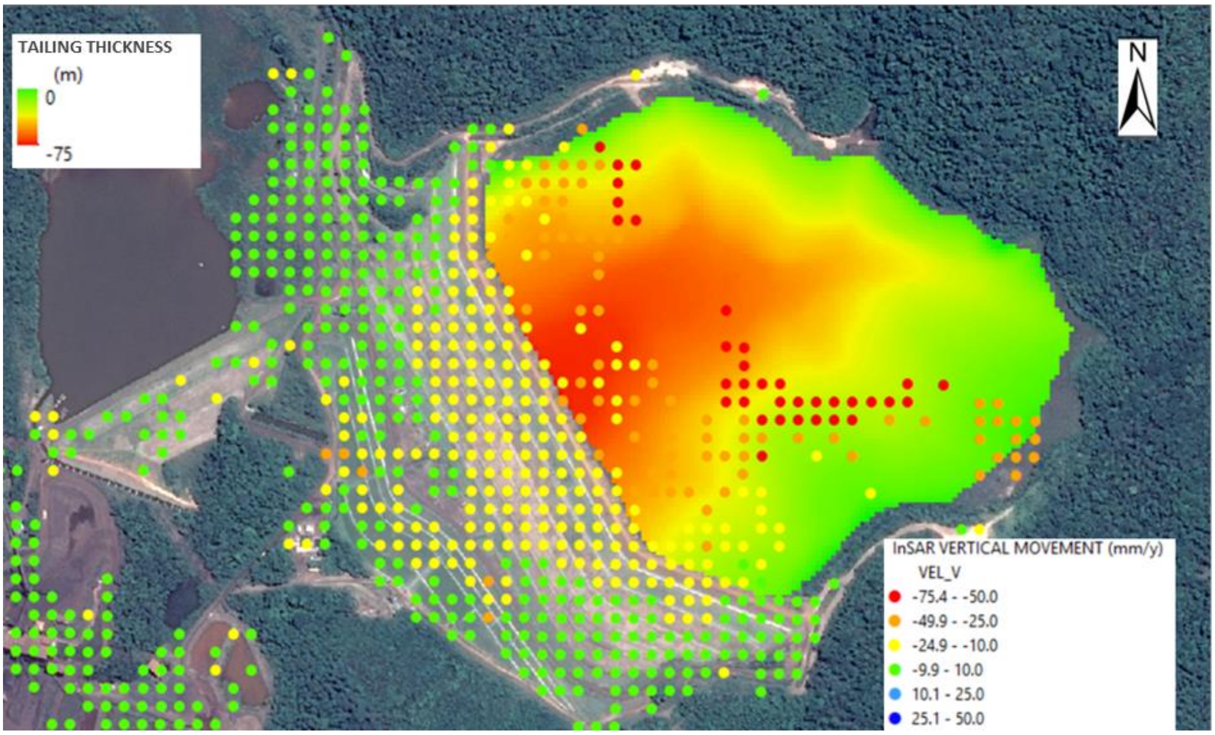

Figure 39: Vertical Velocity Map From InSAR Visualized Over Thickness of Tailings

6.4 Cross-Sections

To obtain a better understanding of the geometry of the deformations indicated by the satellite InSAR datasets, three cross-sections through the dam were drawn on the pre-failure topography (Figure 40), and the deformation vectors were measured using InSAR by combining the ascending and descending line-of-sight data, as visualized in Figure 41 through Figure 43. The deformation vectors inferred from InSAR do not include the N-S component, since the line-of-sight of both ascending and descending orbits is almost perpendicular to that direction which, considering the direction of the cross-sections, could introduce a bias in the direction of the vectors.

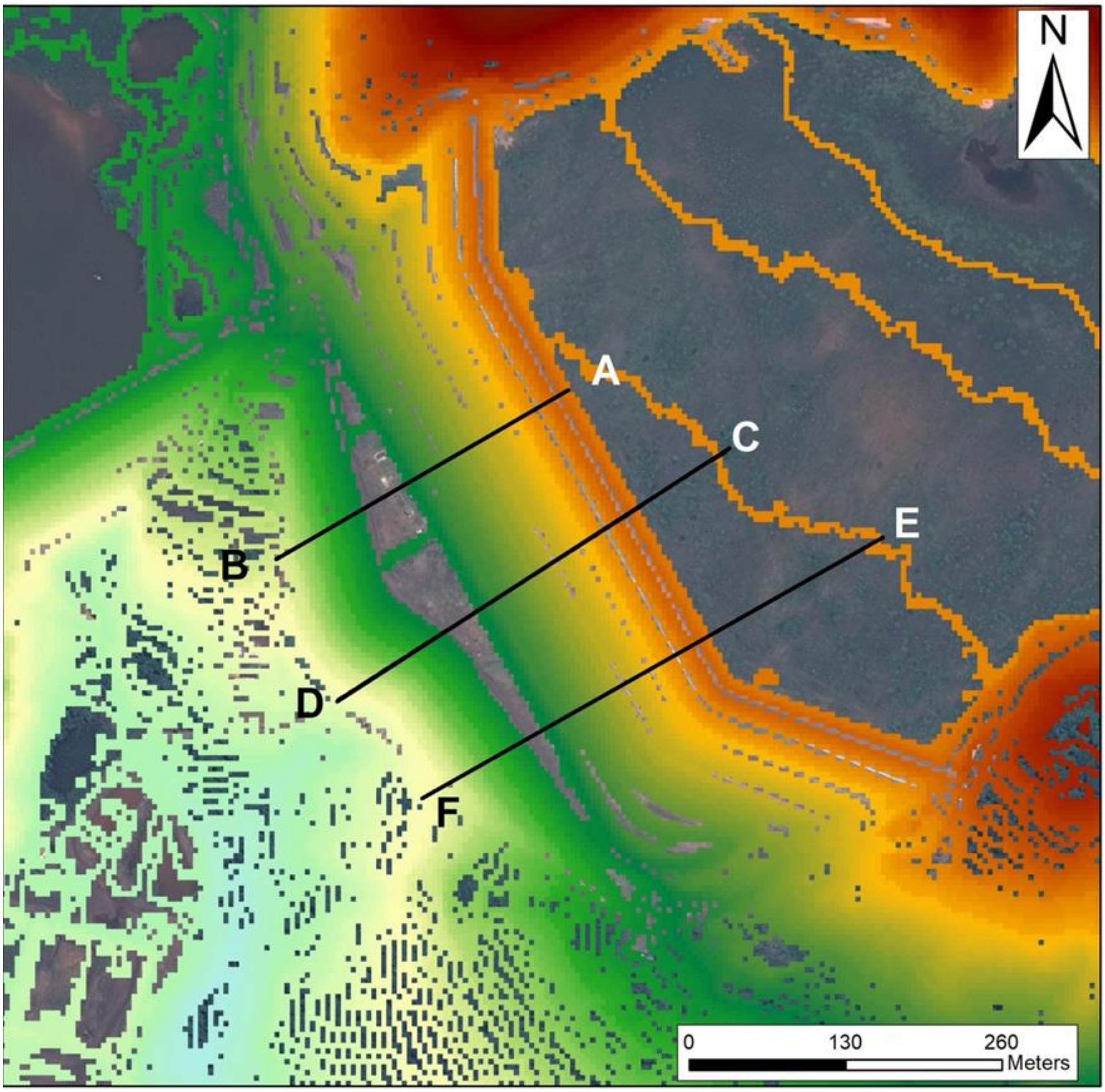

Figure 40: Topography of Dam I Before Failure Showing Locations of Three Cross-sections

In all cross-sections, the deformation of the dam's crest is mainly vertical, while towards the toe of the dam the vectors dip towards the West and their inclination gradually increases up to a maximum angle of ~60° from the vertical, as shown in cross-section EF (Figure 43).

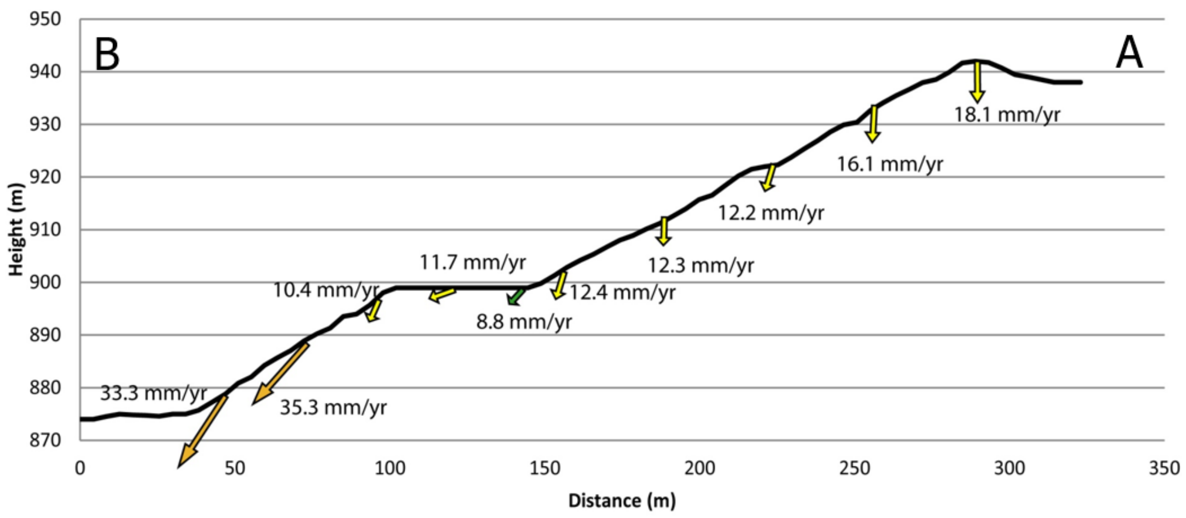

Figure 41: Cross-section AB Showing the Deformation Vectors Obtained From InSAR TerraSAR-X-Sentinel-1 Data

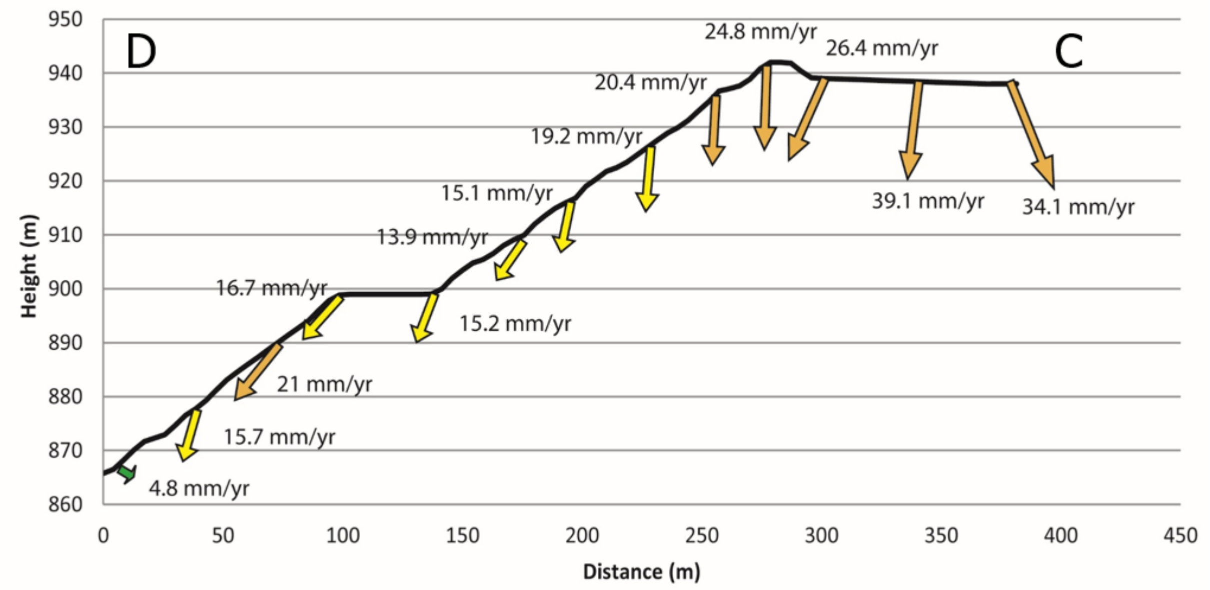

Figure 42: Cross-section CD Showing Deformation Vectors Obtained From InSAR TerraSAR-X-Sentinel-1 Data

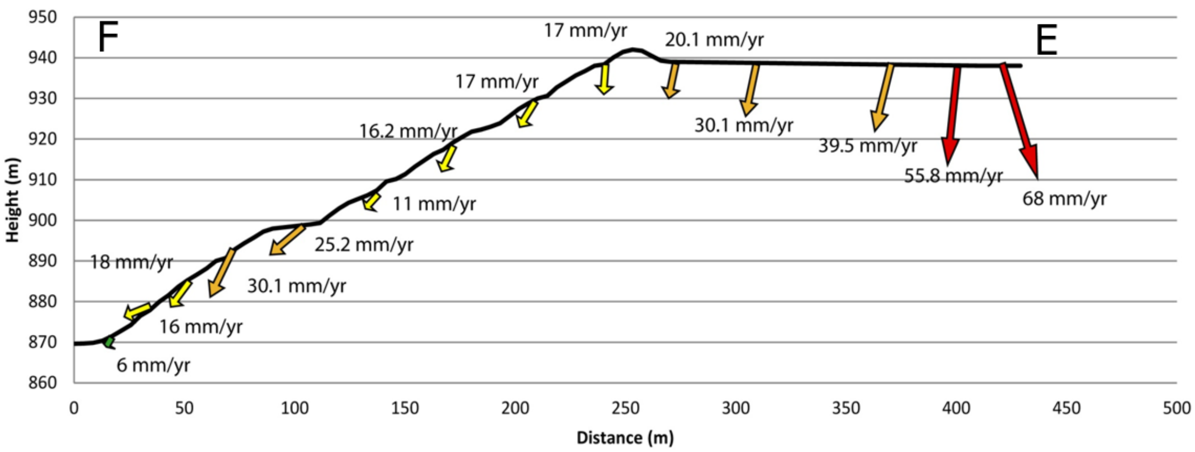

Figure 43: Cross-section EF Showing Deformation Vectors Obtained From InSAR TerraSAR-X-Sentinel-1 Data

By analyzing the cumulative deformation obtained from the InSAR data along the cross-sections divided into four temporal subsets of the entire period covered by the data, it is possible to visualize the temporal evolution of the deformations with an increase in the cumulative deformation more evident in the last three months (Figure 44).

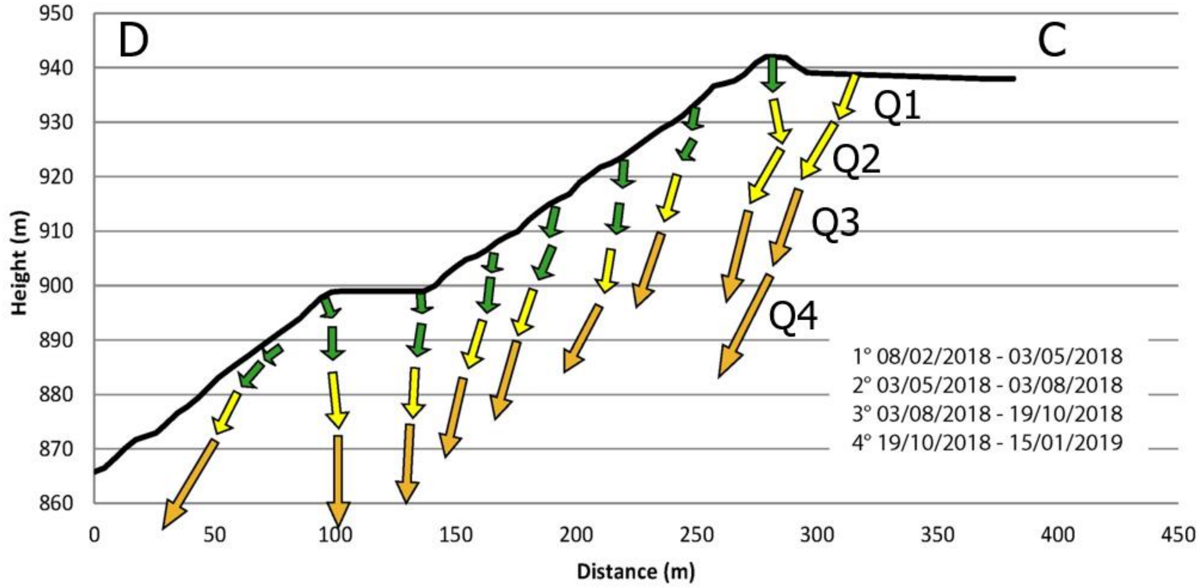

Figure 44: Cross-section EF Showing Deformation Vectors Obtained From InSAR TerraSAR-X-Sentinel-1 Data for Different Sub-periods of the Entire Time Span Covered by Datasets

6.5 Comparison Between InSAR and TWI

InSAR data have been compared to TWI. TWI was calculated based on the pre-dam topography to estimate the water flow before dam construction. High values of TWI indicate that water is accumulating. The spatial distribution of the TWI values in the analyzed area shows that the flow accumulation obtained by calculating the TWI with the original topography is concentrated at the southern part of the toe of the dam where the dam face is exposed to the SW. By comparing the TWI values with the InSAR data (Figure 45), it is possible to observe that most of the deformations identified by the InSAR analysis prior to failure at the bottom of the dam are located in the same sector of the pre-dam topography where the highest values of TWI were identified.

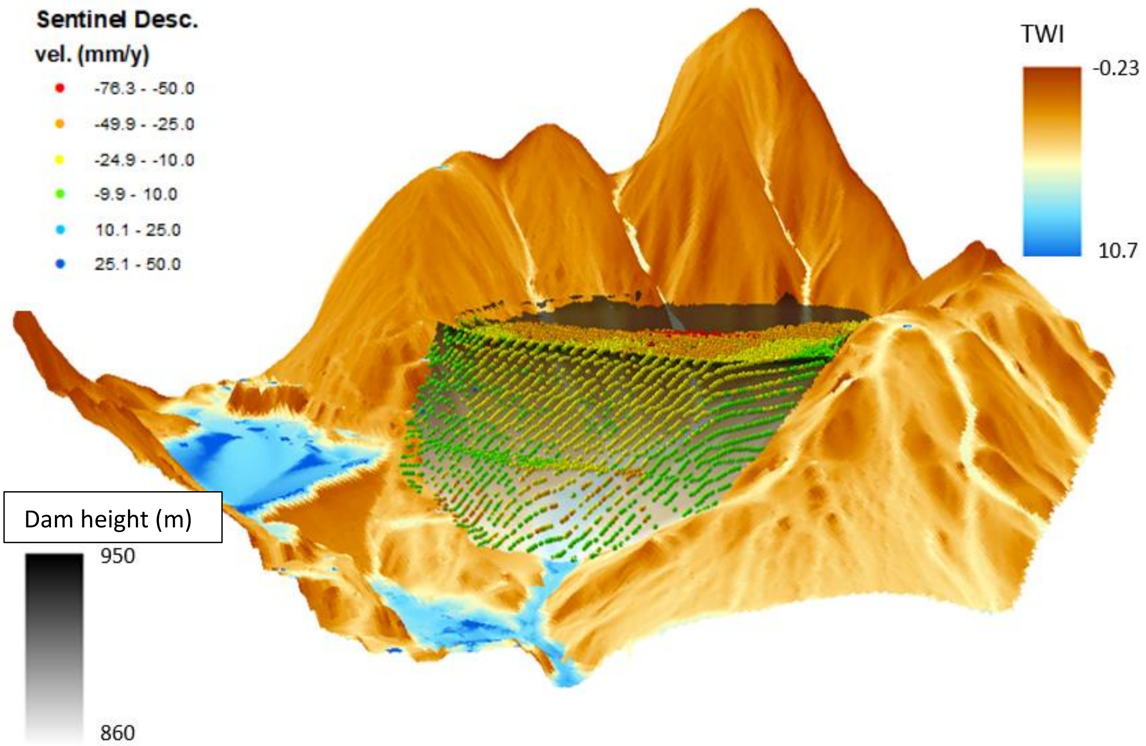

Figure 45: 3D View of Satellite InSAR Data Visualized Over Dam and TWI

6.6 Comparison Between InSAR and Rainfall

Rainfall data from the F18 rain gauge (details set forth in Appendix C) were compared with InSAR data to identify possible temporal correlations between the deformations measured from early 2018 to that measured at the time of the collapse (including the rainy season).

The comparison was done using the Sentinel-1 dataset and the E-W and vertical components obtained from Sentinel-1 and TerraSAR-X. These datasets were chosen as the most representative of the detected deformations before the event, especially in the lower part of the dam.

Time series of deformations considered representative of different sectors of the area of interest have been compared with:

- daily rainfalls;
- monthly rainfalls; and
- cumulative rainfalls.

The comparison between the InSAR data and the rainfall data shows a good correlation between the periods of intense rainfall and the accelerations measured in the InSAR data for the measurement points belonging to the dam (at the bottom and at the crest).

In particular, most of the points at the bottom (Figure 46) and on the crest of the dam (Figure 47) show that where rainfall was low from May to September 2018, there was limited deformation. During the period beginning October 2018 when rainfall increased, accelerations are recorded. The deformations in the tailings are less correlated with rainfalls than those on the dam, showing an almost linear trend with a few slight acceleration periods only partially associated with rainfall events (Figure 48).

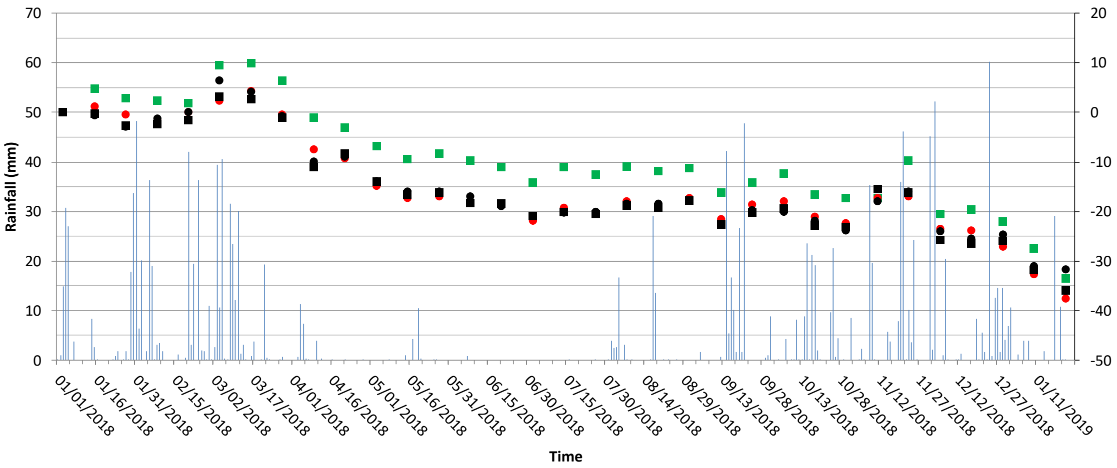

(a)

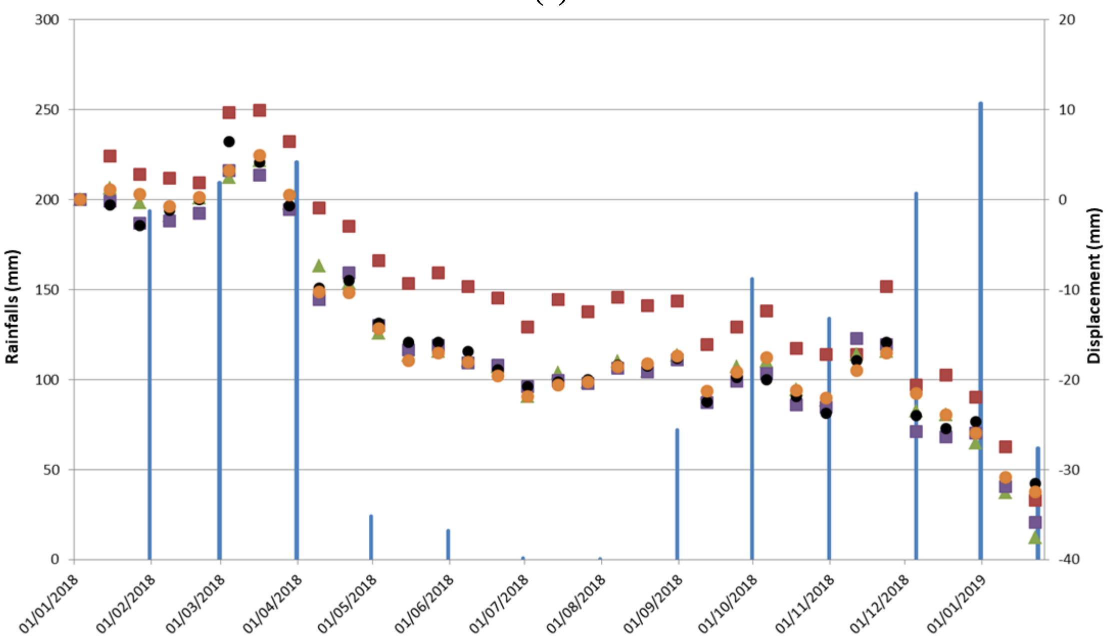

(b)

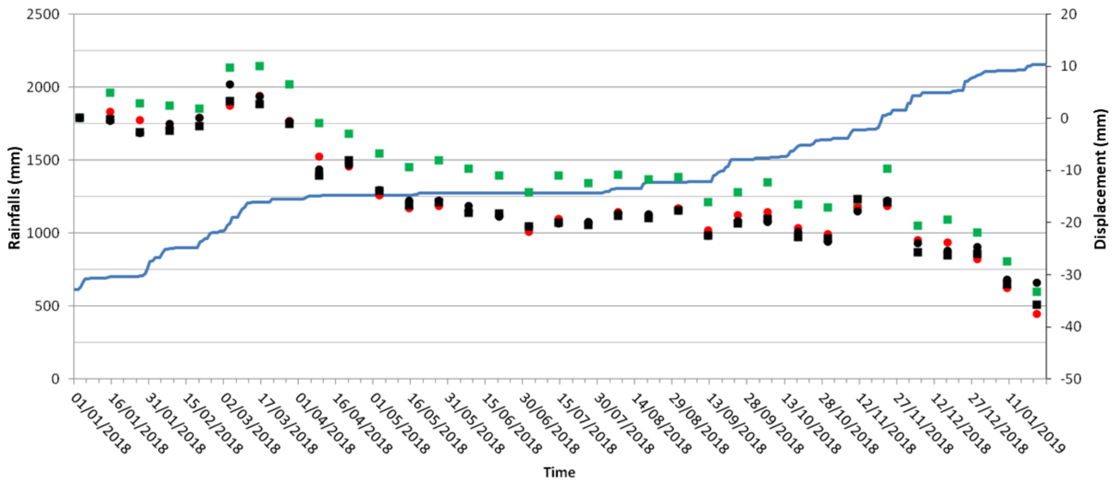

(c)

Figure 46: Comparison Between: (a) InSAR Data and Daily Rainfall, (b) InSAR and Monthly Rainfall, and (c) InSAR and Cumulative Rainfall for Points Located at Toe of Dam I

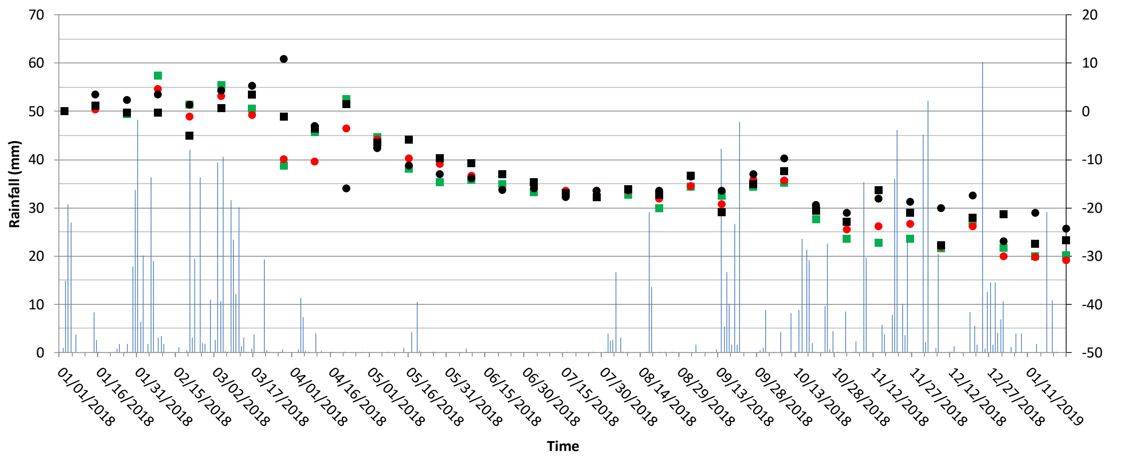

(a)

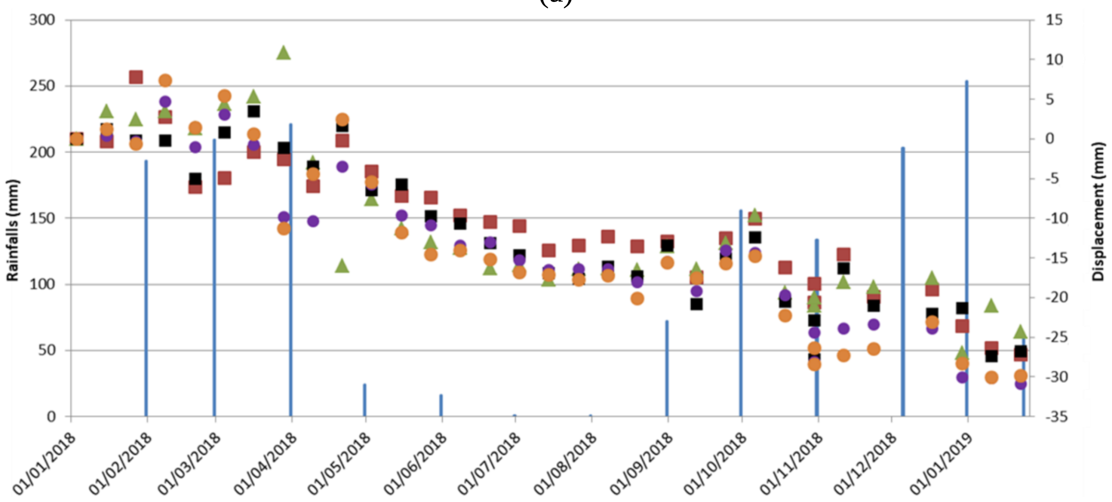

(b)

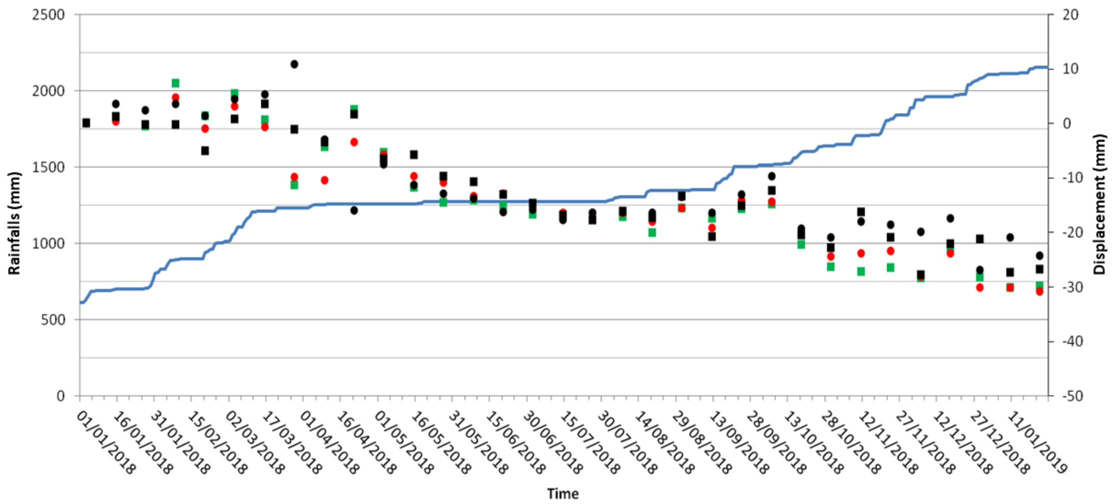

(c)

Figure 47: Comparison Between: (a) InSAR Data and Daily Rainfalls, (b) InSAR and Monthly Rainfalls, and (c) InSAR and Cumulative Rainfall for Points Located at the Crest of Dam I

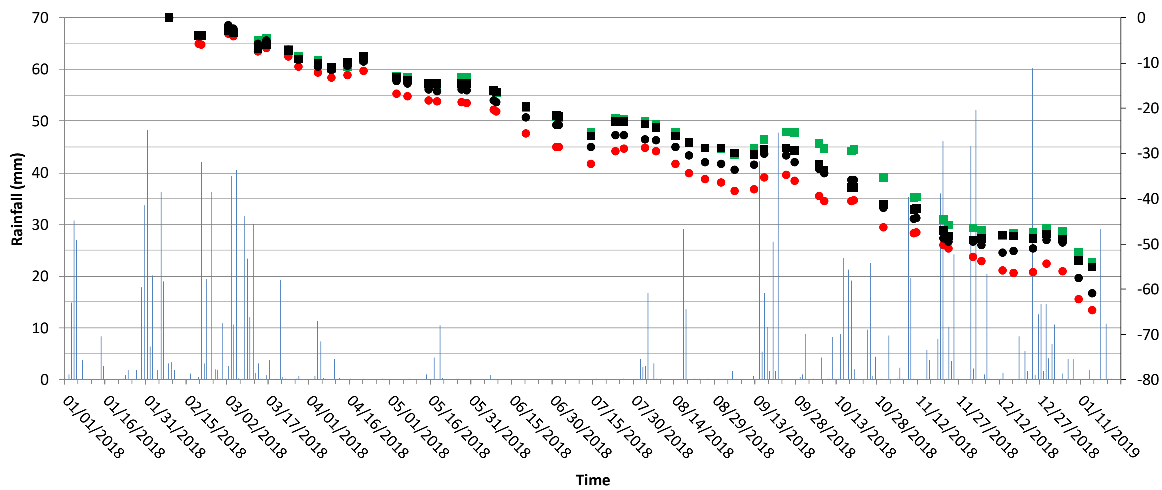

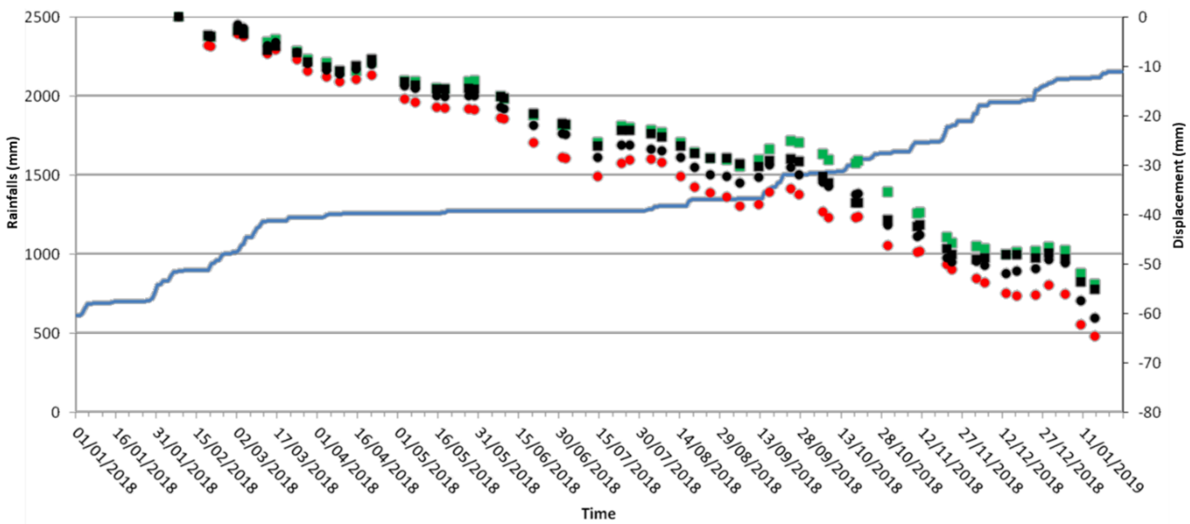

Figure 48: Comparison Between: (a) InSAR Data and Daily Rainfall, and (b) InSAR and Cumulative Rainfall for Points Located Within Tailings

7. SENTINEL-2 ANALYSIS

The objective of the Sentinel-2 analysis was to investigate the dynamics and changes of the Dam I surface during the entire year before the collapse. The focus of the analysis was the dynamics of:

- the pond and wet areas on the tailings; and
- the soils and the vegetation on the dam face, the tailings, and the surroundings for indirect analysis of moisture levels during time.

Multispectral Copernicus Sentinel-2 (S2) satellite images acquired from the European Space Agency (ESA) Sentinel Scientific Data Hub were used. The Sentinel-2 images are derived from two identical satellites (2A and 2B) placed in a sun-synchronous orbit. Sentinel-2 incorporates an innovative wide swath (290 km), high spatial (10 m to 60 m), and temporal (~5 day or ~10 day) resolution. The Sentinel-2 sensor operates on 13 spectral bands covering the visible, near infrared ("NIR") and shortwave infrared ("SWIR") electromagnetic frequency domains.

From the ESA Hub, 19 Sentinel-2 images were selected from January 2018 to January 2019. In Table 1, the image list with the acquisition date is shown.

Table 1: Sentinel-2A and Sentinel-2B data

No.	**Satellite**	**Date**	**N.**	**Satellite**	**Date**
1	S2B	January 22, 2018	**11**	S2B	August 20, 2018
2	S2B	March 13, 2018	**12**	S2A	September 9, 2018
3	S2A	April 27, 2018	**13**	S2B	September 24, 2018
4	S2B	May 2, 2018	**14**	S2A	October 14, 2018
5	S2B	May 22, 2018	**15**	S2B	January 18,.2018
6	S2A	June 1, 2018	**16**	S2A	December 23, 2018
7	S2B	June 16, 2018	**17**	S2B	January 7, 2019
8	S2A	July 6, 2018	**18**	S2B	January 17, 2019
9	S2B	July 21, 2018	**19**	S2A	January 22, 2019
10	S2A	August 15, 2018			

The datasets were pre-processed for atmospheric correction to obtain reflectance values. The following processing workflow consists of the selection of the bands with 10 m and 20 m resolution and of the resampling of all the data to a higher resolution. The analysis and interpretation were conducted on different colour composites and on three different calculated indices (Moisture Index, Normalized difference water index - NDWI, and Normalized Difference Vegetation Index - NDVI).

7.1 Pond Within Tailings and Wet Areas

The most useful composites were selected to highlight and follow the evolution of the pond and the wet areas within the tailings in Dam I, for which the Near Infrared - NIR and Short Wave Infrared - SWIR bands were used (RGB 8-4-3; RGB 12-8-3; RGB 8A-11-12).

7.1.1 Pond

- From January to June 2018: the pond was detected in all the images (Figure 49a-b), located almost in the same position near the stream inlet from the catchment above. The NDWI dated April 27, 2018, clearly confirms the presence of a water body in the central part of the wet area (Figure 51). In Figure 51, the pond is the blue feature (water has the maximum value) in the central part of the wet area (coloured in green for the lower value of wetness index).
- In July 2018, the pond completely disappears, as the tailings surface dries (Figure 49c).
- In August 2018, the pond is again detectable (Figure 49d).
- The image in late September 2018 shows an extension of the pond and the presence of a second pond on the south-eastern (SE) part of the dam (Figure 49e).
- In October 2018, both ponds visible during September 2018 disappear.
- On December 18, 2018, the two ponds are again visible, and the whole tailings surface is wetter compared to late September 2018 (Figure 49f). In the corresponding NDWI and Moisture Index, the central pond is less evident than in April 2018, but the negative values in NDVI indicate the presence of water.
- On January 7, 2019, the pond surface seems to have further increased from December 2018, as confirmed by the NDWI and Moisture Index elaboration. Conversely, in the following 10 days (January 17, 2019), the pond is strongly reduced, and both NDWI and Moisture Index confirm the decreased moisture levels in the area. By January 22, 2019, in all composite images, the situation seems stationary and one pond near the stream inlet remains visible, as confirmed by the NDWI and Moisture Index elaborations (Figure 53).

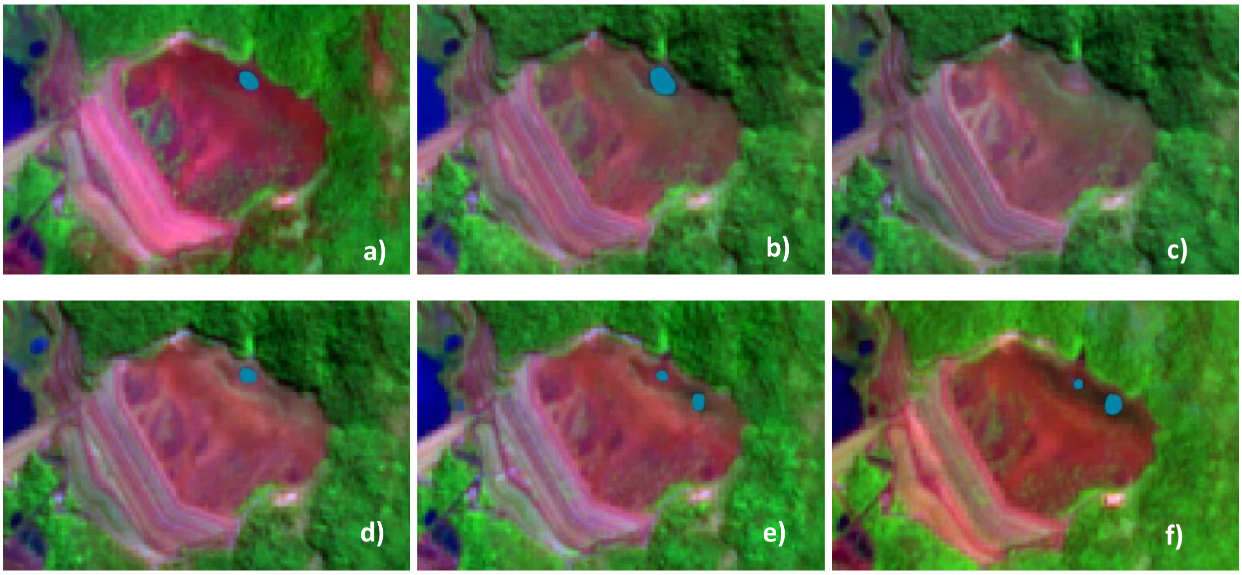

Figure 49: Dynamics of Pond (Depicted in Blue) on Dam I in S-2: (a) January 22, 2018, (b) June 1, 2018, (c) July 21, 2018, (d) August 15, 2018, (e) September 23, 2018, and (f) December 18, 2019

7.1.2 Wet Areas

A wet area was detected on the northern part of the tailings. The extent of the wet area has changed over the monitoring period, with the maximum in mid-March 2018 and then shrinking and remaining relatively constant in the following months (April to June 2018) (Figure 50a-b).

- In July 2018, the limits of the wet area on the tailings (Figure 50c) seem stable when compared to June 2018.
- August and September 2018 show an increase in the extent of the wet area on the tailings with respect to July 2018, but not to the extent seen in April to June 2018.
- In October 2018, a strong decrease in the extent of the wet area is observed, while December 2018 and January 2019 depict the wet area reaching almost its maximum spatial extension, especially on December 18, 2018, and January 7, 2019 (Figure 50d-e).

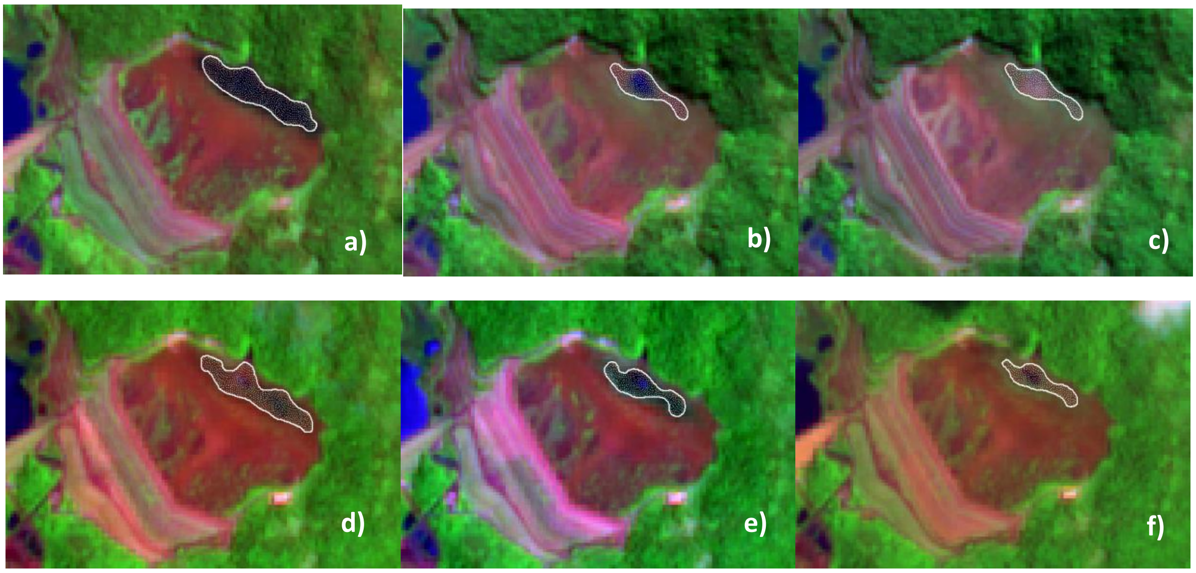

Figure 50: Dynamics of Wet Area (White Boundary) on Dam I in S-2: (a) March 13, 2018, (b) June 1, 2018, (c) July 21, 2018, (d) December 18, 2018, (e) January 7, 2019, and (f) January 22, 2019

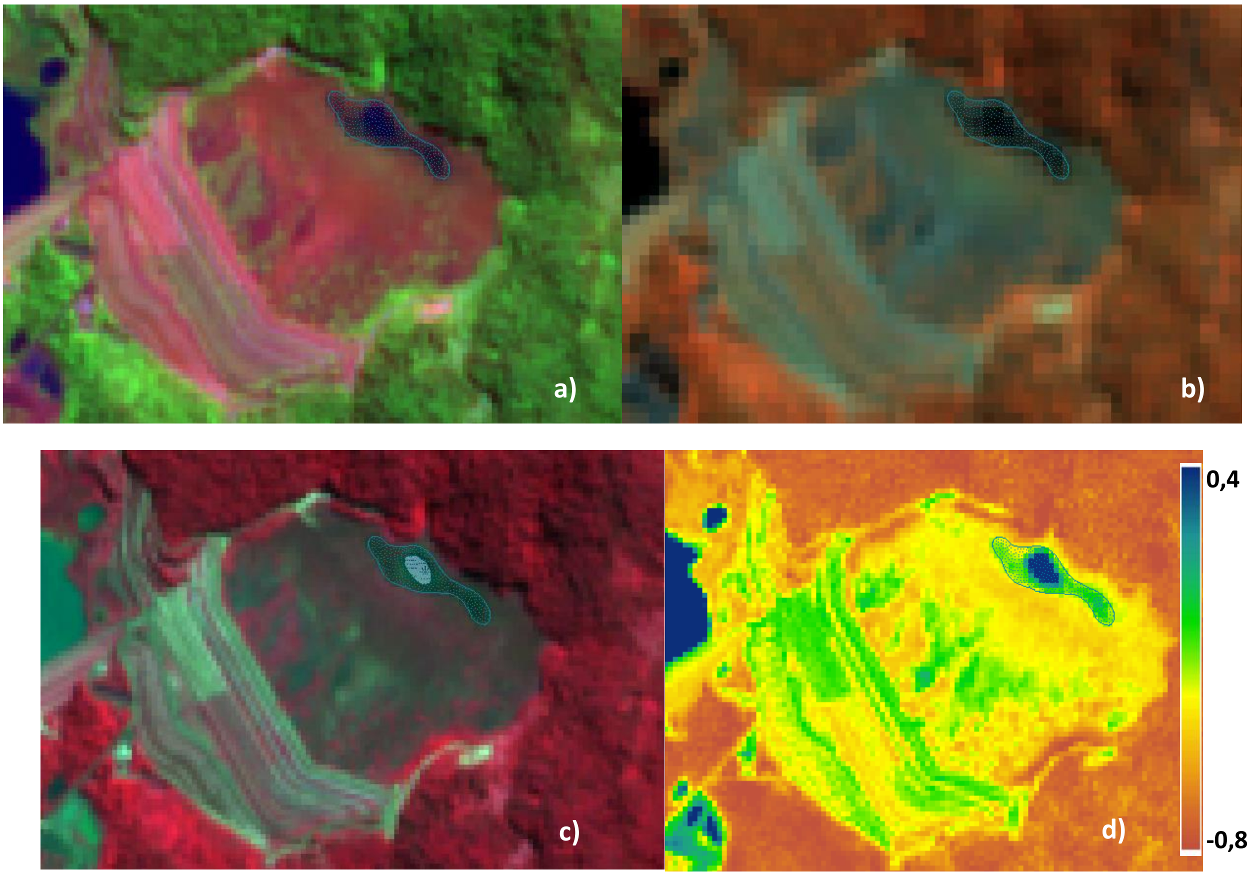

Figure 51: S-2 Data for April 27, 2018. Elaborations Used to Identify Wet Area and Pond Inside It. (a) RGB 12-8-3; (b) RGB 8a-11-12; (c) RGB 8-4-3; (d) NDWI Index

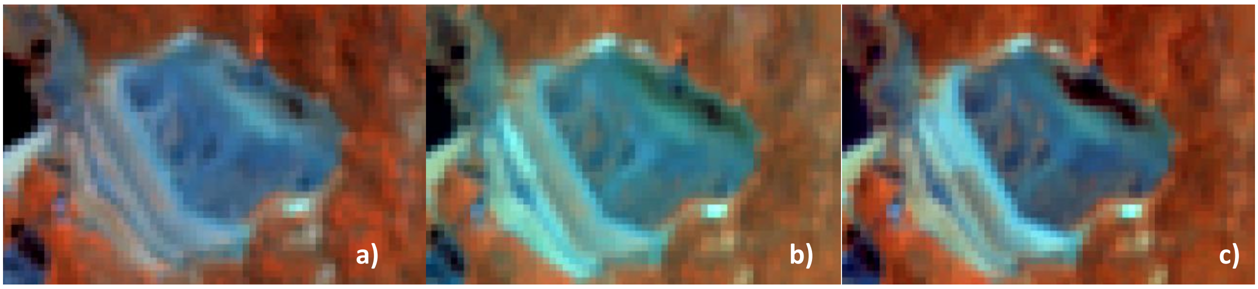

Figure 52: Comparison Between (a) September 24, 2018, (b) December 18, 2018, (c) and January 7, 2019, S-2 RGB 8a-11-12 Composites. It is Possible to Detect the Presence of the Second Pond in (a) September 24, 2018, (b) the presence of Two Distinct Ponds in December 18, 2018, and (c) the General Increase of Water Surface in January 7, 2019

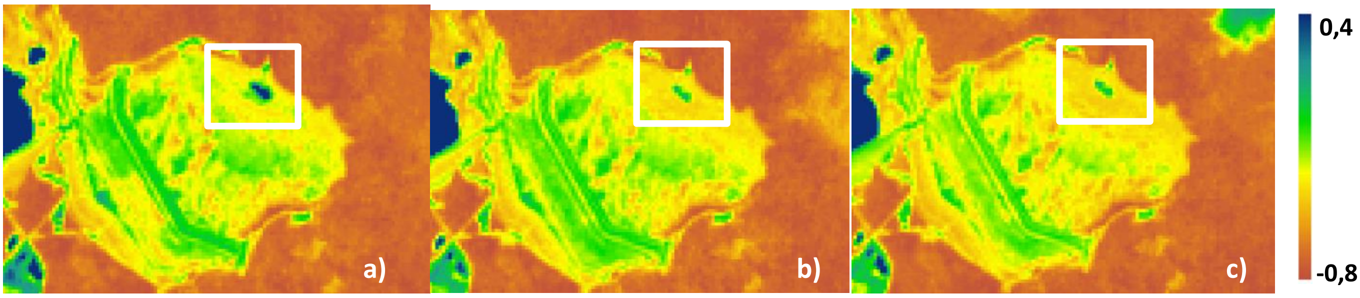

Figure 53: Comparison Between S-2 NDWI Elaborations That Show Progressive Decrease of Water Surface in Northern Part of Dam I for (a) January 7, 2019, (b) January 17, 2019, and (c) January 22, 2019

7.2 Setback Area

The NDWI elaboration and analysis highlight particularly high NDWI values in the setback area from December 2018 to January 2019, indicating high moisture levels in this sector of the dam during this period. In particular:

- December 18, 2018: The NDWI image (Figure 54) shows the mid-south area with higher values of moisture with respect to the surroundings and with respect to the previous months. Although, the Moisture Index of the same date is unable to show this relative difference (possibly due to the type of soil composition), the NDVI confirms the absence of vegetation. This indicates that the higher moisture values are not connected with vegetation presence, but most likely with presence of wet soil.
- January 7, 2019: Similar high NDWI values as per the image of December 18, 2018.
- January 17, 2019: The NDWI image shows lower values in this area than those shown in the previous image acquisitions in December 2018 and January 2019.
- January 22, 2019: The NDWI image shows low values similar to the image acquisition on January 17, 2019 (Figure 53).

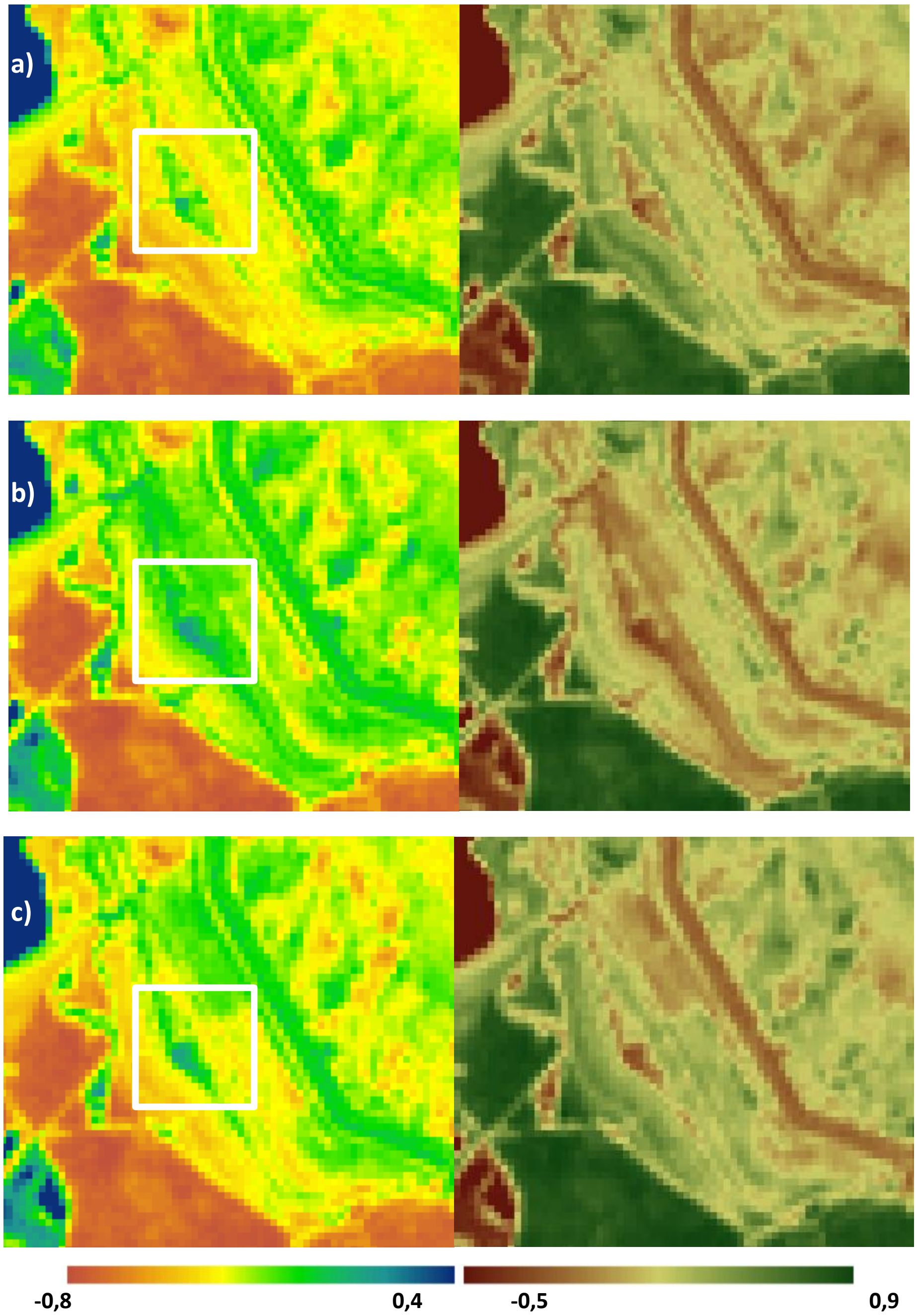

Figure 54: Comparison Between S-2 NDWI and NDVI Elaborations Showing Moisture Content in Setback Area of Dam from December 2018 to early January 2019 With Respect to Values of October 2018: (a) October 14, 2019, (b) December 18, 2019; and (c) January 7, 2019

7.3 Vegetation Differences in the Tailings and on the Dam Front

The Sentinel-2 multispectral data also provided information on the dynamics of the vegetation on the face of Dam I. In particular, the analysis of the Sentinel-2 data on the vegetation coverage can be summarized as follows:

- In January 2018, the dam face is not vegetated or has limited vegetation coverage, although the surface of the tailings has some vegetated area, mainly grass.

- In March 2018, the dam face and tailings show high signal responses associated with vegetation presence.
- In April 2018, the dam face vegetation seems to have been cut (straight line between vegetated (southern part) and not vegetated (northern part) areas). In the tailings, the vegetation response is similar to the March 2018 image. The NDWI index highlights two distinct zones with relevant differences in moisture (probably due to vegetation) (Figure 51).
- In May 2018, the dam face and tailings vegetation have the same distribution as in April 2018.
- In June 2018, the dam face vegetation seems to have been cut and regrowth is visible. The vegetation on the tailings did not change with respect to May 2018.
- In July 2018, over the entire area there is a weaker vegetation response, and the tailings close to the dam crest are much drier than in the previous months. These conditions are likely the result of low precipitation.
- In August 2018, there is very low vegetation, and the tailings close to the dam crest are much drier than in July 2018 (despite the presence of the pond).
- In September 2018, there are no changes in the vegetation response on the dam face in comparison with August 2018. Vegetation regrowth is visible on the tailings.
- In October 2018, the dam face and the tailings have a very high vegetation response.
- On December 18, 2018, the lower part of the dam face is not vegetated, the grass having apparently been cut. The tailings are showing vegetation similar to that of October 2018. The NDWI shows a second area with higher moisture values on the dam face. The NDVI confirms the absence of vegetation. The Moisture Index is unable to show this relative difference, possibly due to high levels of soil moisture. The December 22, 2018, image shows an evident change in the dam face: the vegetation of the northern part was completely cut (straight line).
- On January 7, 2019, much more vegetation is observed on the tailings. The northern part of the dam face is still not vegetated. On January 17, 2019, it seems that the situation has inverted: the northern part is showing vegetation regrowth while the southern part is completely cut (Figure 55). Similarly, on January 22, 2019, the southern part shows some evidence of vegetation regrowth, confirmed by the NDVI. The Moisture Index shows a gradual increase in dryness on the dam face and tailings, due to the lack of January rainfall. The NDVI image shows limited vegetation regrowth on the dam face.

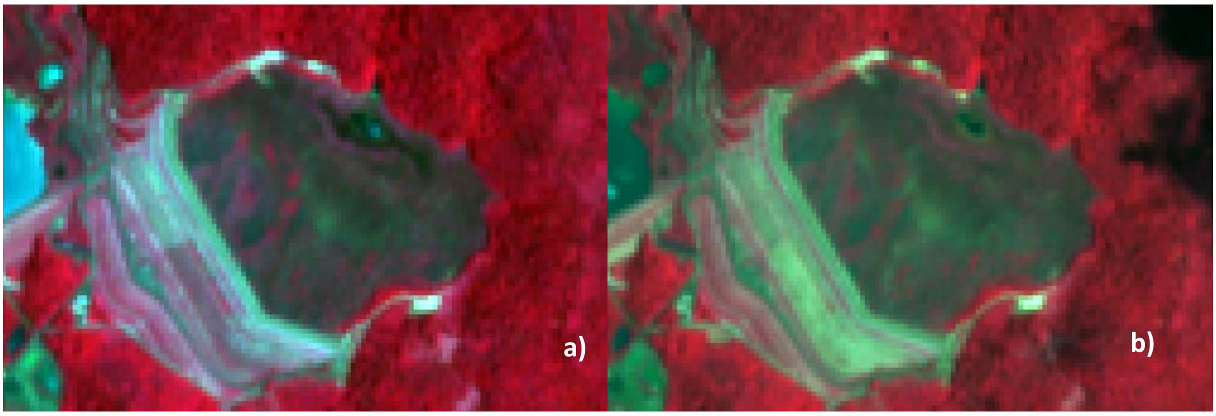

Figure 55: Comparison Between the S-2 Acquisitions on (a) January 7, 2019, and (b) after 10 days (January 17, 2019). Note the Shrinking of the Wet Area in the Northern Part of Dam I

8. VHR OPTICAL SATELLITE IMAGE ANALYSIS

The aim of the Very High Resolution (VHR) Optical Satellite Image analysis, together with the Sentinel-2 results in Section 7, was to investigate the dynamics and changes of the dam's surface during the year before the failure.

Images were collected by the following commercial satellites:

- The GeoEye-1 satellite, by Digital Globe. The sensor operates on four bands from visible to near infrared and simultaneously on the panchromatic band. The resolution is 1.65 m for the multispectral imagery and 0.41 m for the panchromatic imagery.
- WorldView-3 (WV-3), by Digital Globe, is the first multi-payload, super-spectral, high-resolution commercial satellite sensor. The WV-3 sensors collect the standard panchromatic and multispectral bands, eight-band SWIR, and 12 CAVIS imageries. The WorldView-3 satellite provides 0.31 m in panchromatic resolution, 1.24 m multispectral resolution, 3.7 m SWIR, and 30 m CAVIS resolution.
- The Pléiades constellation by Airbus Defense & Space. Pleiades 1A and 1B are identical for their specifications, with image acquisition of 0.5 m in panchromatic mode and 2 m in multispectral mode (blue, green, red, and NIR).

The four satellite bundle images (panchromatic and multispectral dataset) analyzed were acquired on the following dates:

- June 2, 2018, WV-3, 8 multispectral bands; 1 panchromatic band;
- July 21, 2018, WV-3, 8 multispectral bands; 1 panchromatic band;
- September 23, 2018, GE-1, 4 multispectral bands; 1 panchromatic band; and
- January 18, 2019, Pleaides, 4 multispectral bands; 1 panchromatic band.

Multispectral data were analyzed by different processing, including radiometric correction and conversion to top-of-atmosphere (“TOA”) spectral radiance, co-registration and sub-setting of all the multispectral and panchromatic images, setup of different colour composites and decorrelation stretching process, and calculation of two indices (NDWI and NDVI).

The VHR data, which cover the period from June 2018 to January 2019, confirm all the observations made with Sentinel-2, providing a higher resolution in the definition of objects and features.

All optical satellite data were compared to the time series of rainfall data, to support their interpretation.

8.1 Pond Inside the Tailings and Wet Areas

The pond inside the tailings and the wet area were analyzed and mapped. Compared with the Sentinel-2 images, all the features previously observed were confirmed.

8.1.1 Pond

- In the June 2018 WV-3 acquisition (June 2, 2018) the pond (depicted in blue in the right column of Figure 56) has the same extension as projected in the Sentinel-2 data from the same period (June 1, 2018). The position and size of the water surface is confirmed by NDWI and NDVI indices.
- In the July 2018 WV3 acquisition (July 22, 2018), the pond completely disappears similar to the Sentinel-2 data (July 21, 2018). Due to the absence of surface water, the pond sediments are clearly visible (high reflectivity in all bands) (depicted in light brown in Figure 56b, right column).
- In the September 2018 GE-1 acquisition (September 23, 2018), the pond, as observed in Sentinel-2 data, is again visible and confirmed by NDWI and NDVI indices. A second pond is detected on the SE part of the wet area (depicted in blue in Figure 56c, right column). The increased resolution, in particular the panchromatic mode with 0.5 m, provided additional details for the surroundings of the pond area (Figure 57). An interesting feature is the possible damming of the main Dam I inlet by an earth berm first visible in September 2018 (Figure 57b).
- In the January 2019 Pleaides acquisition (January 18, 2019), the central pond is present and wider than in the September 2018 VHR image (Figure 56d). The second pond on the SE part of the wet area is not visible anymore. The damming is still present and complete in January 2019, probably causing water concentration upstream, confirmed by the NWVI index (Figure 57d).

8.1.2 Wet Area

- In the June 2018 WV-3 acquisition (June 2, 2018), the wet area (white boundary in Figure 56a, right column) has the same extension projected in the Sentinel-2 data from the same period (June 1, 2018). The size of the wet area also is confirmed by NDWI and NDVI indices.
- In the July 2018 WV3 acquisition (July 22, 2018), the boundary of the wet area (white boundary in Figure 56b) is the same as the previous month and as the Sentinel-2 data from the same period (July 21, 2018).
- In the September 2018 GE-1 acquisition (September 23, 2018), the wet area has a wider extension than that from July 2018, but similar to the Sentinel-2 data (September 24, 2018). The size of the wet area is confirmed by NDWI and NDVI GE-1 indices.

- In the January 2019 Pleaides acquisition (January 18, 2019), the wet area has the same extension as the Sentinel-2 data (January 17, 2019).

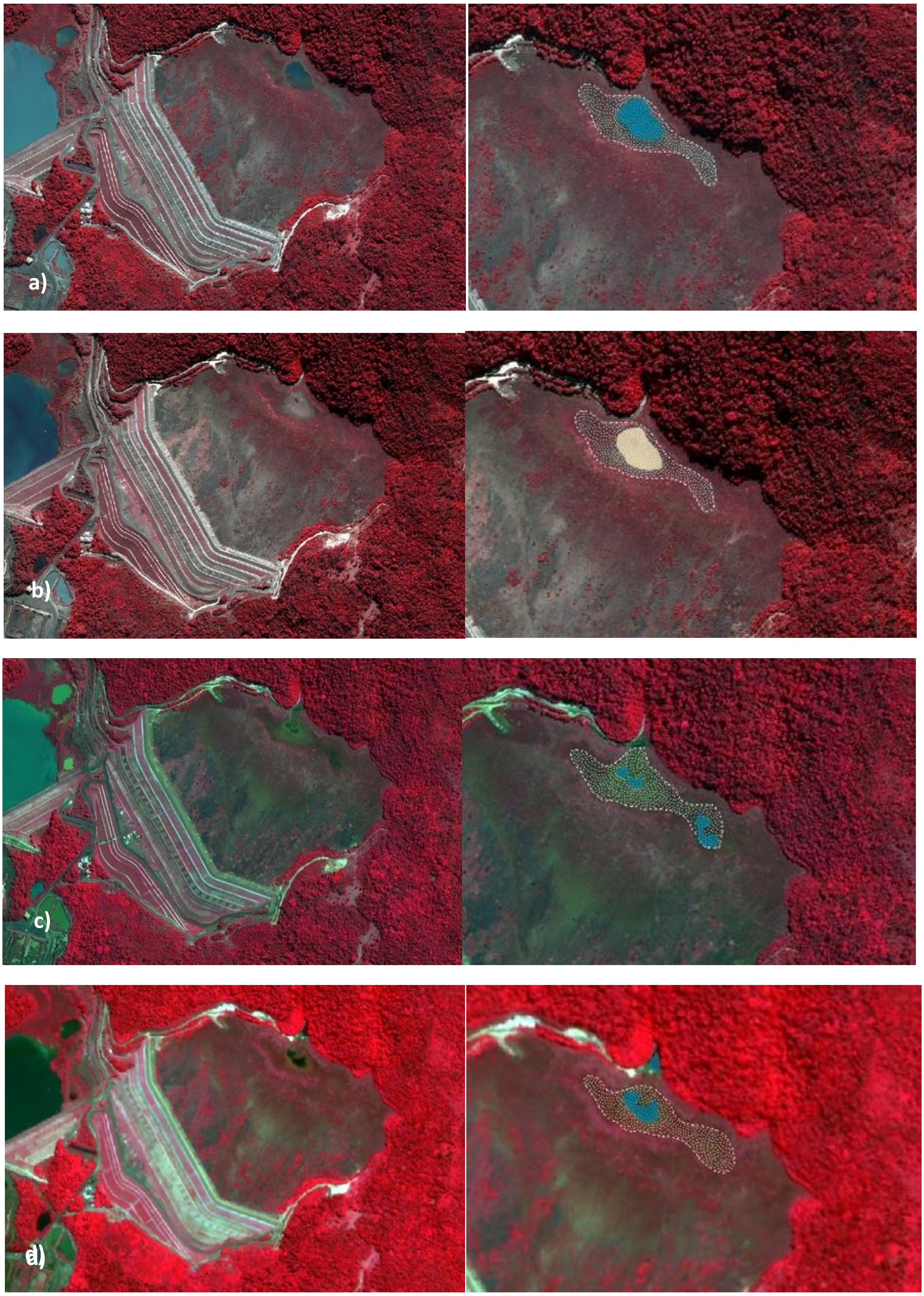

Figure 56: Left column: Dynamic of the Pond and Wet Area from June 2018 to January 2019: (a) June 2, 2018, WV3 RGB 654; (b) July 22, 2018, WV3 654; (c) September 23, 2018, GE-1 RGB

432; (d) January 18, 2019, Pleiades RGB 432. Right column: Detail of Wet Area (White Line) and Pond (Blue Polygon)

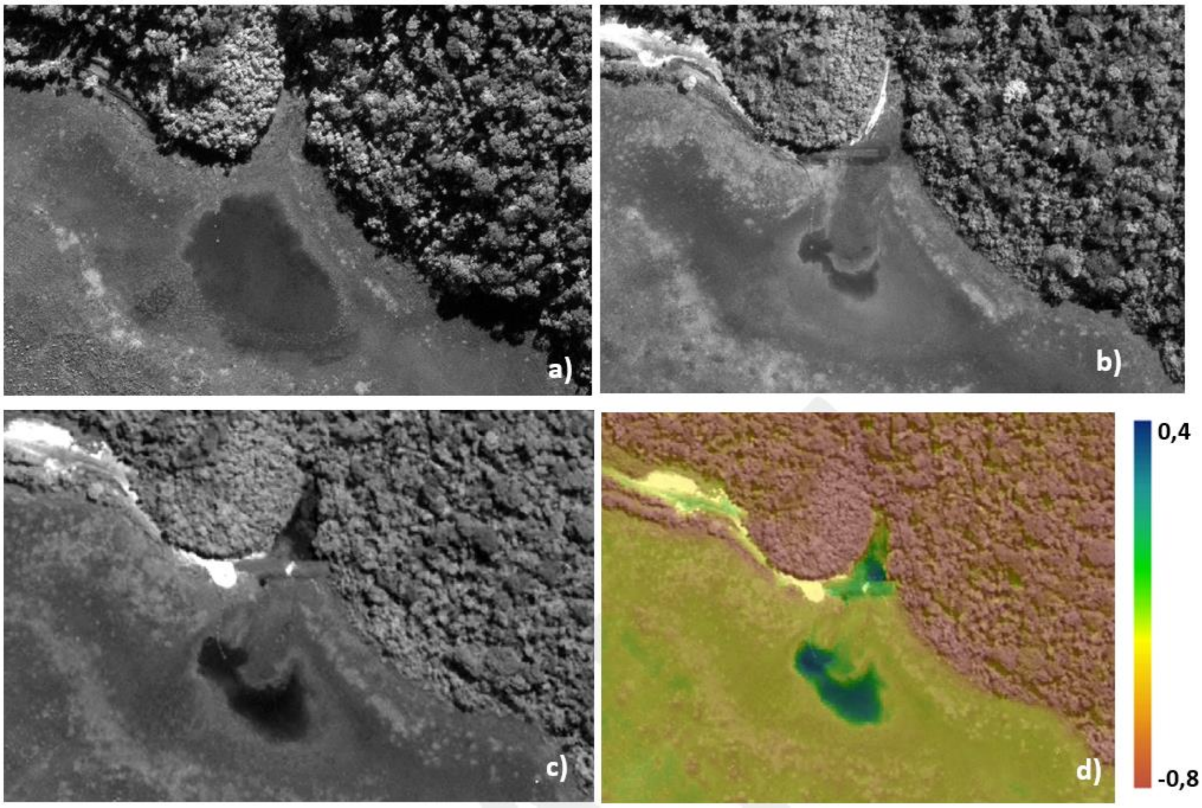

Figure 57: Possible Damming of Main Dam I Inlet by an Earth Berm. (a) Area in June 2018; (b) Starting of Inlet Damming in September 2018; (c) Dam is Complete in January 2019; and (d) Water Concentrates Upstream, Confirmed by NWVI Index

8.2 Vegetation Differences on Dam Face and Tailings

The vegetation analysis on the dam face and the tailings was conducted mainly through NDVI, NDWI, and decorrelation stretching of all colour composites.

Two different vegetation patterns are observed on the dam face. The lower part of the dam face shows grass and vegetation that is homogeneous and stable (Figure 58). The NDVI index and the colour composite only differs in the July 2018 acquisition (Figure 58b).

The upper part of the dam front is not homogeneously vegetated and is mostly bare (yellow to light brown in NDVI) with only small patches of grass (light green in NDVI) more visible in June 2018 and September 2018 (Figure 58a-c). In January 2019 (Figure 58d), this area of the dam face was characterized by two different zones: the northern zone is sparsely vegetated, and the southern zone is almost completely bare (vegetation cut). The same situation is shown in the Sentinel-2 image for January 17, 2019.

By comparing the four VHR dates, it is possible to identify three different zones in the tailings near the dam crest (Figure 59): the first (“1” in Figure 59a) is characterized by sparse and stable vegetation in the shape of an upside down “Y”; the second area (“2” in Figure 59a) is less vegetated and characterized by very dark tailings, probably connected with a level of NDWI-related moisture; the third area ("3" in Figure 59a), on the SE part, seems dry and bright. These three areas remain stable over time, except in July 2018 when they undergo changes due to drier conditions (Figure 59b-d).

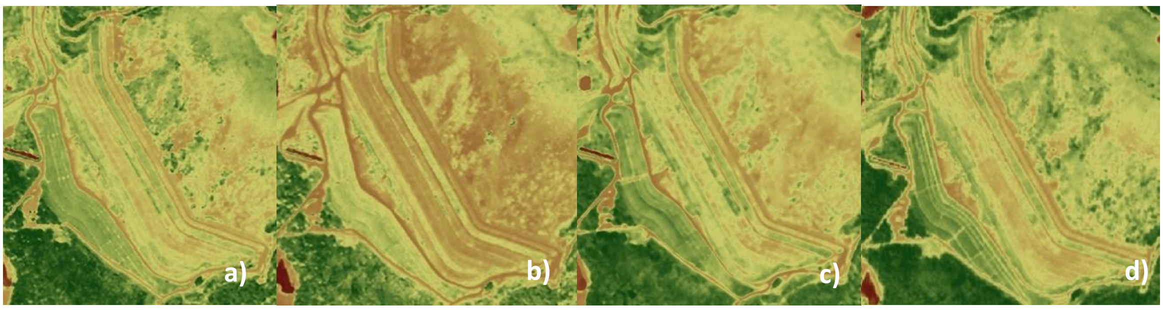

Figure 58: Comparison Among NDVI Indices From June 2018 to January 2019: (a) June 2, 2019; (b) July 22, 2018; (c) September 23, 2018; (d) January 18, 2019

In particular, in June 2018, area "1" is characterized by the presence of vegetation; surrounding area "2" has less vegetation and dark soils; and area "3" can be distinguished by bright and dry soils. In July, all the area has evident changes: the vegetation in area "1" disappears, as confirmed by NDVI indices (Figure 59d); area "2" with dark soil appears also dryer and less vegetated; and area "3" appears brighter and less vegetated.

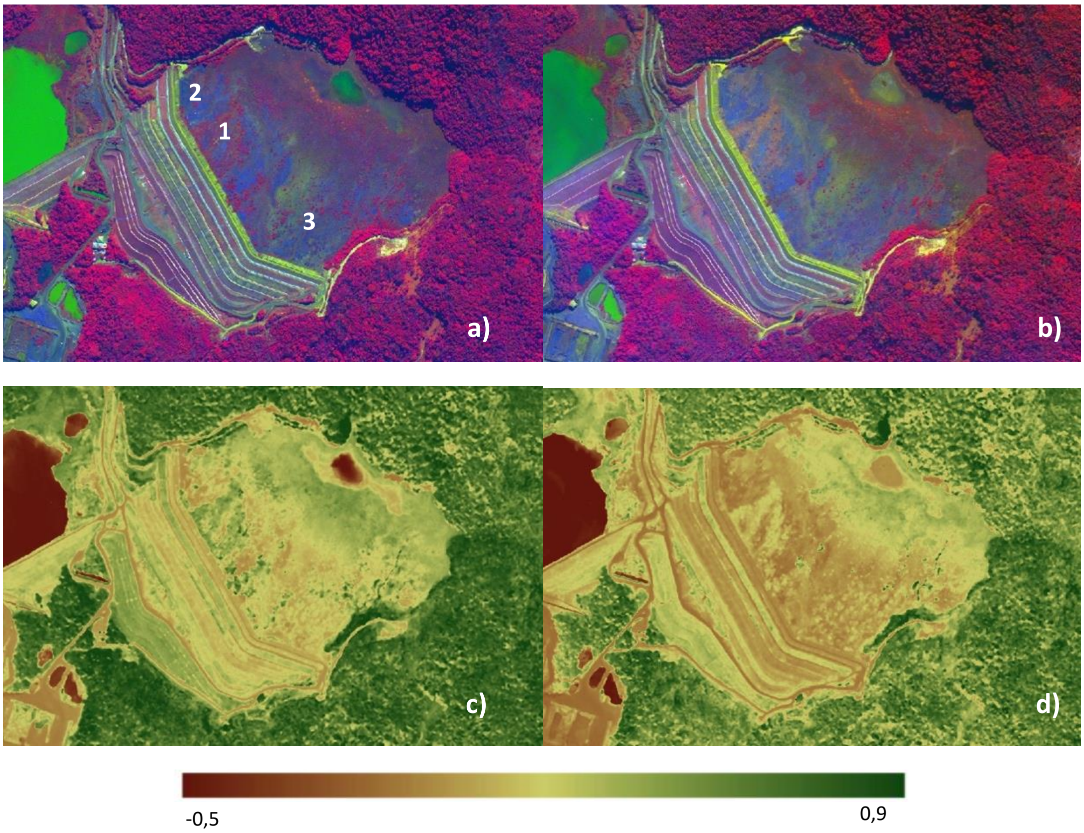

Figure 59: Comparison Between Main Seasonal Conditions: (Left) WV-3 Image of June 2018 (DS 641 and NDVI) and (Right) WV-3 Image of July 2018 (DS 641 and NDVI)

With respect to the 10 m Sentinel-2 images, the higher resolution of these multispectral data (from 1.2 m to 2 m) supported by the panchromatic band (0.3 m to 0.5 m), allows some details on the dam face to be seen that were not visible before or could only be assumed.

In particular, in the June 2, 2018, WV-3 image, in the central flat part of the dam face, it is possible to see an area with a different spectral response compared to the surroundings. The higher value of the NDWI (probable moisture anomaly) compared to the surroundings, and the high absorption in False Color Composite (FCC) and in pan image (black pixels), are probably related to the presence of water (Figure 60).

Figure 60: WV-3 of June 2, 2018. Left to Right: False Colour Composite RGB 654, Pan, and NDWI

On July 22, 2018, an area with different spectral response persists with the same higher NDWI value in comparison with the surroundings.

In the September 23, 2018, image, the anomaly highlighted in June and July 2018 is masked by anthropogenic factors. There are barracks and working facilities in the area. It is possible to observe a new drainage channel construction (Figure 61c).

In the January 18, 2019, image, the anomaly and the working facilities are no longer present (Figure 61d).

8.3 Anthropic Activity/Changes

The VHR image analysis allowed observations of specific changes on the dam and the tailings, including:

- the presence of a probable moisture anomaly on the central flat part of the dam front, observable from June to July 2018 (Figure 60 and Figure 61a-b); in July 2018, it seems that the construction of a supplementary channel began (Figure 61b);
- man-made modifications to the same area in the September 2018 image, including drainage channel construction with support facilities (Figure 61c); in January 2019 this channel is not present (reverse situation to June 2018) nor are the facilities and barracks (Figure 61d);
- other man-made modifications mainly concerning the dam front drainage system occurring from September 2018 to January 2019 (Figure 62); from the pan image comparison it seems that the channel drainage system has been modified in the area. The lower channel in the red circle, visible in September 2018, has been removed in January 2019, and on the right side a new channel is present (F1). On the left of the red circle, it seems that there are new works on the left channel (F2). F3 indicates that the horizontal channel is not clearly visible due to a possible surface modification or to the lower resolution of the Pleaides image with respect to Geoeye-1 (0.4 m to 0.5 m); and
- possible damming of the main Dam I inlet by an earth berm starting in September 2018. This damming is still present in January 2019 and probably causes water concentration upstream (Figure 57).

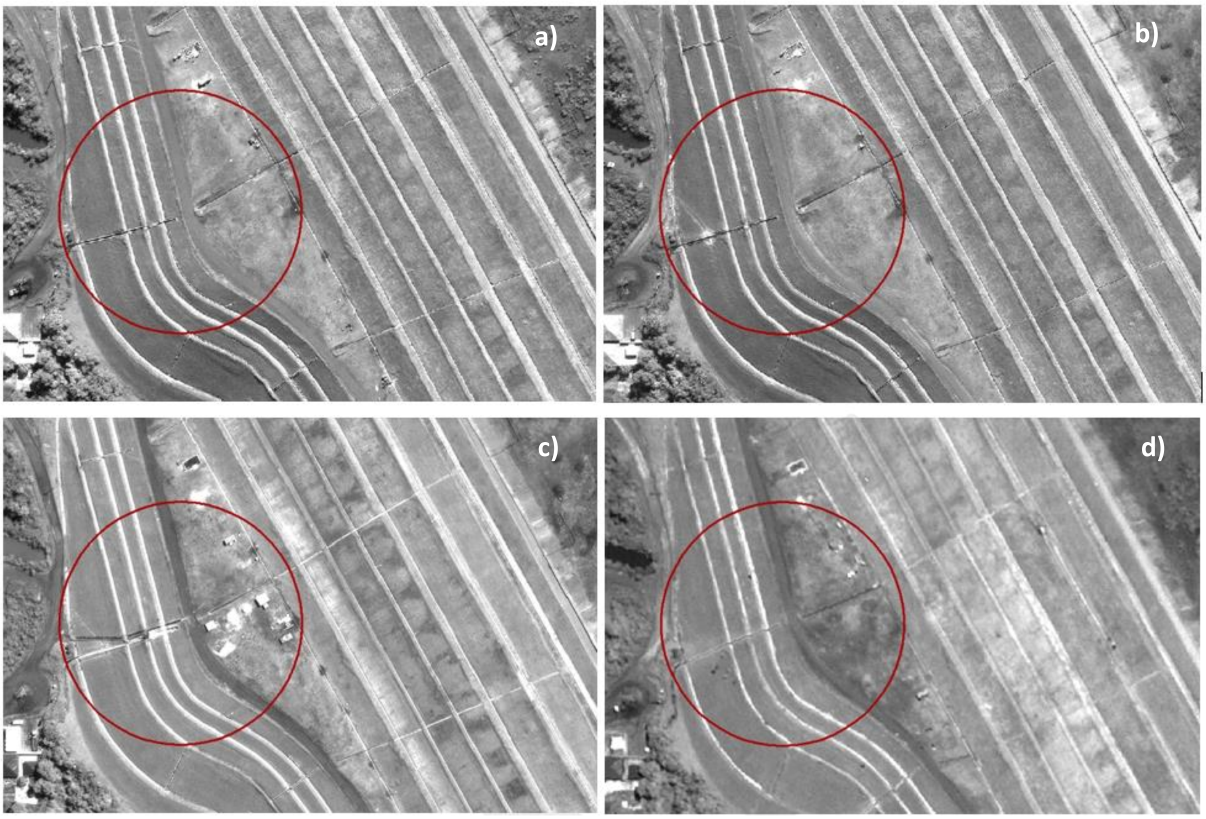

Figure 61: Pan Images of All Four VHR Dates: (a) June 2, 2018, (b) July 22, 2018, (c) September 23, 2018, and (d) July 18, 2019

Figure 62: Comparison Between GE-1 and Pleaides Pan Images of September 23, 2018, and January 18, 2019

8.4 Correlation With Rainfall Data

The daily rainfall data from 2018 to January 2019 collected from the F18 rain gauge as recorded in Appendix C were compared to the Sentinel-2 and VHR data.

From January to the end of June 2018 (Figure 63), most of the rainfall is concentrated in the first 3 months of the year. The high moisture level highlighted by the March 13, 2018, Sentinel-2 image is probably the consequence of this rainy period. Despite the progressive decrease in rainfall from

April to June 2018, all the images show a stable situation concerning the presence of the pond on the tailings.

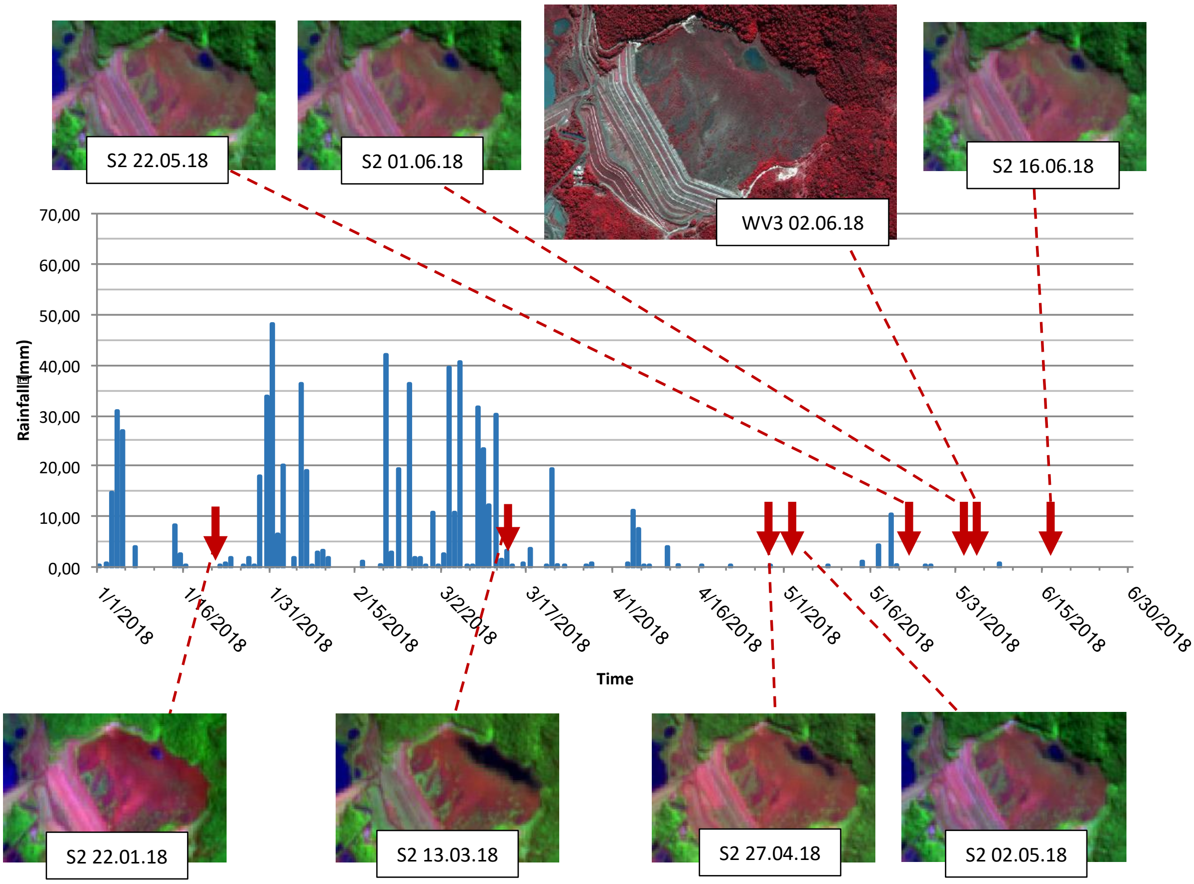

Figure 63: Rainfall Daily Data (Blue Bars) From January 1, 2018, to June 30, 2018. Time Position of Satellite Images is Shown by Red Arrows

From July 2018 to the end of September 2018 (Figure 64), the rainfall is concentrated after the middle of September. All the images for July 2018 confirm the dry period, with the absence of the pond and generally dry conditions of the dam (tailings, soils, and vegetation). In August 2018, despite the lack of intense rainfall, the pond is present in the Sentinel-2 image. The consequence of the rainfall in the middle of September 2018 is probably shown in the images by the presence of two ponds on the tailings.

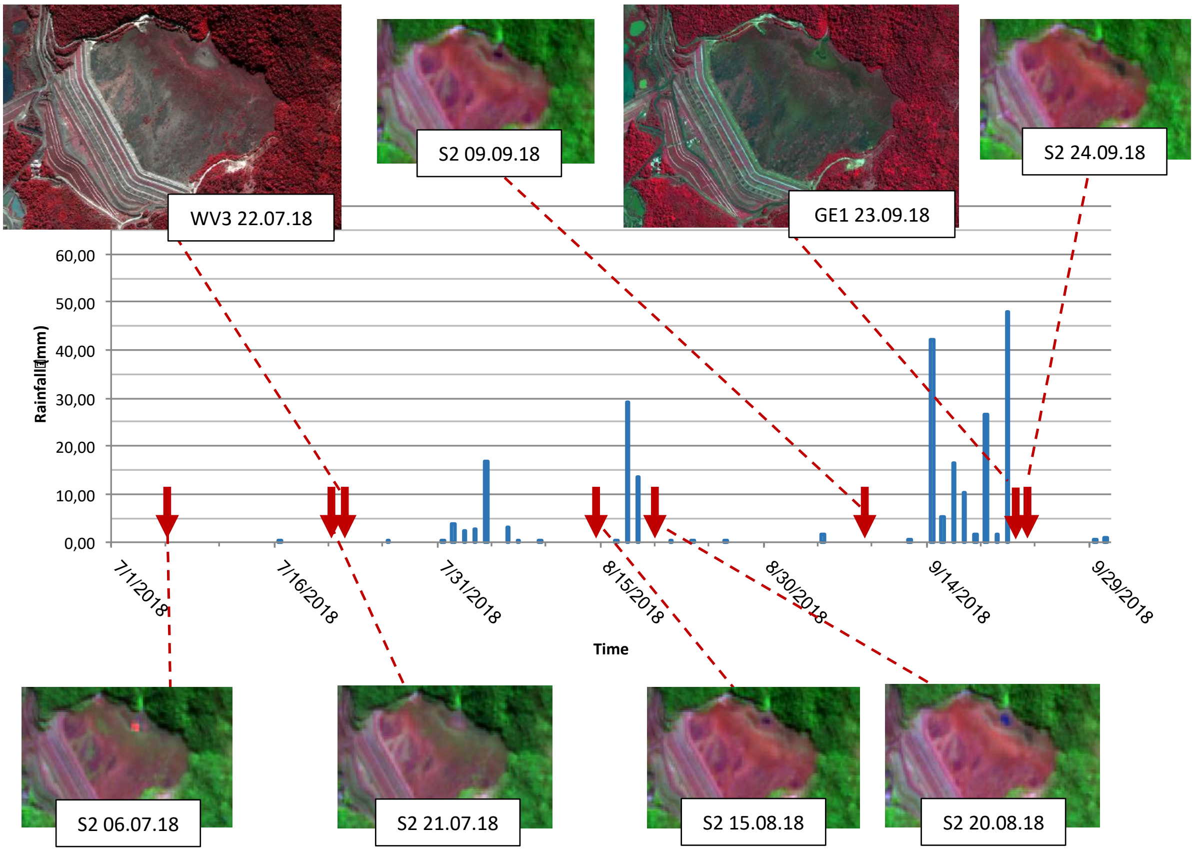

Figure 64: Rainfall Daily Data (Blue Bars) from July 1, 2018, to September 30, 2018. The Time Position of the Satellite Images is Shown by Red Arrows

The period from October 2018 to early January 2019 (Figure 65) is characterized by a more homogenous rainfall pattern. But, despite this, the October 14, 2018, image does not show the ponds of late September (GE-1 September 23, 2018, and S-2 September 24, 2018). The pond on the tailings is again visible in December 2018.

The extent of the pond is at a maximum in the January 7, 2019, S-2 image and decreases over the next two weeks (S-2 image of January 17, 2019), apparently due to the lack of rainfall. From the same images, it is possible to note the shrinking of the wet area. This dynamic is confirmed by the S-2 NDWI elaborations that show the progressive decrease of the water surface in the northern part of Dam I in January 2019 (Figure 53).

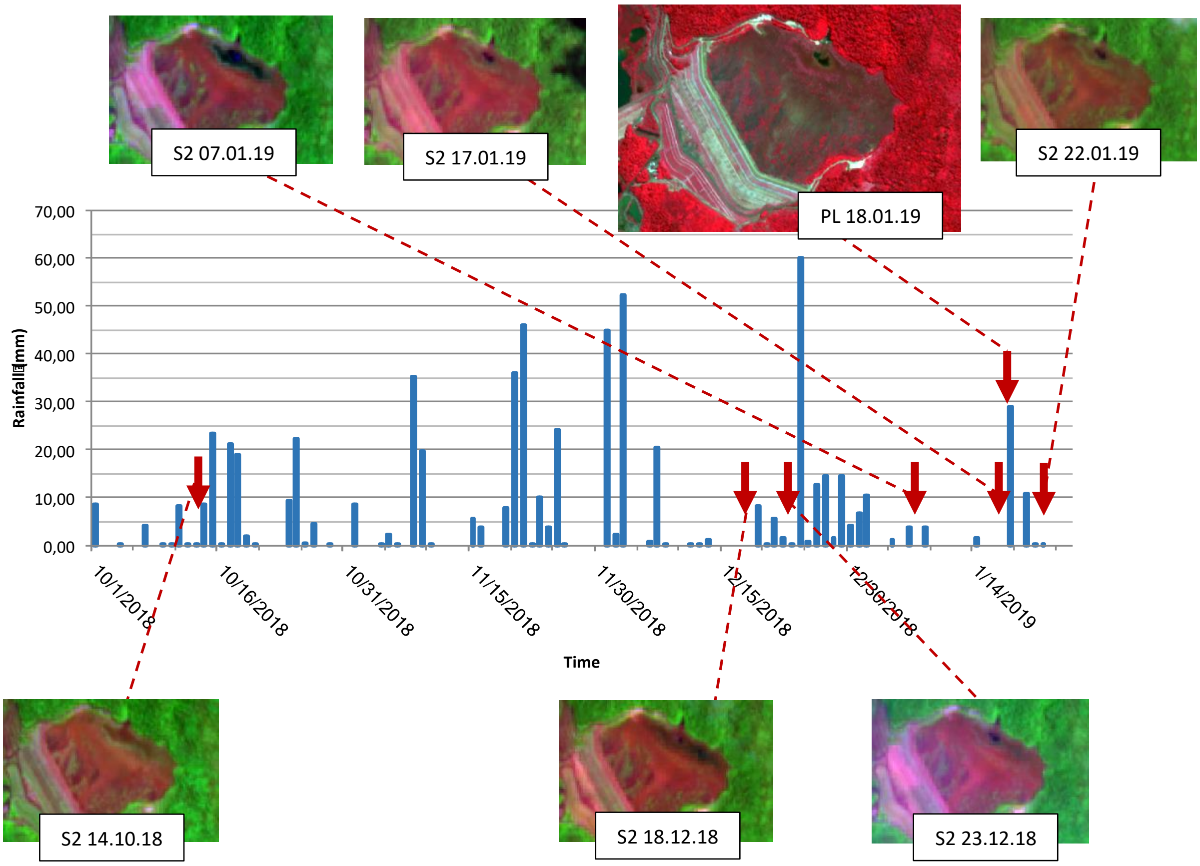

Figure 65: Rainfall Daily Data (Blue Bars) From October 1, 2018, to January 25, 2019. Time Position of Satellite Images is Shown by Red Arrows

9. VIDEO ANALYSIS

The main objective of this work was to model, analyze and interpret the video imaging data from the cameras trained on Dam I during the failure. The analysis was mainly based on the camera in front of the dam (Figure 68).

Since the camera was not connected to a global positioning system ("GPS") antenna, it was necessary to verify the difference between the camera time and UTC time. The camera time has been verified through the following procedure:

- On August 14, 2019, an on-line portal showing the live camera feed was viewed and compared to the camera's settings, as well as to a website showing coordinated universal time (UTC).
- A screenshot depicting both times (Figure 66) was taken.
- This procedure demonstrated a one second (s) delay between UTC (adjusted for the time difference) and the time stamp on the video. This also showed a 1 s difference between UTC time and the time reflected in the settings of the camera (Figure 67).

The above described procedure does not definitively confirm that the time of the camera on the day of the failure had the same time setting as was verified on August 14, 2019.

The video technical specifications are as follows:

- Duration: 15.30 s
- Bits per Pixel: 24, Frame Rate: 30 fps
- Height: 1080 pixels, Width: 1920 pixels
- Video format: RGB24, mp4

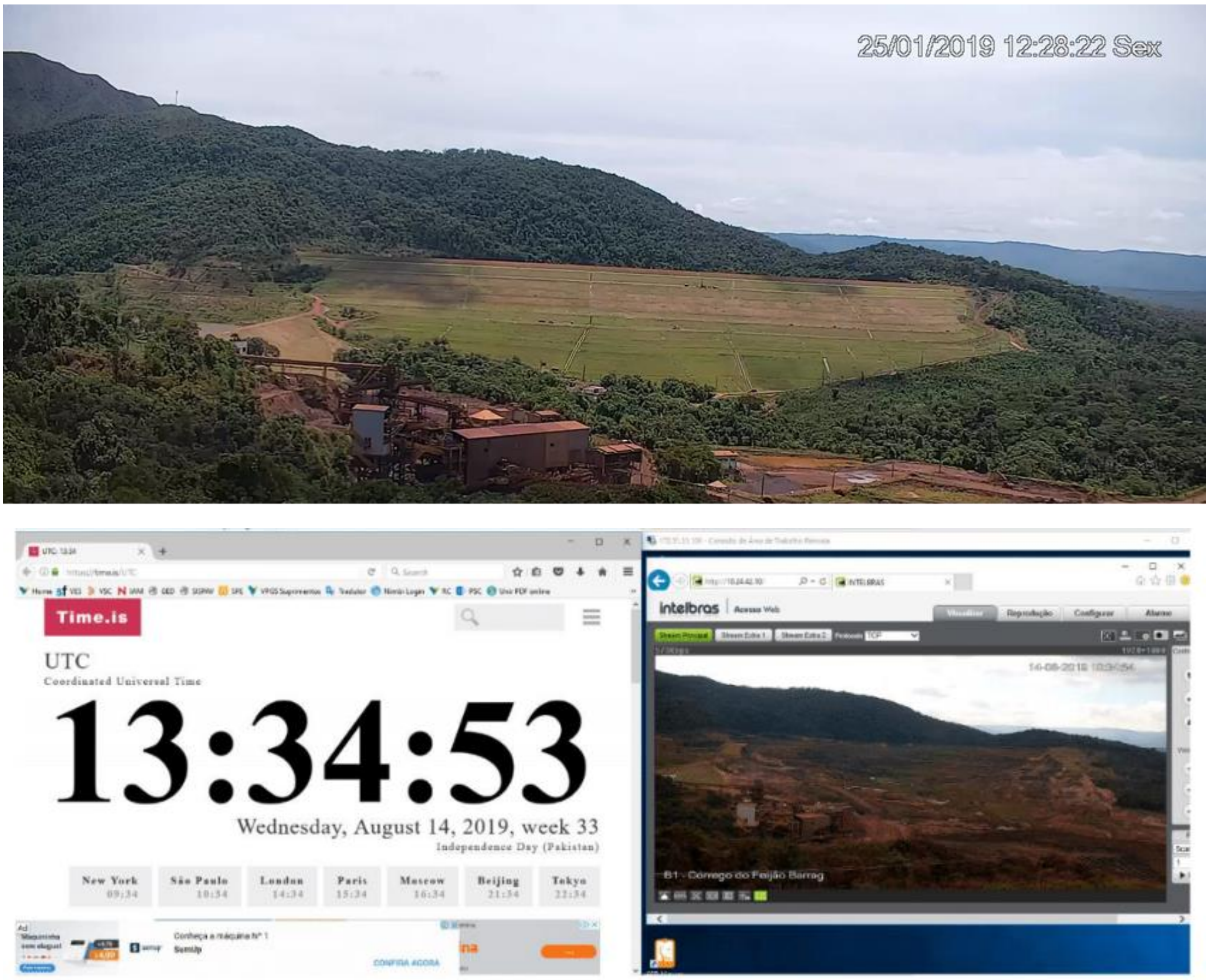

Figure 66: Screenshot Verifying the Time of the Camera With Respect to UTC

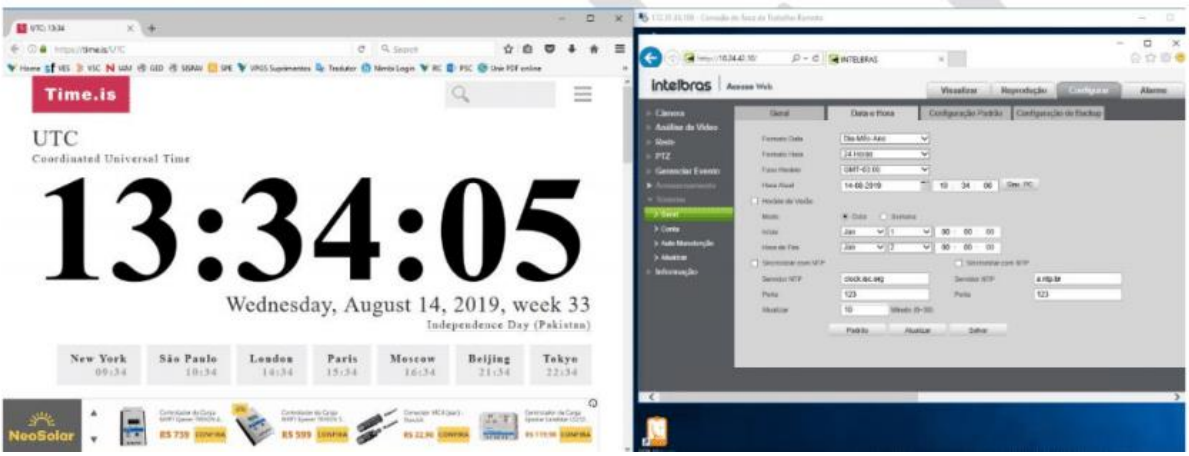

Figure 67: Screenshot Verifying Difference Between UTC and Time Reflected in Settings of Camera

Figure 68: Example of a Single Frame Extracted From Camera in Front of Dam I Prior to Failure

To calibrate the video images, a digital model of the topography of the dam and tailings was used (computer-aided design ("CAD") model from LiDAR data scans). The analysis ran from approximately 12:28:23.90 to 12:28:27.70 on January 25, 2019, covering ~4 s of the visible initiation of the failure. No pre- or post-failure images were included in the analysis to avoid decorrelation effects. Single frames were extracted from the video at a frequency of 30 fps (1/30 of a second between frames).

9.1 Methods

The video footage was analyzed first by applying a finite-element computational scheme capable of modeling the stress-strain continuum within the front of the dam during the initiation of the failure and its early stages. This was done to reveal possible initiation and failure mechanisms.

Digital image correlation ("DIC") modeling is the best tool to analyze deformation patterns from image sequences with indirect measurement of strain deformation in the horizontal direction ("*U*") and in the vertical direction ("*V*") (Figure 69). The strain deformation components *U* and *V* were analyzed separately during the modeling simulations.

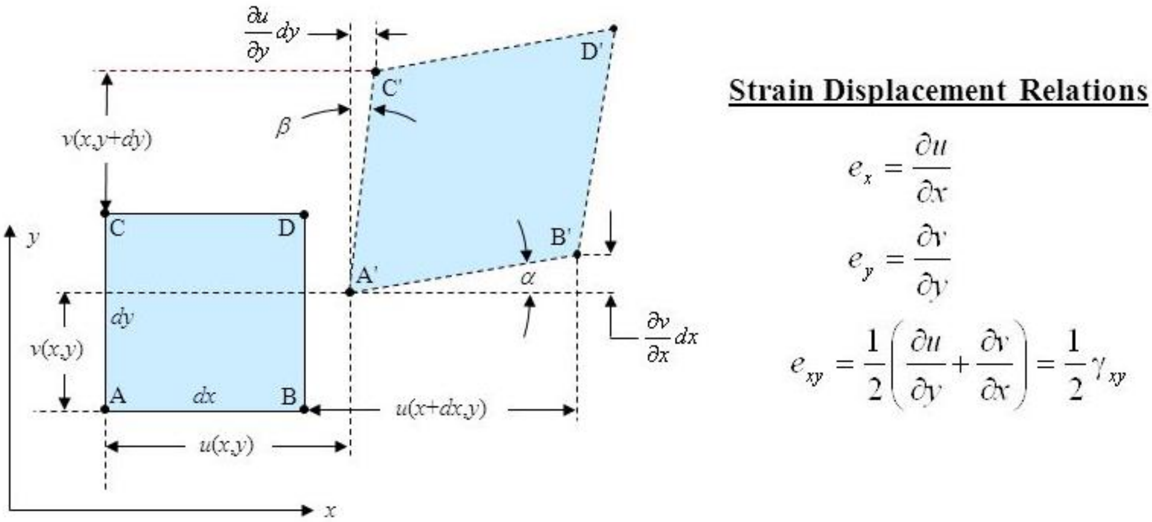

Figure 69: Sketch of Horizontal and Vertical Strain Deformation Components and Their Mathematical Formulation According to an Arbitrary Reference Origin

The procedure applied for the DIC analysis was:

- after preliminary video footage review, single frames were extracted and saved as speckle images for DIC analysis;
- a reference image was defined with fixed points;
- the reference image was calibrated to metric measurements using the available LiDAR topography dataset;
- a discrete element mesh ("DEM") was defined by an iterative procedure to optimize the size of the mesh element to reduce the noise;
- modeling parameters were adjusted during calibration;
- the model was run with strain deformation component dynamic modeling during failure;
- the output was a map showing the deformation frame by frame (not accumulated) along the two directions perpendicular to the camera line-of-sight;
- a set of tracking points was defined within the dam's front area with positioning driven by the DIC strain analysis;
- strain modeling analysis was run with point tracking for all points; and
- data files and plots with point tracking were generated.

The model specifications are a finite element mesh ("FEM") grid with calibrated reference points (based on DEM data) (Figure 70); a subset with Gaussian weighting and optimized 8-tap interpolation with zero-normalized squared differences; a consistency threshold of 0.20; a confidence margin of 0.200; a match ability threshold of 0.60; a filter size of 11; Lagrange tensors; and application of tracking points and virtual extensometer modeling (see below).

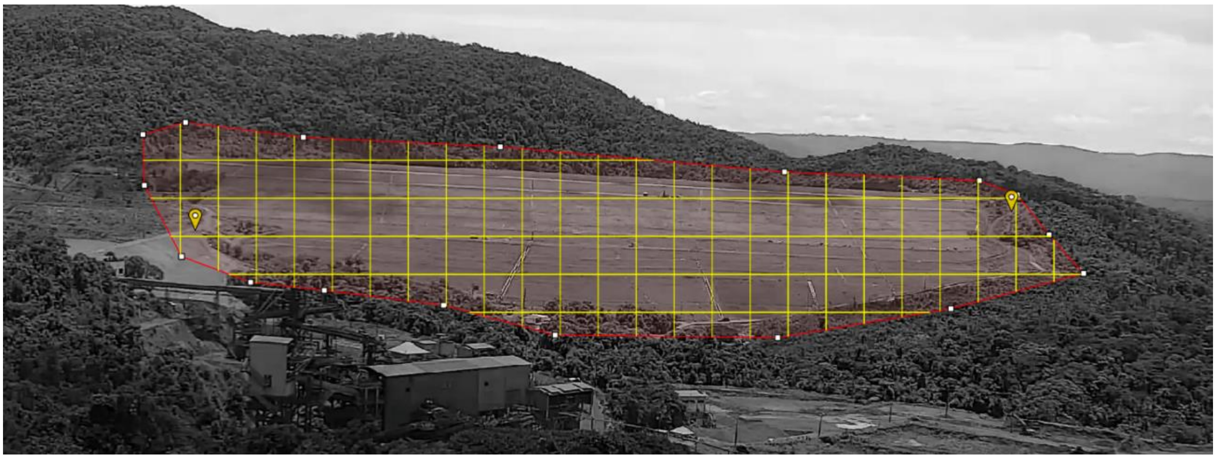

Figure 70: Modeling Environment with a FEM Grid, Reference Points, and Model Boundaries

A second approach also was utilized involving progressive-difference analysis, which is based on a simple but powerful implementation of image differencing within the Matlab computing environment. Difference analysis has the advantage of revealing visible changes of image reflectance patterns, highlighting differences that would otherwise be difficult to see.

The procedure applied for the progressive-difference analysis was:

- after preliminary video footage review, single frames were extracted and saved as single RGB images for the analysis;
- a reference image was defined as the first image with reference reflectance;
- each image was compared to the reference image in a Matlab image analysis environment by applying "imshowpair" image differencing with noise filtering; and
- a matrix of change from blue (no difference) to white (maximum difference) was created for each frame pair.

9.2 <u>Video analysis results</u>

The main results of the two different surface 2D video analysis methods are presented in parallel, to better highlight their differences. The presentation scheme follows the logic depicted in Figure 71. The times discussed below correlate to the video camera time (i.e., they are not adjusted to UTC time or to reflect the 1 s difference with UTC time). The top image of Figure 71 represents a simple RGB high-resolution frame, as extracted from the video footage at the given time, to be used as a visual reference. The central image presents the modeling results in terms of vertical strain deformation *V* (expressed as *m*) overlapped to a greyscale frame. The bottom image of Figure 71 represents the results of image differencing with reference to the initial analysis time (time zero is set at January 25, 2019, at 12:28:23.83). The modeling is based on 120 frames acquired between 12:28:23.83 and 12:28:26.70 from the 30-fps front camera video footage.

The first indication of deformation was at frame 003 (Figure 72). At this stage, the *V* component of the strain is negative, denoting a lowering of this portion of the dam crest by about 0.1 m in the vertical direction. No other deformation is measurable on the remaining dam front.

After 0.2 s, in frame 009, bulging seems to initiate in the central-right portion of the front of the dam (with reference to the observation point of view). As visible in Figure 73, in this case the *V* component of the strain deformation is positive, with a value of ~0.15 m. This indicates a vertical uplift, possibly due to the effect of line-of-sight geometry on the actual deformation vector.

The difference image in a blue to white colour scale at the bottom of Figure 73 does not show clearly the shape of the bulging. It highlights deformations in the same area that are mostly related to the change in reflectivity of the drainage channels and other along-slope linear features.

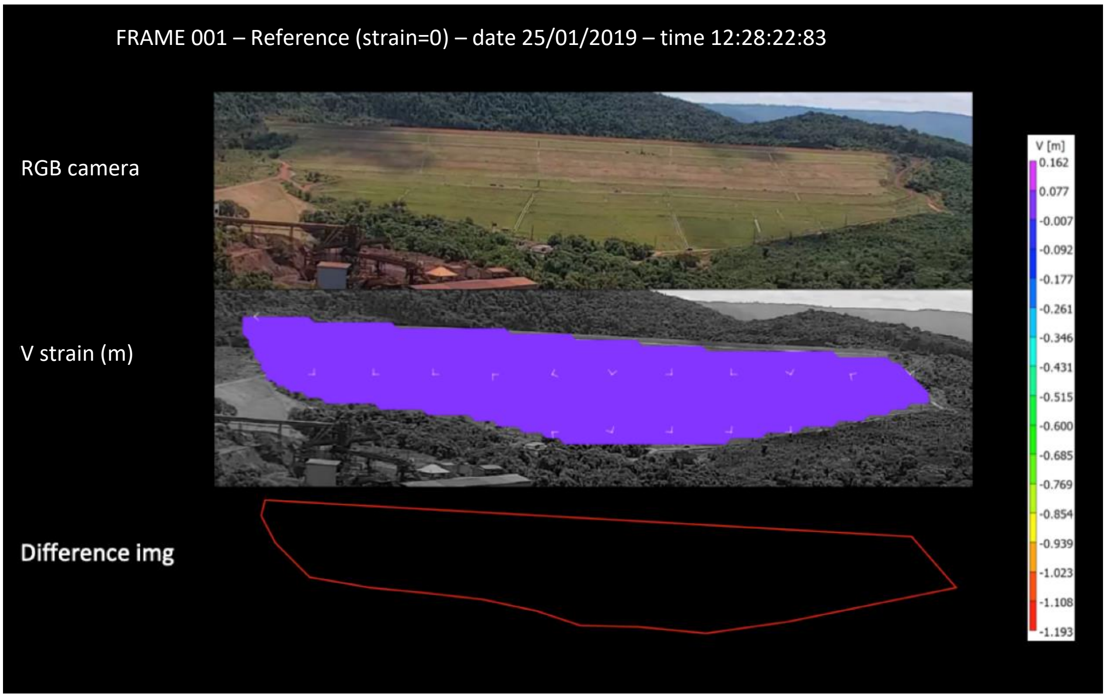

Figure 71: Frame-based Deformation and Change Detection Analysis of Dam I

Figure 72: Frame 003. Initial Strain Develops at Top-center of Dam I

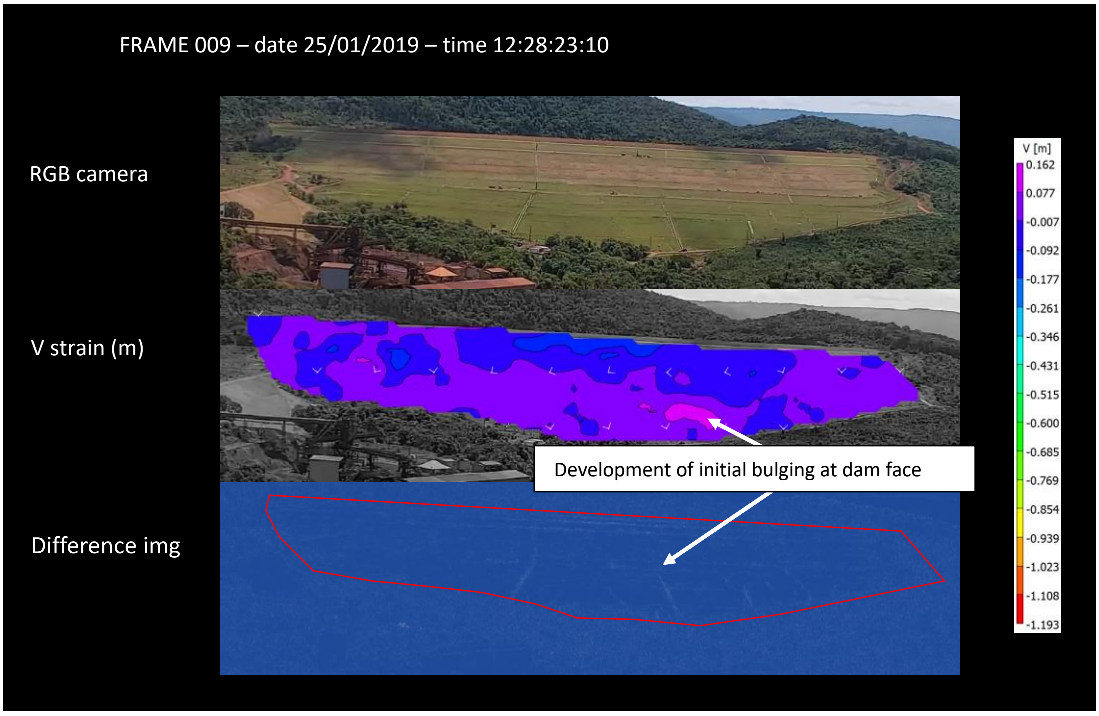

Figure 73: After 0.2 s From Beginning of Deformation at Dam Crest, a Bulging Starts Developing on Central-right Portion of the Dam Face

After 1 full second, at frame 045, Figure 74 shows the deformation at the dam crest accelerating rapidly away from a limited highly deformed area in the center. The deformation pattern is mainly developing horizontally, progressively involving more of the dam crest. The *V* component of the strain deformation is from about -1 m at the center down to zero at a distance of ~120 m on both sides of Dam I. The width of the deformed area is ~30 m.

At the same time, the bulging in the right-central part of the dam face also is developing and expanding, mostly horizontally. The *V* component of the strain deformation is still positive, and the deformation seems to be limited to 0.15 m. However, as already noted, the *V* component is the vector sum of three components along the line-of-sight of the camera. Therefore, the depicted color/value is only the combination of different effects developing on the dam face. Possibly, the vertical positive component is still dominating, but it is compensated, in this phase, by the initial development of a vertical failure component which is still not predominant.

The final stage of this phase of deformation is visible in Figure 75, in which the crest deformation has developed to involve almost 80% of the dam crest width, with a maximum deformation of meters, and the bulging which now occupies most of the lower portion of the dam face.

The positive sign of the *V* component at the bulging changes to negative suddenly at frame 081 (12:28:26.40) (Figure 76). This is a clear indication that the resultant *V* component is mainly downward, driven by gravity. The deformation along this direction is larger than 1 m.

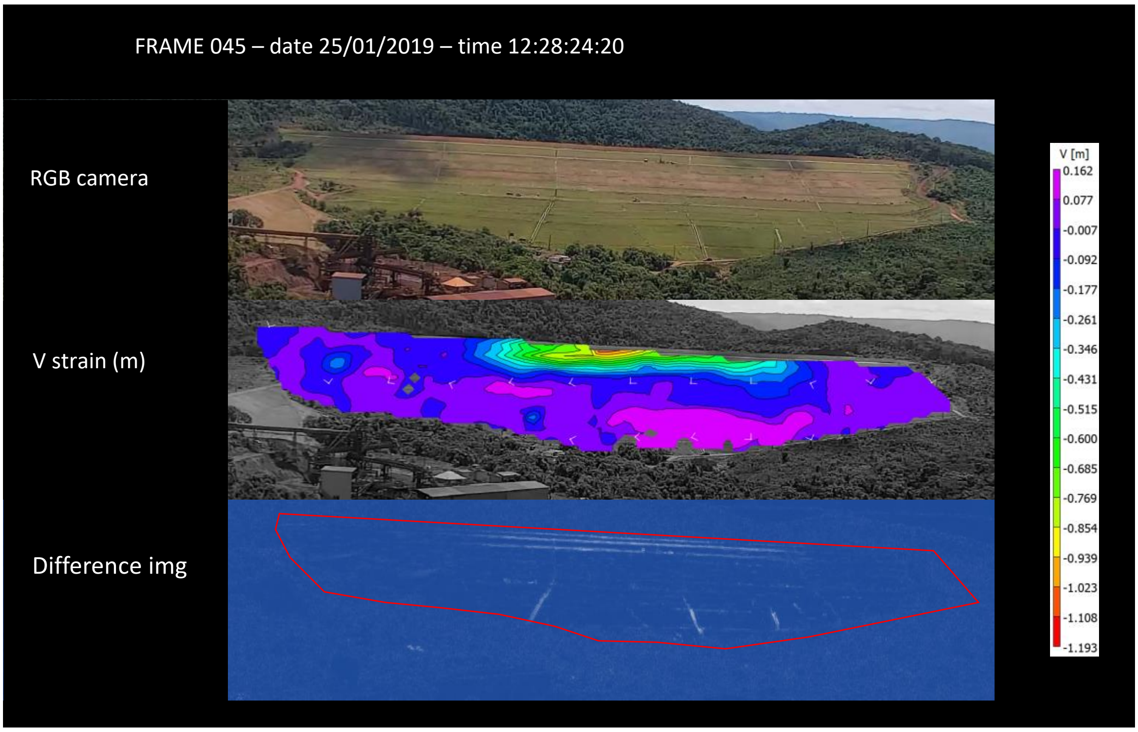

Figure 74: After 45 Frames, Deformation at dam Crest is Accelerating Rapidly, While Bulging of Dam Face is Larger and Still Positive

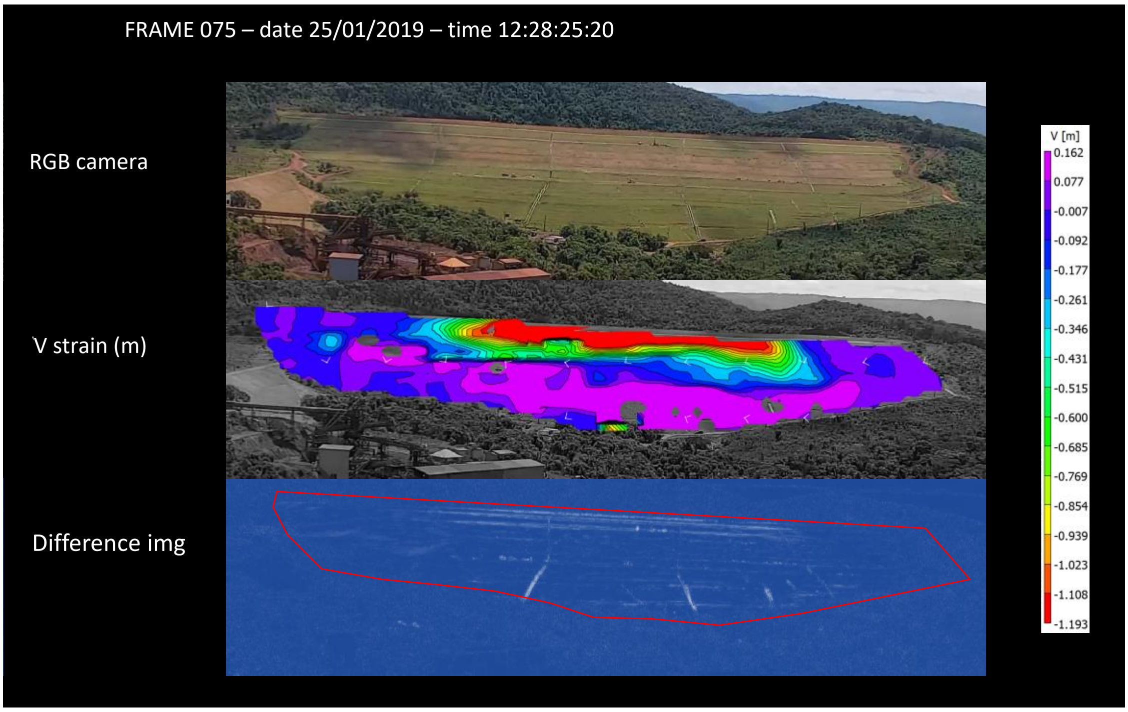

Figure 75: Terminal Stage of Deformation Phase 1, in Which Bulging is Still Positive and Dam Crest is Collapsing Widely

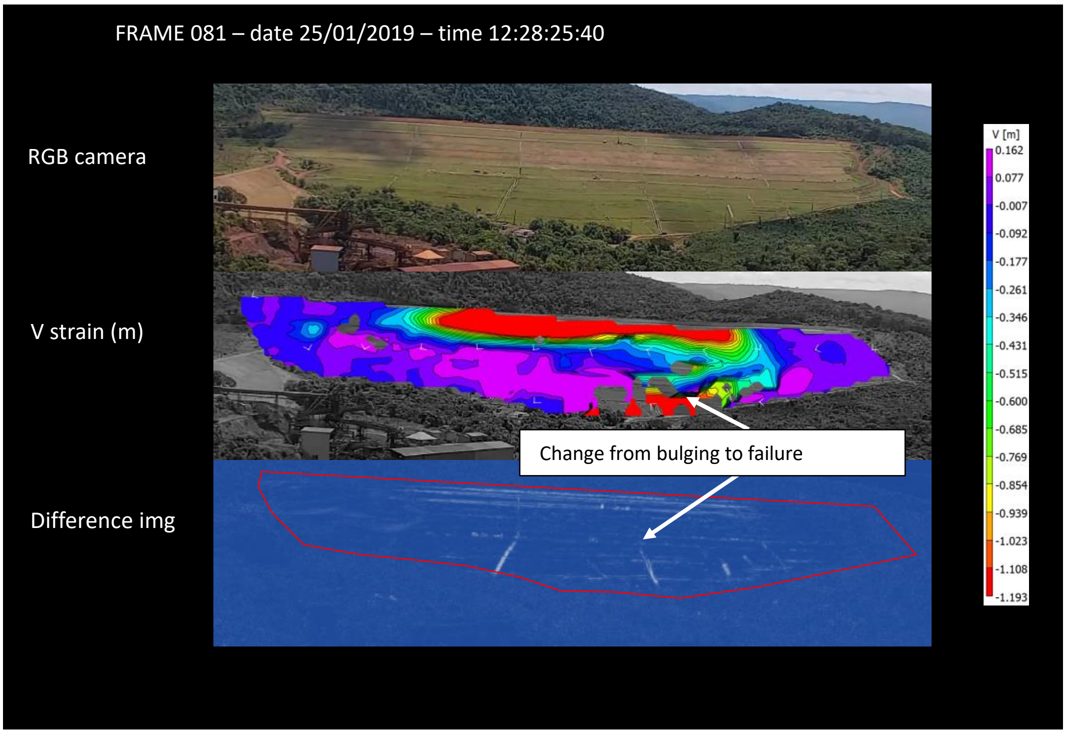

Figure 76: Change from Predominantly Bulging to Predominantly Vertical Collapse of the Central-right Part of the Dam Face

After another 1.30 s, at 12:28:26:70, the failure that initiated at the dam crest joined with the collapse in the central dam face (Figure 77), followed by the general failure, which occurred a few seconds later, at 12:28:30.

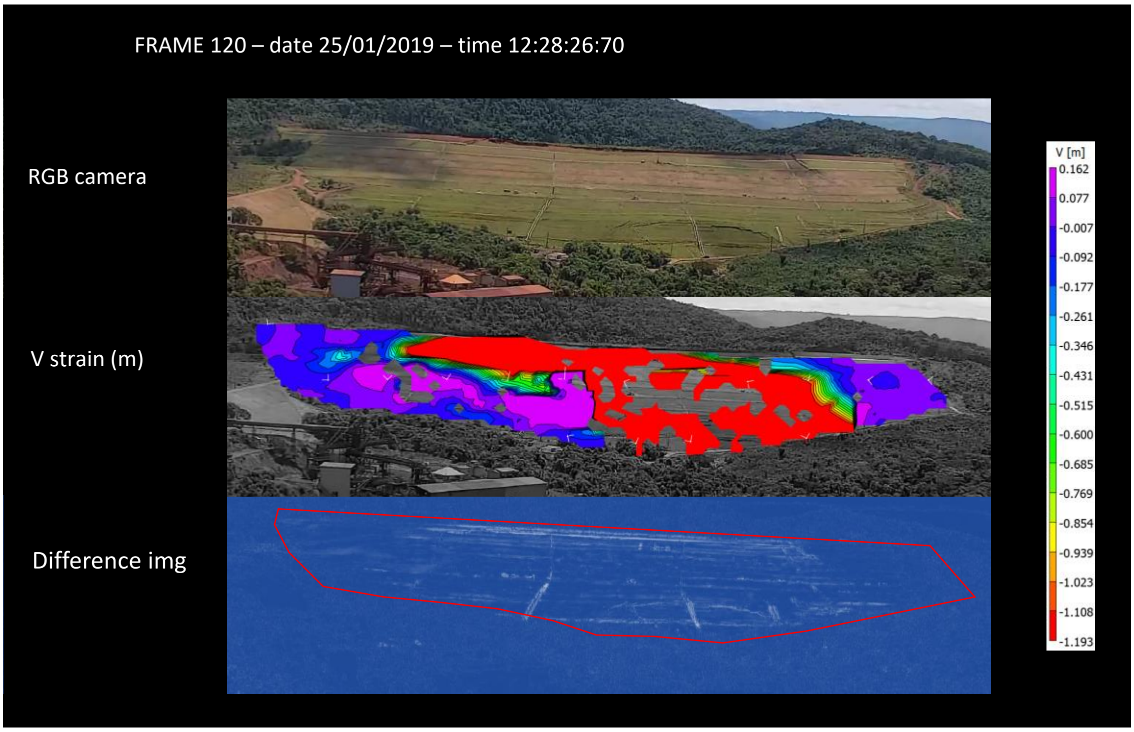

Figure 77: At Frame 120, Two Failure Zones Join and General Dam Failure Starts

According to the results of the DIC and progressive-difference imaging analysis, there are two main failure zones. The first, located at the central part of the dam crest, precedes the second one, at the center-right part of dam face, by a few tenths of a second. The point-tracking tools in the DIC analysis were selected to highlight the deformation vectors in those two areas.

Figure 78 shows the summary of the *V* component deformation time series for those selected points over the 4 s time frame. Tracked points P11, P13 (on the crest) and P17, P8 (on the central dam face) show the highest rates and magnitudes of deformation. Figure 79 suggests that the *V* component of the deformation started at the same time in the two different portions of the dam for the two selected survey points. This is not reflected in the continuous deformation field, however, and may mean that only local deformation was active at that stage on the central dam face.

Figure 80 and Figure 81 show that the *U* component of the deformation of the central-right dam face is not visible, suggesting predominantly upward and outward (towards camera) deformations.

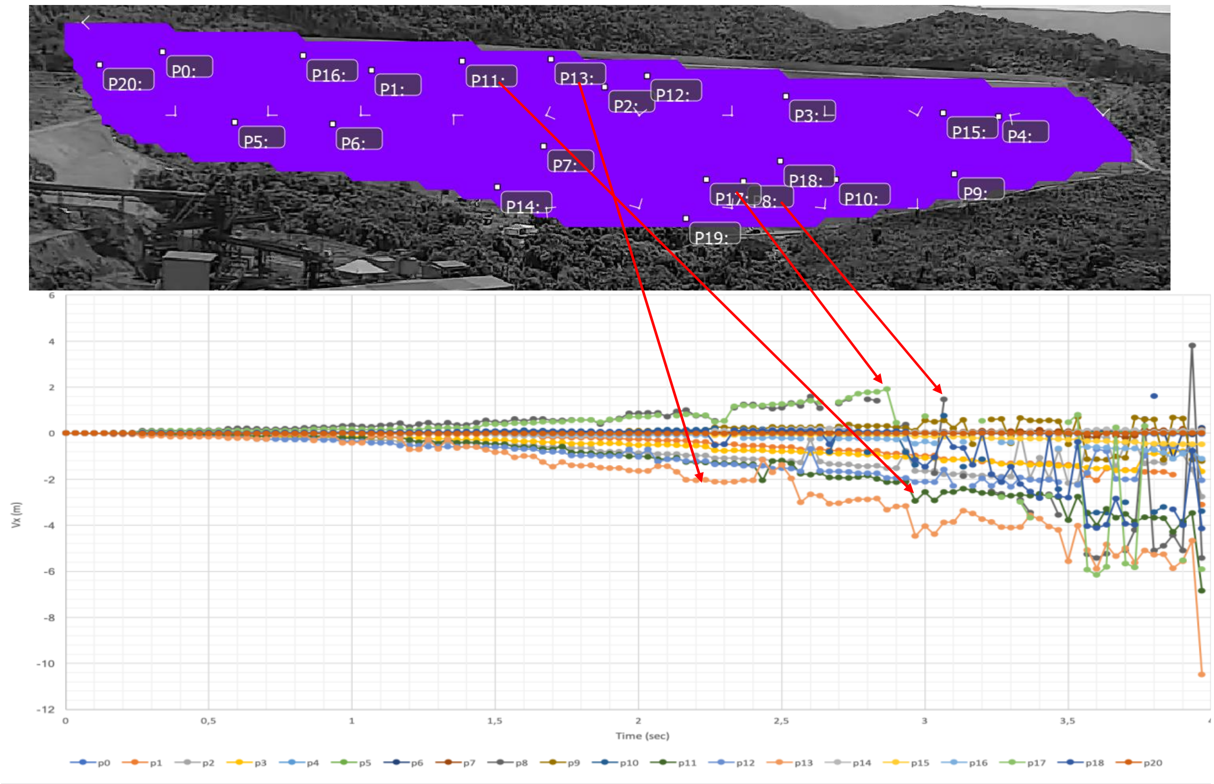

Figure 78: Summary of Point Tracking Analysis From Frame 0 (Time = 0 s) to Frame 120 (Time = 4 s) of Modeled *V* Component

The onset of failure is noted first at the dam crest and then on the lower right side of the dam, with a few tenths of a second between them. After that, deformation also develops on the central part of the dam face.

The deformation at the dam crest shows a steady increase of the negative *V* component of strain (compatible with a gravitational failure; that is, collapse within the body of the dam). The deformation at the central part of the dam face starts with a positive *V* component (probably indicating bulging) followed by inversion to negative values (gravitational failure) about 2 s after the initiation of the failure.

The above considerations may be biased by the sensitivity of the method to the directions perpendicular to the camera line-of-sight. This, however, is not likely to change the general meaning of the conclusions since the line-of-sight bias tends to underestimate measurements such that the actual differential deformations might be even more pronounced than those highlighted in the analysis.

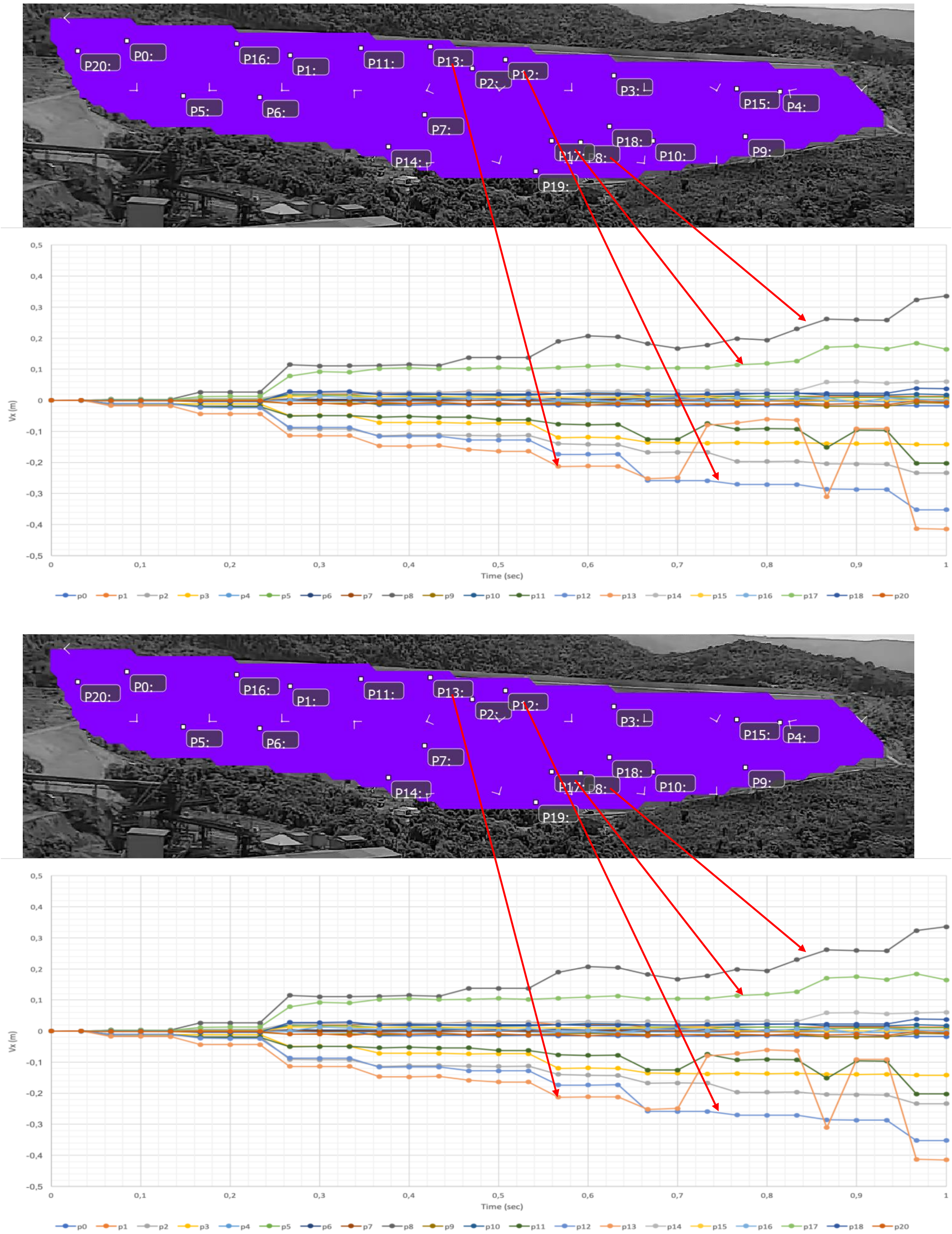

Figure 79: Detailed Point Tracking Analysis From Frame 0 (Time = 0 s) to Frame 30 (Time = 1 s) of Modeled *V* Component

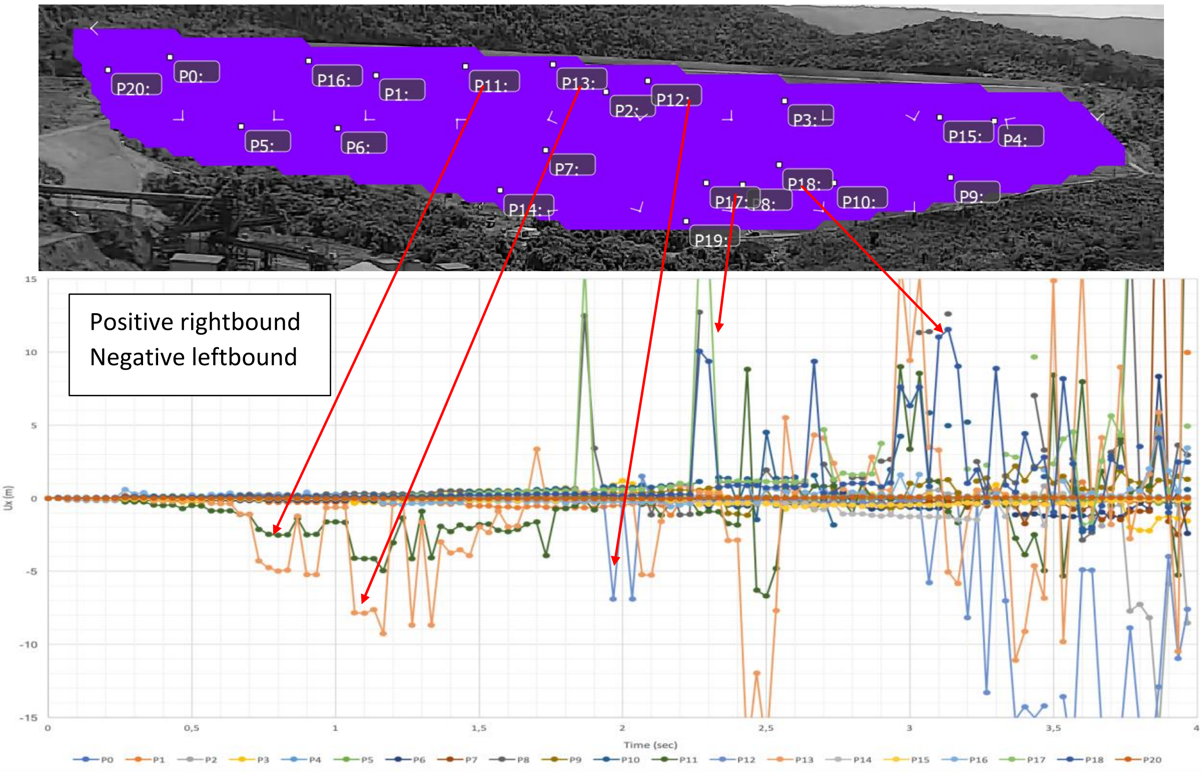

Figure 80: Summary of Point Tracking Analysis From Frame 0 (Time = 0 s) to Frame 120 (Time = 4 s) of Modeled *U* Component

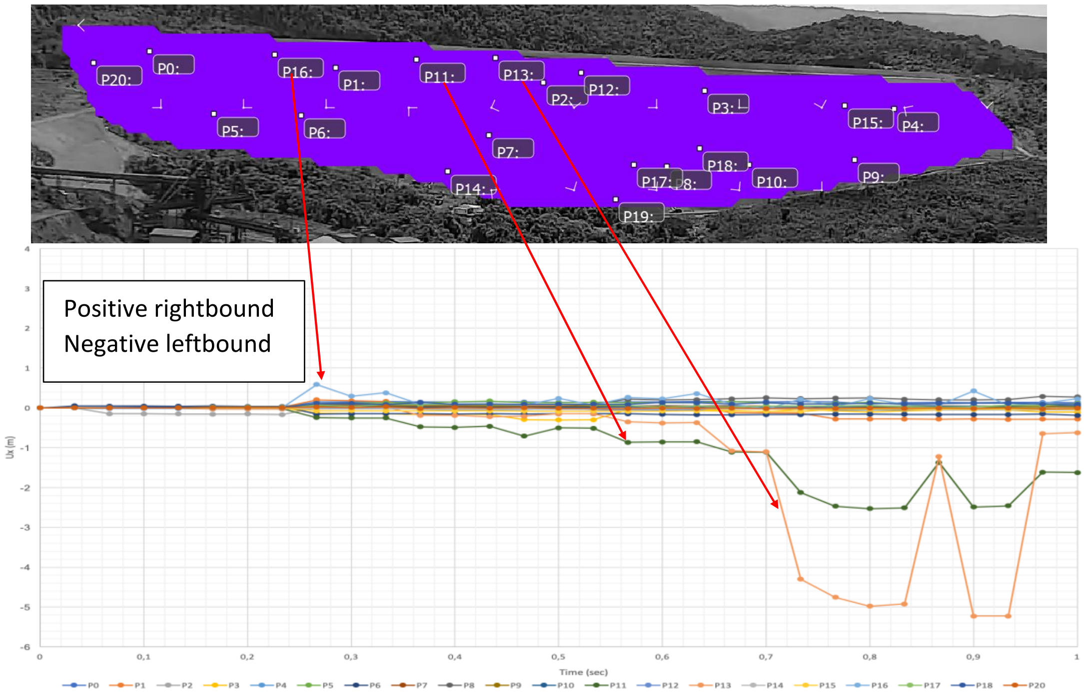

Figure 81: Detailed Point Tracking Analysis From Frame 0 (Time = 0 s) to Frame 30 (Time = 1 s) of Modeled *U* Component

Some methodological considerations should be noted. First, the DIC analysis highlights how the failure developed in the initial stages as visible from the camera geometry. Second, point tracking, despite being cumulative and pointwise, may provide higher accuracy for the initial stages of failure at some specific locations. Difference-imaging may provide an easy-to-read visualization of actual changes in camera footage, but it is probably more accurate on or near specific linear features (such as the dam crest line and water drainage system) due to cross-pixel reflectance changes.

10. DRONE FOOTAGE ANALYSIS

The main objective of the drone footage analysis was the identification of any surface evidence of ongoing or past deformations on the dam surface at the time of the collection of footage (January 2019) visible from the drone. In addition, the analysis was aimed at identifying any superficial sign potentially relevant with respect to the stability of the dam (wet areas, anomalies in the vegetation coverage, presence or absence of water in the drainage channels, etc.).

Two videos were taken on January 18, 2019. During the video acquisition, the drone flew parallel to the dam raisings from the crest to the bottom of the dam. The first video (DJI_0142.mov) covers the upper part of the dam and lasts 15 min, while the second video (DJI_0143.mov) covers the lower part of the dam and lasts 7 min and 35 s. The visibility was very good due to the sunny weather.

Through the visual analysis of the two videos, it was possible to make the following observations:

- Vegetation coverage: The grass was cut recently on the dam with no anomalous vegetated areas. In general, the upper part of the dam had drier conditions than the lower part (i.e., greener grass in the lower part of the dam) (Figure 82). No water was visible in the sector of the tailings visible in the video.
- Wet areas: No wet areas were visible in the drone footage at the time of the flight.
- Drainage channels: Clean and dry drainage channels were present in the upper and central part of the dam (Figure 83), but the channels in the lower part of the dam had flowing water that was brown in color (probably wet mud inside) (Figure 84).
- Morphology: By flying along the crest and the different raisings, neither convex nor concave morphologies potentially associated with past or ongoing deformations were identified (Figure 85). Some localized sectors of the central part of the dam with rough, irregular, and gibbousness morphology may be associated with superficial past deformations or with cows walking on the dam (03:30 of second video) (Figure 86).
- Instability evidences: There were no sign of cracks, trenches, or any clear evidence of ongoing instabilities. On the Seventh Raising, a linear feature, a few meters long, was identified (Figure 87). This feature appears to be local settlement of fill related to the construction of the adjacent concrete drainage channel.

The analysis of the drone footage does not show any recent or active deformations in the dam, including the alleged deformation of January 18, 2019 reported by the ground radar.

Figure 82: Drone Footage at 06:50 of Video DJI_0143.mov Showing Greener Vegetation in Lower Part of Dam Compared to Central and Upper Parts

Figure 83: Drone Footage at 06:20 of Video DJI_0142.mov

Figure 84: Drone Footage at 05:32 of Video DJI_0143.mov Showing Drainage Channel With Brown Mud and Flowing Water

Figure 85: Drone Footage at 02:10 of Video DJI_0142.mov

Figure 86: Drone Footage at 01:48 of Video DJI_0143.mov Showing a Rough Morphology in Central Part of Dam

Figure 87: Drone Footage at 09:30 of Video DJI_0142.mov Showing a Linear Feature Parallel to Bottom of Seventh Raising

11. CONCLUSIONS

The analysis of the LiDAR data facilitated the calculation of the stored tailings volume from the dam crest (8,413,000 m^3), the volume of the material involved in the failure (9,651,000 m^3), and the TWI. The TWI showed that the accumulated flow prior to the construction of Dam I was concentrated at the toe of the dam, in its southern part, where the dam face is exposed to the SW.

The review of the survey data for the prisms installed on the crest of Dam I did not reveal any deformation. This may be attributable to the low precision of the manual measurements (a few centimeters of the error bar) and the low acquisition frequency (monthly).

The radar data did not show any deformation in the last hours or days prior to the failure above the level of the radar noise under the specific set up of the radar (manufacturer quoted minimum detectable velocity of 0.3 mm/h). The signal detected by the radar in the months prior to the failure is interpreted as the accumulation of noise introduced by the presence of vegetation (and stored moisture) on the face of Dam I and by residual atmospheric artefacts, to which the radar wavelength was sensitive.

Small, rapid deformations were recorded by the radar on June 11, 2018 in the central part of Dam I, 35 m and 55 m above DHP 15 following its installation. Closer to DHP 15, initial positive (outward) deformations of up to 6.4 mm were recorded with an average deformation of 2.4 mm, followed by negative (inward) deformations of up to 14.1 mm, with an average of 3.9 mm. Further from DHP 15, only positive deformations were recorded, up to a maximum of 8.3 mm, with an average of 3.6 mm.

The "slow movement" radar data processed after the event to identify the presence of slow deformations in the months before the event also did not identify any deformation above the minimum detectable velocity of the radar with post-processing (3 mm/month). The deformations detected by satellite InSAR at the bottom of Dam I most likely were not detected by the radar because these are slightly below the minimum velocity detectable by the radar.

The analysis of the different satellite InSAR datasets identified deformations in the dam and tailings in the months prior to the failure. In particular, deformations in the range of 16 to 32 mm/y, with a significant E-W component, were detected at the toe of Dam I starting from March/April 2018. A number of phases of accelerations were detected from October to December 2018, with small further accelerations observed from December 2018 to January 2019. Mainly vertical deformations were detected at the crest of Dam I, with a similar temporal evolution as other points on the dam, but with accelerations visible only in late 2018. Vertical deformations were detected in the tailings as well. The detected deformations on Dam I are highly correlated with the rainfall recorded by the F18 rain gauge, and appear to be consistent with settlement.

The analysis of the high resolution (Sentinel-2) and VHR resolution (GeoEye, WorldView3, and Pleiades) multi-spectral images allowed the dynamics of the pond on the tailings to be followed, including its presence and size, and the variation of the vegetation coverage on the dam front. Moreover, an anomalously high value of soil moisture in the setback was detected in the satellite acquisition from December 2018 and early January 2019.

From the analysis of the frontal video frames, the onset of failure was noted first at the dam crest and on the lower left side of the dam, a few tenths of a second before the onset of failure of the main body of the dam. Thereafter, deformation also developed in the central-SE part of the dam face. The deformation at the dam crest showed a steady increase of the negative *V* component of strain (settlement, compatible with a gravitational failure). The deformation at the central-SE dam face starts with a positive *V* component (probably indicating bulging) followed by inversion to negative values (gravitational failure) about 2 s after the initiation of failure. The above considerations may be influenced by the sensitivity of the method to the different components of the deformation vector, considering that the method is more sensitive to deformations in the directions perpendicular to the camera line-of-sight.

The drone footage analysis of the videos acquired in January 2018 did not reveal any particular superficial evidence associable with ongoing or past deformations.